Search for Short Cosmic Gamma-Ray Bursts Using Data from the APEX and LILAS Experiments Onboard the Phobos-2 Interplanetary Spacecraft

A. S. Kozyrev[1*], I. G. Mitrofanov[1], A. B. Sanin[1], and C. Barat[2]

[1]*Space Research Institute, Russian Academy of Sciences, Profsoyuznaya ul. 84/32, Moscow, 117810 Russia*
[2]*Centre d'Etudes Spatiale des Rayonnements, Toulouse, France*

Abstract—A statistical analysis of the spectral and temporal parameters for 546 triggering events on the APEX gamma-ray detector onboard the Phobos-2 spacecraft has revealed a group of 28 events that are probably short cosmic gamma-ray bursts (GRBs). The distribution of the full group of 74 events of the APEX experiment in duration parameter is bimodal in shape, which is in good agreement with the bimodal shape of the BATSE GRB distribution. A search for the detected group of short events using data from the LILAS X-ray and soft gamma-ray detector onboard the same spacecraft has yielded no positive result. A comparison of the APEX and LILAS data has led us to conclude that the short GRBs have a significantly reduced soft gamma-ray flux at energies <100 keV relative to the power law $dN/dE = CE^{-\alpha}$ with the average index $\alpha = 2.62$. © *2004 MAIK "Nauka/Interperiodica"*.

Key words: *gamma-ray astronomy, cosmic gamma-ray busts*.

INTRODUCTION

The Soviet−French APEX (Astrophisico-Plane-tological Experiment) and LILAS experiments of the Phobos-2 mission (Sagdeev and Zakharov 1989) operated for eight months (from July 1988 until March 1989). One of the main scientific objectives of these experiments was to study the emission from cosmic gamma-ray bursts (GRBs) in the energy ranges 50 keV−10 MeV (APEX) and 6−150 keV (LILAS).

The APEX experiment used a large CsI(Tl) scintillation detector with a size of about $10 \times 10 \times 10$ cm and a spectral resolution of $\sim$10% for energies $\sim$1 MeV (Mitrofanov *et al.* 1991). The LILAS experiment used two scintillation detectors made of cleaved NaI(Tl) crystals that recorded X rays and gamma rays with energies above 6 keV (Hurley *et al.* 1994). The sensitivity of the LILAS detectors decreased significantly for photons with energies >100 keV.

Both instruments operated almost continuously in background and burst modes that automatically switched from one to another. The background mode switched to the burst mode during burst triggers before which the current gamma-ray flux was continuously compared with the measured background level in background mode. APEX was triggered when the signal exceeded the background level by more than 7σ at least for one of the three comparison time scales:

0.0625, 0.25, or 1 s. LILAS was triggered in a similar way at a 7σ level on time scales of 0.25 and 1 s.

After a triggering event, APEX switched to burst mode in which the following characteristics of the gamma-ray flux were measured:

(1) *The time profile of the photon flux with 8-ms resolution* during the first 8.6 s and with 0.125-s resolution during the succeeding 55 s. The profile of the photon flux was recorded in the energy range 150 keV to 1.5 MeV.

(2) *The time-to-spill profile of the photon flux* of 24 counts in the energy range 150 keV to 1.5 MeV. The recording mode of the time-to-spill profile allowed a time resolution up to fractions of a millisecond to be achieved.

(3) 116 sequential photon energy spectra recorded in 108 energy channels in the energy range 64−9200 keV.

In burst mode, LILAS produced similar data for each of the two independent detectors.

AN OVERVIEW OF THE DATA ON PREVIOUSLY KNOWN APEX, LILAS, AND BATSE GAMMA-RAY BURSTS

Over the eight months of Phobos-2 operation, the APEX detector recorded 546 triggering events. LILAS triggered 590 times over this period.

Initially, during the period 1988−1992, only 58 APEX triggering events were interpreted as cosmic GRBs
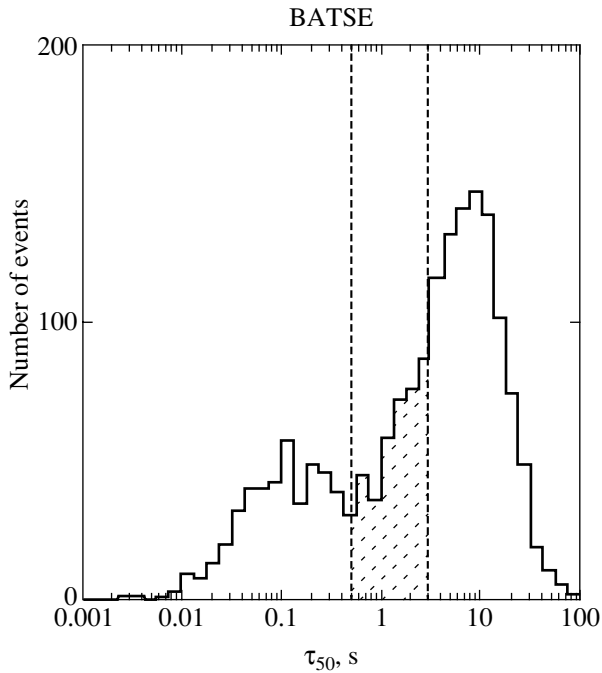
*E-mail: `kozyrev@mx.iki.rssi.ru`

BATSE

Fig. 1. Distribution in duration parameter τ_{50} for 1779 GRBs from the BATSE catalog (Paciesas *et al.* 1999). The hatched region with $0.5 < \tau_{50} < 3$ s was used for a comparison with APEX data.

APEX

Fig. 2. Distribution in duration parameter τ_{50} for the 58 previously known GRBs (*1*) and the combined distribution of the 58 previously known and 16 new short GRB candidates (*2*) constructed from APEX data. The hatched region with $0.5 < \tau_{50} < 3$ s was used for a comparison with BATSE GRBs.

(Mitrofanov *et al.* 1992). It should be noted that 62 events were presented in the above paper. Subsequently, however, four of them were excluded from the APEX GRB list, because these were identified with solar flares or recurrent burst triggers occurred during the same GRB.

At present, BATSE and PHEBUS data have revealed that the GRB distributions in duration parameters T_{50} and T_{90} (Koshut *et al.* 1996) and in emission time τ_{50} (Mitrofanov *et al.* 1999) are bimodal (Dezalay *et al.* 1991; Kouveliotou *et al.* 1993). It has been found that there are two distinct classes of GRBs: long events with characteristic emission times $\tau_{50} > 0.5$ s and short events with $\tau_{50} < 0.5$ s. The emission time was calculated for 1779 GRBs from the fourth BATSE catalog (Paciesas *et al.* 1999). Their distribution clearly shows a bimodal pattern (Fig. 1). The energy spectrum of short GRBs is known to be harder than that of long GRBs (Dezalay *et al.* 1991; Kouveliotou *et al.* 1993).

We constructed the distribution for the 58 previously known APEX GRBs using the emission time τ_{50} (Fig. 2). The left peak that must correspond to short GRBs is virtually absent in this distribution. It follows from the BATSE data that the fraction of short GRBs with $\tau_{50} < 0.5$ s is $\sim$26% of their total number (see Fig. 1). Since the measurement time of the GRB profiles in the APEX experiment was limited by a duration of 63.6 s, the emission
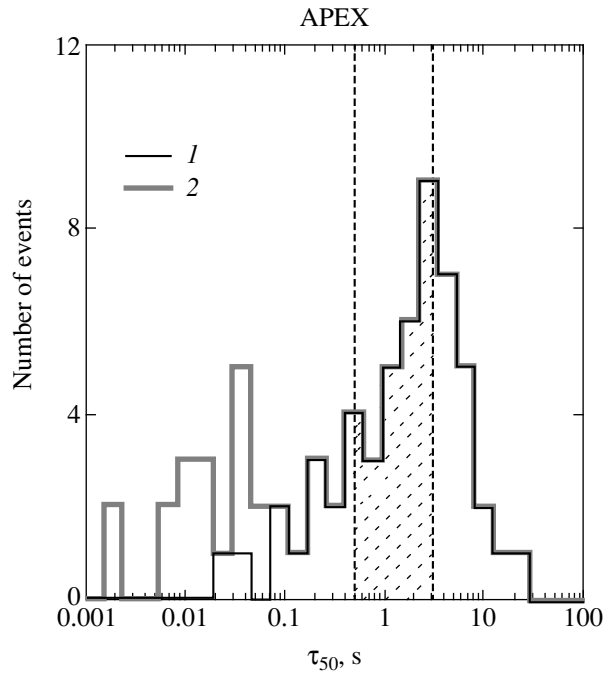
time for long bursts was underestimated, and the right part of the τ_{50} distribution turned out to be displaced leftward, toward the shorter emission times (see Fig. 2). Therefore, for a comparison of the two distributions, we chose the interval $0.5 < \tau_{50} < 3$ s for which the measurements for BATSE and APEX events are comparable. For the BATSE experiment, 460 short GRBs with $\tau_{50} < 0.5$ s correspond to 353 events in the interval $0.5 < \tau_{50} < 3$ s (see Fig. 1). This implies that for the APEX experiment, about 29 short GRBs must correspond to 22 events in the interval $0.5 < \tau_{50} < 3$ s (see Fig. 2). The APEX database (Mitrofanov *et al.* 1999) contains only 12 events with emission times $\tau_{50} < 0.5$ s. This number is a factor of 2.4 smaller than the number of short GRBs that might be expected from the relation derived in the BATSE experiment.

LILAS detected 64 GRBs; all of these events belonged to long bursts with a characteristic variability time of $\sim$30 s. The APEX and LILAS lists of long GRBs were found to match satisfactorily in all of the cases where the two instruments were in background mode and were able to trigger. At the same time, no short events from the APEX database were present in the LILAS list of triggering events. Therefore, they were not identified with GRBs.

To elucidate the causes of the discrepancy between

the APEX and BATSE data on short events, we reanalyzed all of the APEX triggering events in an effort to find the most likely candidates for identification with short GRBs. Subsequently, we compared the list of found candidates with the LILAS list of triggering events to establish the cause of the absence of short GRBs in the LILAS list.

CLASSIFICATION OF THE COMPLETE SET OF APEX TRIGGERING EVENTS

All of the 546 APEX triggering events can be broken down into the following groups:

(1) the well-known group of long GRBs: 60 triggering events of this group correspond to the 58 previously known APEX GRBs (Mitrofanov *et al.* 1992);

(2) the group of 5 events that were reliably identified with solar flares using data from other experiments;

(3) the group of 196 triggering events that occurred because APEX switched to burst mode by an external command or due to internal false triggers of the electronics;

(4) the group of 3 events with telemetry information failures;

(5) the group of 282 hitherto unidentified events that may include short GRBs.

The events of group V account for $\sim 51\%$ of the total number of APEX triggering events, and most of them have one or, more rarely, two or more intervals with a statistically significant excess of the signal above the background level. The overwhelming majority of the triggering events of group V are assumed to have occurred due to the passage of charged particles through the CsI(Tl) crystal. However, it follows from a comparison of the APEX and BATSE data that some of the events of this group are short GRBs.

Thus, the problem of searching for short APEX GRBs consists in separating the events of group V into short GRBs and APEX triggering events from charged particles. This separation will be performed by comparing the statistical distributions in emission time and spectral hardness parameters for the triggering events from charged particles and short GRBs.

STATISTICAL PROPERTIES OF GROUP V OF UNIDENTIFIED APEX EVENTS

To analyze the rapid variability of group V of hitherto unidentified events, it is most convenient to use time-to-spill data. For these data, the time intervals in the profile of an event have different durations that are determined by the time to spill of 24 counts. At a high count rate, the duration of the intervals of this profile can be several fractions of a millisecond. The duration of the intervals increases with decreasing

signal-to-noise ratio; this may lead to an overestimation of the event duration when, after the burst completion, the instrument waits for absent background counts to complete the current interval of the time-to-spill profile. Therefore, to estimate the durations of the events from group V being analyzed, we used not the measured time-to-spill profile, but its analytic fit.

Since all of the time-to-spill profiles for the 282 events of group V are unimodal, these profiles can be described by the analytic function

$$
F(t) = \begin{cases} \dfrac{F_{\max}}{1 + \left(\dfrac{t - t_{\mathrm{o}}}{\tau_{\mathrm{in}}}\right)^2}, & t \leq t_{\mathrm{o}} \\[2em] \dfrac{F_{\max}}{1 + \left(\dfrac{t - t_{\mathrm{o}}}{\tau_{\mathrm{out}}}\right)^2}, & t \geq t_{\mathrm{o}}, \end{cases} \quad (1)
$$

where $F_{\max}$ is the maximum flux reached by the function $F(t)$ at time t_0, which lies within the interval of the peak in the time-to-spill profile; τ_{in} and τ_{out} are the characteristic durations of the rising and falling edges, respectively. We compared the model time-to-spill profile (1) with the measured profiles for the events of group V and estimated its parameters τ_{in}, τ_{out}, t_0, and $F_{\max}$ using Pearson's goodness-of-fit test.

The burst duration parameters T_{50} and T_{90} are known to be affected by systematic effects that depend on the signal-to-noise ratio (Koshut *et al.* 1996). Therefore, to statistically describe the durations of the 282 events of group V, we used the emission time τ_{50} (Mitrofanov *et al.* 1999); the latter is defined as the time in which 50% of the total number of S counts is accumulated at maximum count rate. For the single-pulse events considered in this case, the emission time characterizes the duration of the phase of the most powerful energy release in the detector. Events of a different physical nature (scintillation flashes from the passage of heavy charged particles or flashes from GRBs) are expected to have different distributions in total emission time τ_{50}.

The emission time of the events being analyzed was estimated from their analytic profile (1) as

$$
\tau_{50} = (\tau_{\mathrm{in}} + \tau_{\mathrm{out}})\tan\left(\frac{0.5S}{F_{\max}(\tau_{\mathrm{in}} + \tau_{\mathrm{out}})}\right), \quad (2)
$$

where S is the total number of accumulated counts of the event above the background level.

The distribution of the 282 events of group V in emission time τ_{50} (Fig. 3) exhibits short and long components to the left and to the right of the dashed line, respectively. The long component in the right part of the distribution contains 59 events with emission times $\tau_{50} > 2$ mas. There are probably short
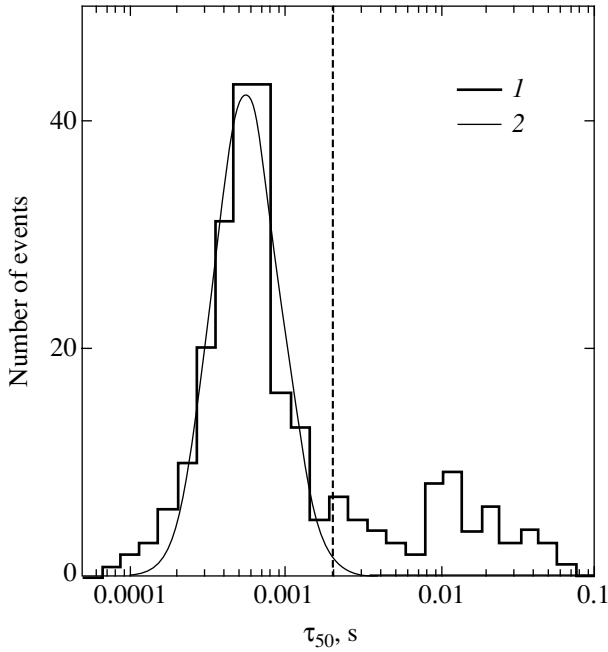
Fig. 3. Distribution in emission time parameter τ_{50} for 282 short events of group V (*1*). We subjected 59 events with $\tau_{50} > 2$ ms (to the left of the dashed line) to Bayesian probabilistic classification. The lognormal fit to the left part of the distribution (*2*) was used as a reference distribution function for the class (B) of charged particles.

Fig. 4. Distributions of the probability density in spectral hardness ratio and their analytical fits used for the probabilistic classification of GRBs (*1*) and charged particles (*2*).

GRBs among the events of this component. The short component in the left part of the distribution contains 223 events and corresponds to a narrow peak on the logarithmic scale. This peak has a mean emission time of about 0.6 ms, and its full width at half maximum corresponds to a spread in values by a factor of about 3 or 4. The short component of the distribution (see Fig. 3) probably corresponds to triggering events from charged particles. However, we do not know whether charged particles contribute appreciably to the long component of the distribution with an emission time of more than 2 ms.

We may assume that triggering events from charged particles dominate among the 110 events of the left slope of the short component with an emission time $\tau_{50} < 0.6$ ms. For these events, we estimated the spectral hardness ratio (HR) from APEX measurements as the ratio of the count rate (with the subtracted background) in the energy range 300–1000 keV to the count rate in the energy range 100–300 keV. The observed spectral HR distribution for these 110 events is represented by the dashed curve in Fig. 4. Its analytical fit is a Gaussian with a nearly zero mean and a variance that corresponds to the statistical fluctuations of the count rate in the spectral channels used. Thus, the events of the left slope of the short component (see Fig. 3) are soft and have no statistically significant signal in
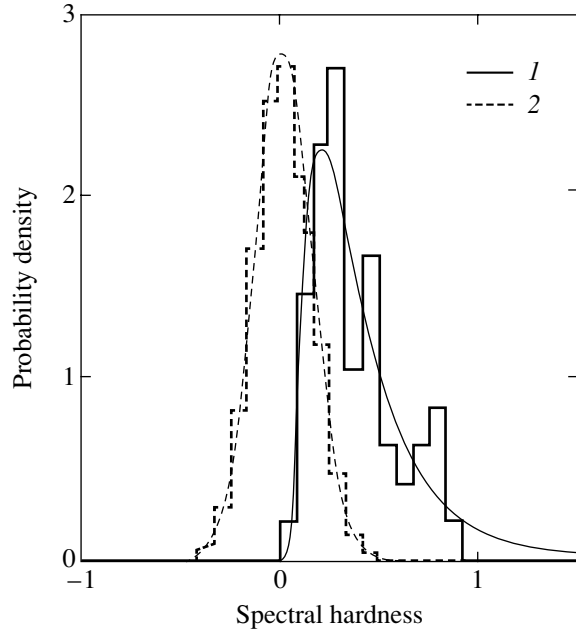
the energy range 300–1000 keV. This conclusion is consistent with the assumption that triggering events from charged particles make an overwhelming contribution to this group, and that short GRBs with their relatively harder emission do not contribute appreciably to this group.

There is a group of 113 events on the right slope of the short component in the distribution of the emission time (see Fig. 3) in the time interval from 0.6 to 2 ms. Undoubtedly, triggering events from charged particles also dominate among them, but short GRB may be present. The only criterion for the identification of bursts in this group can be a relatively large spectral hardness ratio. However, this criterion cannot yield a reliable result for the group of events on the right slope of the short component, because, due to the large number of triggering events from charged particles, their distribution in hardness ratio (see Fig. 4) predicts an appreciable number of events with a large hardness ratio. We cannot reliably identify a small group of GRB-related events against this background. Therefore, it is appropriate to search for and identify short GRBs using APEX data only in an interval with emission times >2 ms, where the contribution from charged particles is probably not dominant (see Fig. 3).

THE METHOD FOR PROBABILISTIC IDENTIFICATION OF SHORT GAMMA-RAY BURSTS IN THE APEX DATABASE

The long component of the distribution of triggering events with emission times >2 ms (see Fig. 3) is a group of 59 events among which short GRBs may be present. The search and identification for them can be performed using Bayesian probabilistic classification. This method is optimal for identifying events of various classes based on a comparison of their statistical properties and distributions (Sivia 1996). We excluded from our analysis two events for which we were unable to estimate the hardness ratio. In searching for short GRBs among the remaining group of 57 APEX triggering events, we calculated the partial probabilities of their belonging to two alternative classes of events: the class of triggering events from charged particles and the class of short GRBs.

We assumed that each analyzed event ξ described by the emission time (τ_{50}) and the hardness ratio (HR) belonged to one of the two alternative classes H_t of events, where t corresponds to the hypothesis of short GRBs (tested class (A)) or the hypothesis of charged particles (tested class (B)). For each event ξ, the partial probability of its belonging to the class H_t was estimated using the Bayes theorem:

$$P(H_t|D_\xi) = P(H_t)\frac{P(D_\xi|H_t)}{P(D_\xi)}, \qquad (3)$$

where $P(H_t)$ is the a priori probability, $P(D_\xi|H_t)$ is the likelihood probability, and $P(D_\xi)$ is the normalization coefficient.

The a priori probability $P(H_t)$ specifies the expected proportion of events in classes (A) and (B) in such a way that $P(H_A) + P(H_B) = 1$. The a priori probability was determined using BATSE data (see Fig. 1). We compared the distributions of the emission time for BATSE and APEX in the τ_{50} interval 0.5 to 3.0 s. The events with $\tau_{50} > 3$ s were excluded from the a priori probability estimate, because the emission time estimates for the longest bursts in the APEX data could be distorted due to a constraint on the maximum length of the measured time profile, 63.6 s.

A comparison of the BATSE and APEX statistics predicts the existence of 29 short GRBs among the APEX triggering events with emission times $\tau_{50} < 0.5$ s. In the previously known APEX GRB database, 12 events satisfy this condition, implying that the deficit of short GRBs is about 17 events (Figs. 1 and 2). Thus, for the 57 classified APEX triggering events, the a priori probabilities for the tested hypotheses (A) and (B) are assumed to be $P(H_A) = 0.3$ and $P(H_B) = 0.7$.

The likelihood probability $P(D_\xi|H_t)$ is the probability that an event ξ with a set of parameters D_ξ

satisfies the hypothesis H_t. This probability is defined as the product of the probabilities of an event belonging to the class H_t for the reference statistical distribution of the emission time and the hardness ratio, $D_\xi = \{d_\xi^{\tau_{50}}$ and $d_\xi^{HR}\}$:

$$P(D_\xi|H_t) = P(d_\xi^{\tau_{50}}|H_t) \times P(d_\xi^{HR}|H_t). \qquad (4)$$

The probabilities $P(d_\xi^{\tau_{50}}|H_t)$ and $P(d_\xi^{HR}|H_t)$ for the class (B) of charged particles were determined from the lognormal fit to the short component of the emission time (Fig. 3) and from the reference HR distribution of the 110 events (Fig. 4) on the left slope of this short component (Fig. 3).

Since the distribution in emission time τ_{50} for the BATSE GRBs on short time scales is limited by 64 ms, there is no point in using it as the reference distribution for the tested class (A) of GRBs. Therefore, to estimate the likelihood probability from the emission time τ_{50} for the events of class (A), we chose a flat, uniform distribution of τ_{50} values from 2 ms to 0.5 s.

We used the statistical HR distribution for all of the previously known APEX GRBs (Mitrofanov et al. 1992) (Fig. 4) as reference HR statistics for the tested class (A) of short GRBs. This choice is fairly conservative, because it is well known that the hardness ratio of short GRBs can be larger than that of long GRBs (Dezalay et al. 1991; Kouveliotou et al. 1993). The reference HR statistics for the tested classes of short GRBs (A) and charged particles (B) are shown in Fig. 4. These distributions significantly overlap each other. However, this overlapping does not rule out the possibility of reliably estimating the Bayesian probability of identification with each of the particle classes, because none of the classes dominates the other in the overlapping region.

The normalization coefficient $P(D_\xi)$ was calculated from the alternativeness condition for the hypotheses being tested: $P(H_A|D_\xi) + P(H_B|D_\xi) = 1$.

THE GROUP OF CANDIDATES FOR SHORT GRBs FROM APEX DATA

The calculated Bayesian probabilities of 57 events belonging to the tested class (A) of GRBs proved to be distributed mainly near unity (a group of 28 events with a high probability of being GRBs) and near zero (a group of 25 events with a high probability of being associated with charged particles). In addition, for four analyzed events, the identification probabilities are distributed over the range 0.1 to 0.9. It follows from this fact that we have managed to reliably separate the group of 57 triggering events into two classes, which confirms the initial assumption that there are two alternative classes of short APEX events.

Table 1. Candidates for short GRBs with an identification probability > 0.5

Triggering number	Probability P_{GRB}	Spectral hardness ratio HR	Emission time τ_{50}, s
73	0.98	0.054	0.008
139	0.92	0.340	0.004
140	1	0.321	0.053
143	1	1.500	0.002
145	1	1.486	0.018
160	1	0.110	0.013
177	0.96	0.048	0.008
181	1	0.042	0.040
212	1	0.051	0.031
217	1	0.111	0.010
231	0.60	0.434	0.002
235	1	0.150	0.011
280	1	0.406	0.031
310	1	0.134	0.059
317	1	0.731	0.002
320	1	0.070	0.019
325	1	0.285	0.039
333	0.63	0.132	0.004
347	1	0.242	0.010
350	1	0.148	0.008
352	1	0.145	0.022
362	1	0.158	0.034
369	1	0.032	0.013
376	1	0.517	0.012
382	1	0.567	0.046
389	1	0.388	0.019
401	1	1.038	0.049
402	1	0.084	0.011
404	1	0.411	0.009
408	1	0.993	0.002

Thirty events with the probabilities of their belonging to GRBs > 0.5 are listed in Table 1. This table also includes the emission times τ_{50} and the hardness ratios (HR). To choose candidates for short GRBs, we set a probability level $P(H_A|D_\xi) > 0.95$. Twenty seven events satisfy this condition.

The complete list of 85 candidates that consists of the 58 previously known GRBs and 27 new candidates for short GRBs is presented in Table 2. Note the group of 11 events that forms a continuous sequence in the complete list from January 18 through February 4, 1989 (see Table 2). It is hard to believe that all these events are associated with short GRBs. There is no information about an enhanced detection rate of solar or Galactic charged particles during this period. However, we should take into account that near-Earth observations cannot always reveal the solar proton events recorded in the vicinity of Mars. It is well known that the Phobos-2 spacecraft reached Mars on January 29, 1989, went into an elliptical orbit around this planet, and some of these events could be associated with particle streams near the planet.

It is appropriate to mark the above group of 11 events by a symbol for the maximum reliability of the results for short GRBs. The remaining 16 events correspond to the most conservative selection of new short APEX GRBs. At the same time, the presence of the events marked by ? in the complete list (Table 2) is appropriate, because it allows us to make a comparison with data from other experiments and, possibly, to elucidate the origin of the events from this group.

Thus, our search has revealed 16 new candidates for short GRBs. Given the 12 previously known short events, the total number of GRBs with short emission times $\tau_{50} < 0.5$ s is now 28 events (Table 2).

This number is in excellent agreement with the estimate obtained by comparing the distributions in emission time for the APEX and BATSE events.

In Fig. 2, the thin line represents the distribution in emission time for the 58 previously known APEX GRBs, and the heavy line indicates the new combined distribution for the 58 previously known and 16 found candidates for APEX cosmic GRBs. The new combined distribution has a bimodal shape that is similar to the shape of the distribution constructed from BATSE data.

Of particular interest is the independent detection of the newly discovered short APEX GRBs by LILAS, which had two independent detectors and, hence, was reliably shielded from charged particles.

Table 2. List of 85 APEX GRBs, including the 58 previously known long (Mitrofanov *et al.* 1992) and 27 found candidates (marked by *)

| Triggering number	Date	GMT	Triggering number	Date	GMT
15	880 801	12:14:30	219	881 203	03:30:03
25	880 806	19:03:30	221	881 203	19:59:19
27	880 810	14:10:29	233	881 210	19:50:08
28	880 810	15:40:39	235*	881 212	09:46:49
39	880 822	10:07:18	254	881 218	07:31:36
40	880 822	22:21:19	272	881 225	09:27:26
42	880 825	00:10:22	280*	881 229	10:51:53
46	880 828	05:01:33	288	881 231	02:17:25
47	880 828	13:33:41	290	890 101	02:06:00
51	880 830	00:20:35	295	890 105	08:54:01
52	880 830	00:36:44	296	890 105	18:58:16
53	880 830	03:03:54	299	890 106	14:53:52
54	880 830	12:47:36	302	890 107	12:27:16
73*	880 906	19:17:00	309	890 108	21:54:13
81	880 911	22:03:49	310*	890 108	22:14:35
101	880 925	06:24:23	317*	890 110	16:09:51
102	880 925	18:13:19	318	890 110	20:01:55
106	880 927	03:36:06	320*	890 111	00:44:04
114	881 002	02:58:01	325*	890 112	04:55:17
117	881 002	22:37:51	346	890 118	05:39:39
128	881 009	02:56:14	347*	890 118	13:21:22
140*	881 011	19:47:44	348	890 118	15:01:59
143*	881 012	02:46:53	350*(?)	890 118	22:01:12
145*	881 012	21:44:41	352*(?)	890 119	04:47:27
157	881 016	05:26:48	362*(?)	890 124	20:35:35
160*	881 016	12:30:50	369*(?)	890 125	22:29:39
162	881 017	09:52:53	376*(?)	890 127	08:47:52
165	881 018	02:37:15	382*(?)	890 131	13:36:40
168	881 020	09:18:04	389*(?)	890 201	11:58:30
170	881 021	01:39:01	401*(?)	890 202	16:40:26
175	881 023	02:41:17	402*(?)	890 202	23:37:59
176	881 023	11:18:51	404*(?)	890 203	15:19:46
177*	881 024	02:35:43	408*(?)	890 204	05:15:59
178	881 024	22:06:55	440	890 209	02:56:00
181*	881 025	19:13:41	476	890 222	12:56:56
189	881 102	07:57:40	479	890 223	08:37:16
193	881 103	12:19:10	481	890 224	15:12:35
194	881 104	10:42:21	483	890 224	19:44:39
202	881 121	18:59:54	486	890 228	02:05:22
212*	881 126	05:14:37	487	890 228	21:32:16
214	881 126	09:39:02	488	890 301	00:37:53
216	881 128	03:33:51	492	890 306	16:45:53
217*	881 203	00:08:14			
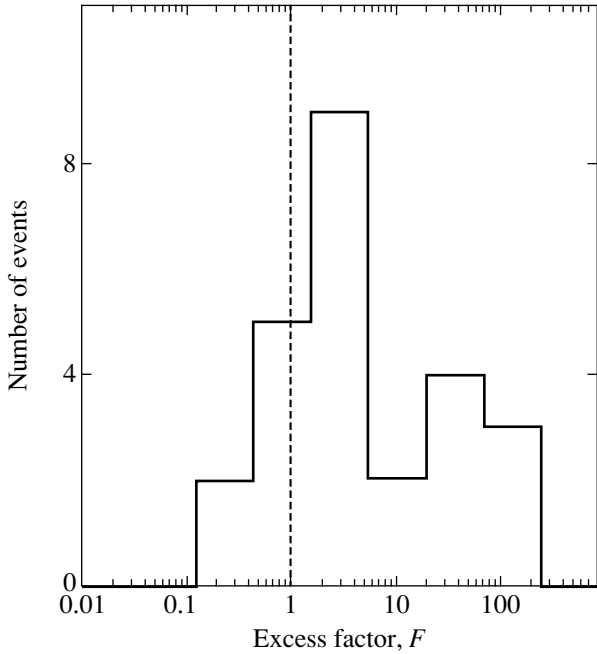
Fig. 5. Distribution of the excess factor F for the emission at low energies <100 keV for 25 of the 28 short GRBs that occurred when LILAS triggered (for this reason, three events were excluded). The dashed straight line indicates the LILAS detection threshold below which there are five events.

COMPARISON OF THE APEX CANDIDATES FOR SHORT GRBs WITH THE LILAS DATABASE

Each of the 28 short APEX GRBs (including the 16 new ones) was tested for its detection by LILAS. For this purpose, we used the excess factor F calculated as the ratio of the expected number of counts in LILAS to the triggering threshold level required for the instrument to switch to burst mode on a time scale of 0.25 s. For short events, this time scale must ensure the most efficient LILAS triggering. Since the background conditions during the Phobos-2 mission were essentially constant, the count threshold level for LILAS triggering was virtually unchanged; it was ~ 63 counts for the 0.25-s time scale.

We estimated the expected signal from a candidate for short APEX GRBs for the LILAS spectral range by using APEX measurements and the hypothesis about a power-law count spectrum of short GRBs:

$$\frac{dN}{dE} = CE^{-\alpha}. \tag{5}$$

The power-law spectral slope α for each event was calculated from the known spectral hardness ratios of the APEX events. The factor C was determined from the condition that the integral of law (5) in the energy range $100-1500$ keV is equal to the measured number of counts from APEX

and by taking into account the reduction in the LILAS detection efficiency of events by the factor $k = 2$. The factor k was determined from the ratio of the detector count rates for three long GRBs (GRB 880 925, GRB 890 224, GRB 890 306) and three short GRBs (GRB 880 830a, GRB 881 104, GRB 890 222) recorded by the two instruments.

A comparison of the 28 short APEX GRBs with the complete list of all LILAS triggering events shows that LILAS has a burst triggering inhibition only in three cases. For the remaining 25 events, the LILAS logic permitted a triggering, but it occurred only for three short events: GRB 880 830a, GRB 881 104, and GRB 890 222. The distribution of the excess factor F for 25 short GRBs is shown in Fig. 5. For five events, our estimates indicate that the LILAS triggering threshold for these events was not exceeded ($F < 1$), and their absence in the LILAS list of events may be considered natural (see Fig. 5). In 17 cases, the LILAS logic allowed a triggering signal to be generated, and the expected number of counts exceeded the threshold required for a triggering ($F > 1$). The absence of triggering events for 17 short APEX GRBs in the complete list of LILAS triggering events can be explained by a cutoff at low energies < 100 keV relative to the power-law energy spectrum (5).

Thus, about 60% of the short APEX GRBs with emission times $\tau_{50} < 0.5$ s (17 of the 28 events) could be recorded by LILAS if the count spectrum of these events obeyed the power law (5). The absence of these events in the complete list of LILAS triggering events may imply that their energy spectra have a cutoff at energies ~ 100 keV, which significantly reduces the count rate in the LILAS spectral range.

As regards the three bursts simultaneously recorded by the two instruments, these events turned out to have a relatively large hardness ratio (~ 0.3) and to be the longest in emission time. Therefore, their properties are most favorable for them to be recorded by LILAS.

CONCLUSIONS

Our reanalysis of the complete list of 546 APEX triggering events has revealed a group of 28 events that are short GRBs with $\tau_{50} < 0.5$ s with a high probability. Twelve of these events have been known previously. The Bayesian probability was estimated for the 16 new candidates for short GRBs to be >0.95.

The new complete group of 74 APEX events presented in Table 2 includes 58 previously known and 16 new short GRBs. The distribution in emission time for the complete group of 74 events is bimodal in shape (Fig. 2), in good agreement with the bimodal shape of the BATSE GRB distribution.

APEX data have revealed that the emission time τ_{50} of the shortest GRBs may be ~2 ms. Given the possible additional cosmological time dilation when passing from the comoving frame of reference to the observer's frame of reference (if the short GRBs are cosmological in nature), such a short emission time imposes significant constraints on the GRB generation mechanism and the sizes of the radiation region of the variable flux.

The detection of only 3 of the 28 APEX candidates for short GRBs by LILAS implies that the LILAS sensitivity was too low for them to be detected. A simple power-law extrapolation of the count rate of short APEX bursts to the range of maximum LILAS sensitivity shows that, for the absence of LILAS triggering events to be explained, we must assume that the short GRBs have a spectral cutoff in the X-ray range.

Many long GRBs are known to have an X-ray emission component. X-ray rich GRBs and bursts whose X-ray emission is accounted for by the bulk of the energy flux (X-ray flares) (Kippen 2002) are currently considered. Our analysis of the APEX and LILAS data has shown that, in contrast to long events, short GRBs probably have no detectable X-ray component. The spectral energy flux density of these events peaks at >100 keV.

Whether long and short GRBs are of different natures is still an open question. However, the results obtained above additionally strengthen the assumption that these classes of GRBs can have different emission sources.

ACKNOWLEDGMENTS

REFERENCES

1. J.-P. Dezalay, C. Barat, R. Talon, *et al.*, *Gamma-Ray Burst Huntsville,* Ed. by W. S. Paciesas and G. J. Fishman (AIP, New York, 1991); AIP Conf. Proc. **265**, 304 (1991).

2. K. Hurley, J.-L. Atteia, E. Jourdain, *et al.*, Astrophys. J. **423**, 709 (1994).

3. R. M. Kippen, *Gamma-Ray Burst and Afterglow Astronomy* (AIP, New York, 2002); AIP Conf. Proc. **662**, 244 (2003).

4. T. M. Koshut, W. S. Pasiesas, C. Kouveliotou, *et al.*, Astrophys. J. **463**, 570 (1996).

5. C. Kouveliotou, C. A. Megan, G. J. Fishman, *et al.*, Astrophys. J. Lett. **413**, L101 (1993).

6. I. G. Mitrofanov, J.-L. Atteia, C. Barat, *et al.*, Planetary Space Sci. **30**, 23 (1991).

7. I. G. Mitrofanov, A. S. Pozanenko, J.-L. Atteia, *et al.*, in *Proceedings of the Los Alamos Workshop on Gamma-Ray Burst*, Ed. by C. Ho, R. Epstein, and E. Fenimore (Taos, New Mexico, 1992), p. 203.

8. I. G. Mitrofanov, D. S. Anfimov, M. L. Litvak, *et al.*, Astrophys. J. **522**, 1096 (1999).

9. W. S. Paciesas, C. A. Meegan, G. N. Pendleton, *et al.*, Astrophys. J., Suppl. Ser. **122**, 465 (1999).

10. R. Z. Sagdeev and A. V. Zakharov, Nature **341**, 581 (1989).

11. D. Sivia, *Data Analysis. A Bayesian Tutorial* (Clarendon, Oxford, 1996).

Translated by V. Astakhov

The Method of a Two-Point Conditional Column Density for Estimating the Fractal Dimension of the Distribution of Galaxies

Yu. V. Baryshev and Yu. L. Bukhmastova*

Astronomical Institute, St. Petersburg State University, Universitetskiĭ pr. 28, Petrodvorets, 198504 Russia
Received April 21, 2003; in final form, December 15, 2003

Abstract—We suggest a new method for estimating the fractal dimension of the spatial distribution of galaxies: the method of selected cylinders. We show the capabilities of this method by constructing a two-point conditional column density for galaxies with known redshifts from the LEDA database. The fractal dimension of a sample of LEDA and EDR SDSS galaxies has been estimated to be 2.1 ± 0.1 for cylinder lengths of 200 Mpc. A major advantage of the suggested method is that it allows scales comparable to the catalog depth to be analyzed for galaxy surveys in the form of conical sectors and small fields in the sky. © 2004 MAIK "Nauka/Interperiodica".

Key words: *galaxies, groups and clusters of galaxies, intergalactic gas, spatial galaxy distribution, fractal dimension.*

INTRODUCTION

Various methods are used to statistically analyze the spatial distribution of galaxies. An overview of these methods is given in the monographs by Martinez and Saar (2002) and Gabrielli *et al.* (2004), who, in particular, considered stochastic point fractal processes.

The method of a conditional number density suggested by Pietronero (1987) and applied to available galaxy redshift surveys by Sylos-Labini *et al.* (1998) is a standard method for analyzing the fractal structures of galaxies. When applied to various samples, this method yields fractal dimensions D of the spatial galaxy distribution ranging from 1.6 to 2.2. To implement this method requires sequentially selecting the spherical volumes in the initial sample of galaxies and counting the objects in these spherical volumes. Since actual galaxy surveys often have the form of narrow conical sectors, the method of a conditional number density is limited by the radius of the largest sphere that completely fits into the volume of a given survey.

In this paper, we suggest a new method for estimating the fractal dimension—the method of selected cylinders. Its advantage over the method of a conditional number density is that it does not require invoking the spherical volume of a sample, but can be applied to narrow spatial layers, because it uses information about the distribution of objects along the segments connecting the pairs of points in the structure.

*E-mail: `bukh@astro.spbu.ru`

STOCHASTIC FRACTAL STRUCTURES

The Density of Stochastic Fractal Structures

The concept of fluid (gas) density, which is commonly used in hydrodynamics, contains the assumption that there is a density that does not depend on the volume element dV. We can then determine the density $\varrho(\mathbf{x})$ at point $\mathbf{x}$ and treat it as an ordinary continuous function of the position in space. In the problem of analyzing the fluctuations, $\varrho(\mathbf{x})$ can be a realization of a stochastic process for which the ordinary moments are specified: the mean, the variance, etc. In particular, this can be a discrete process containing a finite number of points, for example, a Poisson process with a particle number density $n(\mathbf{x})$.

For fractal structures, the concept of particle number density at a point does not exist, because each volume element of the structure contains a hierarchy of clusters and the number density depends significantly on the volume element dV (Mandelbrot 1982). To describe the continuous hierarchy of clustering, which is a new characteristic of the process, we must introduce a new independent variable—the radius r of the region in which the particles are counted. In this case, the number of particles in a self-similar structure increases as a power law

$$N(r) = Br^D. \tag{1}$$

Here, D is the fractal dimension, and $B = N_0/r_0^D$ is determined by the number N_0 of objects within the zero-level scale r_0. Two functions are used to characterize the density of fractal structures,

$n_V(r) = N(r)/V(r)$ and $n_S(r) = (dN/dr)/S(r)$, where $V(r) = (4\pi/3)r^3$, $S(r) = 4\pi r^2$.

Let us consider a discrete stochastic process whose realizations represent sets of points at random positions $\{\mathbf{x}_i\}$, $i = 1,\ldots,N$, so the realized particle number density $n(\mathbf{x})$ is given by

$$n(\mathbf{x}) = \sum_{i=1}^{N} \delta(\mathbf{x} - \mathbf{x}_i). \tag{2}$$

If the stochastic process is fractal, then an additional fractal variable r that characterizes the degree of singularity of the fractal structure must be considered to describe it. Let $N_V(\mathbf{x}_a, r)$ denote the number of particles in the sphere of radius r centered at point $\mathbf{x}_a$ in the structure:

$$N_V(\mathbf{x}_a, r) = \int_0^r n(\mathbf{x}) d^3x, \tag{3}$$

and $N_S(\mathbf{x}_i, r)$ is the number of particles in the shell $(r, r + \triangle r)$ centered at point $\mathbf{x}_a$ in the structure:

$$N_S(\mathbf{x}_a, r) = \int_r^{r+\triangle r} n(\mathbf{x}) d^3x. \tag{4}$$

When we go from one realization to another, these quantities undergo fluctuations; a dependence on the scale r remains after averaging over the set of realizations. For ergodic processes, the averaging over realizations may be replaced with the averaging over the points of one realization. According to Pietronero (1987), the conditional number density of a stochastic fractal process can be defined as

$$\eta(r) = \left\langle \frac{N_S(\mathbf{x}_a, r)}{4\pi r^2 \triangle r} \right\rangle_{\mathbf{x}_a} = \frac{1}{N} \sum_{i=1}^{N} \frac{1}{4\pi r^2 \triangle r} \tag{5}$$

$$\times \int_r^{r+\triangle r} n(\mathbf{x}) d^3x = \frac{DB}{4\pi} r^{-(3-D)},$$

while the volume conditional number density is

$$\eta_V(r) = \left\langle \frac{N_V(\mathbf{x}_a, r)}{(4\pi/3)r^3} \right\rangle_{\mathbf{x}_a} \tag{6}$$

$$= \frac{1}{N} \sum_{i=1}^{N} \frac{3}{4\pi r^3} \int_0^r n(\mathbf{x}) d^3x = \frac{3B}{4\pi} r^{-(3-D)}.$$

Here, $\langle\cdot\rangle_{\mathbf{x}_a}$ denotes the averaging performed on the condition that the centers of the spheres are located at the points occupied by the particles of the realization

(hence the name "conditional"), and the last equalities in (5) and (6) apply to the ideal fractal structures (1) for which $\eta_V(r) = (3/D)\eta(r)$. The exponent in the conditional number density

$$\gamma = 3 - D \tag{7}$$

is called the fractal codimension of the structure.

A fundamentally important property of the conditional number density is that for processes with finite fractal scales beyond which the particle distribution becomes uniform, statistics (5) and (6) reach constant values, which corresponds to the equality $D = 3$ for homogeneous structures. Thus, the method of a conditional number density is a powerful tool in searching for the boundary of the transition from fractal clustering to homogeneity.

The Two-Point Conditional Column Density

The conditional number densities of the stochastic fractal processes considered above are one-point densities, because the center of the sphere in which the particles are counted is placed at one point $\{a\}$ with coordinates $\{\mathbf{x}_a\}$. In some cosmological problems, for example, those related to gravitational lensing (see, e.g., Baryshev and Ezova 1997), it is necessary to use two-point conditional number densities where the two particles $\{a, b\}$ with coordinates $\{\mathbf{x}_a, \mathbf{x}_b\}$ are fixed. The transition from the one-point to two-point conditional number densities in the analysis of fractal structures is similar to the transition from two-point to three-point correlation functions in the analysis of ordinary stochastic processes.

To characterize the particle distribution along the cylinder whose axis connects two points of the structure $\{a, b\} \subset \{x_i, i = 1,\ldots,N\}$, let us introduce the concept of two-point conditional column density $\eta_{ab}(r)$ of a stochastic fractal process. According to Mandelbrot's cosmological principle, particles a and b are statistically equivalent; therefore, the one-point conditional particle number density for each of the points is given by formula (5), which is proportional to the probability of particle occurrence at distance r from the fixed point of the structure. In the case of two independent fixed points of the structure spaced $r_{ab} = |\mathbf{x}_a - \mathbf{x}_b|$ apart, event C that consists in the occurrence of a particle at distance r_a from point a and the independent occurrence of a particle at distance r_b from point b of the fractal structure is given by the union $C = A \bigcup B$ of the events pertaining to each of the fixed points a and b. The assumption that events A and B are independent is the first simple step and can be generalized to dependent events. However, applications of the cylinder method to actual fractal structures have shown that the assumption of independence is a satisfactory approximation.
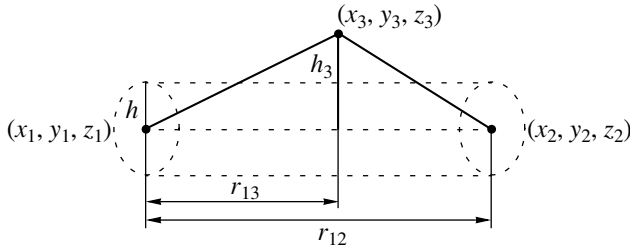
Fig. 1. Method of selected cylinders: the centers of two galaxies are fixed at the points with coordinates (x_1, y_1, z_1) and (x_2, y_2, z_2). All of the remaining galaxies with central coordinates (x_3, y_3, z_3) are checked to determine whether they belong to a given cylinder.

Let us consider the case where a fractal structure is superimposed on the background of an additional homogeneous Poisson process. The two-point conditional column density can then be represented as the sum of the one-point conditional number densities on a Poisson background:

$$\eta_{ab}(r) = \eta_a(r) + \eta_b(r_{ab} - r) + c \qquad (8)$$
$$= \frac{DB'}{4\pi} r_{ab}^{D-3} \left[\left(\frac{r}{r_{ab}} \right)^{D-3} + \left(1 - \frac{r}{r_{ab}} \right)^{D-3} + c_0 \right].$$

Here, the distance r is measured along the rectilinear segment connecting particles a and b and simultaneously determines the radius r of the sphere centered at the first point and the radius $r_{ab} - r$ of the sphere centered at the second point, and the constant B' can be determined from the normalization condition that includes the contribution from the homogeneous background specified by the constants c and c_0. The volume elements in this formula are distributed along the segment ab, and, in this sense, r is a one-dimensional Cartesian coordinate.

The following statistics can be used as an estimate of $\eta_{ab}(r)$:

$$\eta_{ab}(r) = \left\langle \frac{N_c(\mathbf{x}_a, \mathbf{x}_b, r, h, \triangle r)}{\pi h^2 \triangle r} \right\rangle_{\{a,b\}} \qquad (9)$$
$$= \frac{1}{N_{ab}} \sum_{\{a,b\}}^{N_{ab}} \frac{1}{\pi h^2 \triangle r} \int_r^{r+\triangle r} \int_0^h n(\mathbf{x}) 2\pi h \, dh \, dr,$$

where N_c is the number of particles in the volume element of a cylinder with the base radius h and height $\triangle r$ and with the axis connecting particles a and b that belong to the fractal structure at distance r from particle a, which also corresponds to the distance $r_{ab} - r$ from particle b. The averaging is over all pairs of points with the cylinders of length $l = r_{ab} \pm m$, where the distance m is determined by the choice of

discreteness in ray length in the sample of objects under consideration.

An Algorithm for Estimating the Two-Point Conditional Column Density

Let us now consider a practical algorithm of the method of selected cylinders to estimate the column density of objects (galaxies) between specific pairs of points in the structure (fixed galaxies). These points (galactic centers) are placed at the centers of the cylinder bases. The cylinder radii are chosen to be much smaller than the mean separation between the elements of the structure estimated for the sample volume under consideration.

We choose objects with known equatorial coordinates α and δ and redshifts $z_{\rm G}$ from the catalog of galaxies being studied.

Step 1. Since a substantial amount of dust is concentrated in the plane of the Galaxy, the number of galaxies observed through the Galactic equator is significantly reduced. To prevent the distortions introduced by this observational selection, let us divide our sample into two parts. To this end, we calculate the Galactic coordinate b of each galaxy in the sample and attribute the galaxies of the northern ($b > 10°$) and southern ($b < -10°$) Galactic hemispheres to the first and second parts.

Step 2. We transform the equatorial coordinates of the galaxies into their Cartesian coordinates: $\alpha, \delta, z_{\rm G} \rightarrow x, y, z$.

Step 3. We choose any two galaxies and denote the coordinates of their centers by (x_1, y_1, z_1) and (x_2, y_2, z_2), respectively. We place the points with these coordinates at the centers of the cylinder bases. We choose the cylinder radius $h = 1 \times 10^{-4} R_H$, where $R_H = c/H = 5 \times 10^6$ kpc (below, $H = 60$ km s^{-1} Mpc^{-1} is used).

Step 4. We examine all of the remaining galaxies in the sample in turn. Each time, we denote the coordinates of the galactic center as (x_3, y_3, z_3). Following Fig. 1, we determine the distance from the point with coordinates (x_3, y_3, z_3) to the cylinder axis $h_3 = \sin A a_3 R_H$, where $\cos A = \frac{a_3^2 + a_1^2 - a_2^2}{2 a_3 a_1}$,

$$\begin{cases} a_1 = \sqrt{(x_2 - x_1)^2 + (y_2 - y_1)^2 + (z_2 - z_1)^2} \\ a_2 = \sqrt{(x_3 - x_1)^2 + (y_3 - y_1)^2 + (z_3 - z_1)^2} \\ a_3 = \sqrt{(x_3 - x_2)^2 + (y_3 - y_2)^2 + (z_3 - z_2)^2}. \end{cases}$$

The selection criterion: If the galaxy (x_3, y_3, z_3) falls into the cylinder $h_3 < h$, we then calculate the ratio $r_{13}/r_{12} = a$ (since the base of the selected cylinder is much smaller than its height, we assume that r_{13} is the projection onto the axis).

Output data of the method: the total number N of events when galaxies fall into cylinders, the number $N(a)$ of events when galaxies fall into certain parts of the cylinder, and $N(a)/N$ is the column density of the objects between points (x_1, y_1, z_1) and (x_2, y_2, z_2).

Let us now write formula (8) as

$$\frac{N(a)}{N} = 0.5\Big((Ra)^{-\alpha} + (R(1-a))^{-\alpha} + b\Big), \quad (10)$$

where R is the factor defined as the ratio of the maximum length of the segments in the sample to the minimum fractal scale in the sample, b is the constant corresponding to the background Poisson distribution, and α is the exponent that determines the fractal dimension $D = 3 - \alpha$. The sample should be analyzed to determine the parameters R, α, b.

If the real distribution of galaxies is fractal, then galaxies statistically "prefer" to be clustered toward the ends of the cylinders located in any two fixed galaxies. Thus, the principal idea of fractality is demonstrated: all galaxies are equivalent elements of the structure, and the variations in the number density of the objects with distance from the galaxies follows the same pattern.

APPLICATION OF THE METHOD

A Mock Uniform Distribution

According to formula (8), for a uniform distribution of objects in space ($D = 3$), the conditional two-point density is constant. To check whether the algorithm in this simple case is efficient, we simulated a mock catalog of galaxies with a Poisson distribution of 2500 points in space. Figure 2 shows the distribution of galaxies between any two fixed points in this case. It can be immediately seen from this figure that for a uniform distribution of objects in space, there is no clustering toward the ends of the segments.

The LEDA Sample of Galaxies

The LEDA database (Paturel 1997) gives the following astrophysical parameters of galaxies: designations, morphological descriptions, diameters, magnitudes in various color bands, radial velocities, central velocity dispersion, etc. The LEDA sample of galaxies contains observational data from various catalogs. Spatial coordinates are presented for 77 483 galaxies with redshifts z ranging from 10^{-4} to 0.25. According to Silos-Labini *et al.* (1998), the completeness of the LEDA database is 90% for galaxies with $m_B \leq 14.5$ and known redshifts, 50% for galaxies with $m_B \leq 16$ and known redshifts, and 10% for galaxies with $m_B = 17$ and known redshifts.

Let us now apply the method of selected cylinders to the LEDA sample of galaxies. We limit the
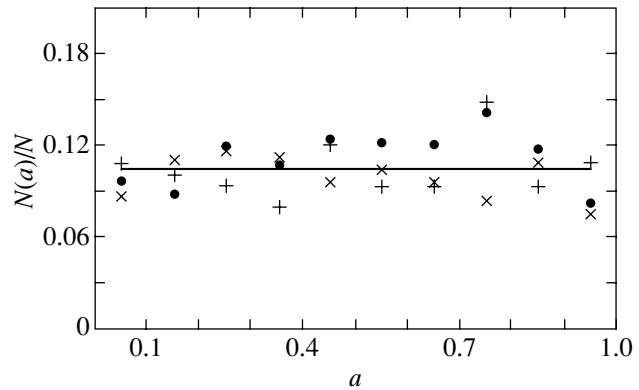

Fig. 2. Distribution of objects in fixed cylinders for a mock uniform distribution of objects in space. The dots, crosses, and pluses indicate the results of our three numerical simulations, and the curve represented the least-squares fit.

sample by redshift and absolute magnitude. Consider the volume-complete samples of galaxies with $M < -17$ separately for the northern and southern Galactic hemispheres. Thus, the number of galaxies with $z < 0.02$ ($\sim$100 Mpc) is 7265 and 6467 in the northern and southern parts of the sky, respectively. The galaxies are fixed in pairs. The points with the coordinates of the centers of these galaxies are located at the cylinder bases. All of the remaining northern and southern sky galaxies are checked to see whether they belong to these cylinders. We sort the cylinders by height (by segment lengths). How are the galaxies distributed in the fixed cylinders between two fixed galaxies?

A distinctive feature of a fractal is its self-similarity on any scale. To make sure that this assumption is valid for the LEDA sample of galaxies, let us single out several subsamples from the total sample containing the set of segments of various lengths. The first subsample contains all of the segments with lengths up to 50 Mpc, the second subsample contains the segments with lengths from 50 to 60 Mpc, the third subsample contains the segments with lengths from 90 to 100 Mpc, and the fourth subsample contains all of the segments with lengths up to 100 Mpc. Based on formula (8), we can establish the analytical dependence $N(a)/N$ and estimate the fractal dimension of the distribution on various spatial scales. Table gives the results of our computations.

Figures 3 and 4 show a plot of $(N(a)/N)$ for the entire set of segments of various lengths (up to 100 Mpc) for the southern Galactic sky on linear (Fig. 3) and logarithmic (Fig. 4) scales. According to formula (8), this plot allows us to estimate the fractal dimension of the galaxy distribution in space (i.e., to determine $D = 3 - \alpha$). The exponent α specifies the

Table

Catalog	Number of galaxies with $M < -17$	Cylinder length, Mpc	$D = 3 - \alpha$	R	σ_{fit}
LEDA_S	6467	$0-100$	2.02	243.16	0.015
LEDA_S	"	$90-100$	2.01	245.03	0.041
LEDA_S	"	$50-60$	1.98	216.49	0.025
LEDA_S	"	$0-50$	2.18	439.64	0.028
LEDA_N	7265	$0-100$	2.12	331.44	0.013
LEDA_N	"	$90-100$	2.08	300.10	0.041
LEDA_N	"	$50-60$	2.07	280.45	0.019
LEDA_N	"	$0-50$	2.22	515.69	0.027
LEDA_sector 1	1155	$50-200$	2.08	288.80	0.015
LEDA_sector 2	385	$50-200$	2.02	229.22	0.070
SDSS	1505	$0-250$	2.00	399.89	0.009

slope of this function. By varying α, we choose an optimum value in such a way that the slope of the derived function corresponds to the LEDA data with the minimum rms dispersion of the fit σ_{fit}, which is defined as the square root of the sum of the squares of the differences between the theoretical (solid line) and observed values of $N(a)/N$.

An important result is that b is equal to zero in all of the cases considered. This implies that the observed distribution is purely fractal for all cylinder lengths, and no homogeneous Poisson background is observed. As expected for fractal structures, the objects are clustered toward the ends of the segments, and the theoretical dependence (8) well describes the observations without the additional assumption about the presence of a homogeneous background.

For cylinders of various heights, we obtained dependences similar to those shown in Figs. 3 and 4. This implies that on different spatial scales, the galaxy distribution between the pairs of fixed galaxies obeys the same law (8) with a fractal dimension close to 2. The fitting parameters R and D in formula (8) and σ_{fit} for various lengths are listed in the table.

To demonstrate the efficiency of the method for narrow conical sectors, we considered the two cor-
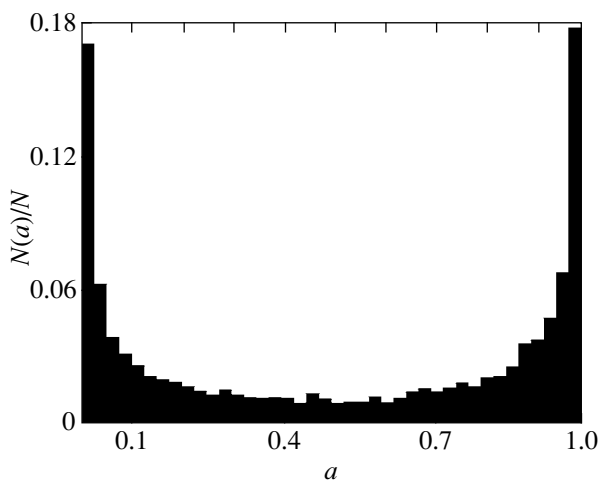

Fig. 3. Observational data corresponding to the distribution of galaxies from the LEDA database for all cylinders with sizes of up to 100 Mpc. We used a volume-limited sample of 6476 galaxies in the southern Galactic sky with $M < -17$.
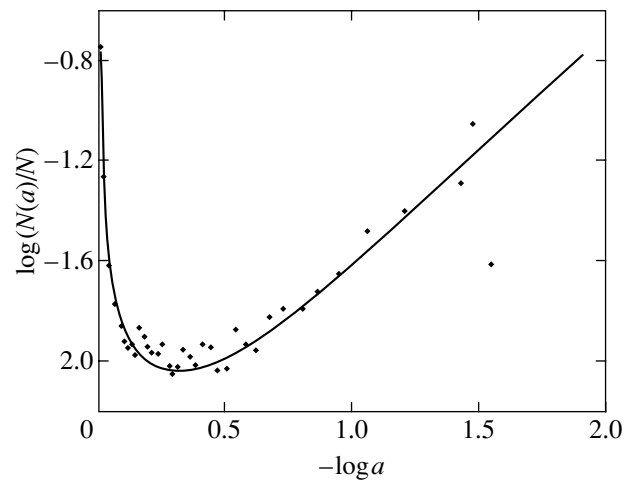

Fig. 4. Same as Fig. 3 on a logarithmic scale. The solid line corresponds to fit (8). For cylinders with scales up to 100 Mpc, the fractal dimension D is 2.02, and the constant b is 0.
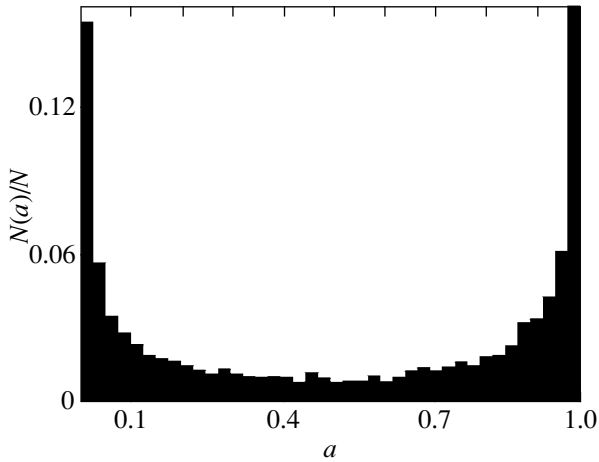
Fig. 5. Distribution of galaxies for a narrow LEDA sector along the cylinders with sizes from 50 to 200 Mpc. The number of galaxies in the volume-limited sample with $M < -17$ is $N = 1155$.
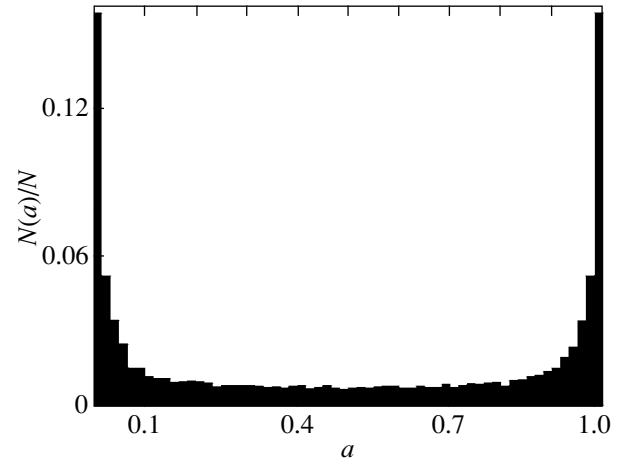

Fig. 7. Histogram for the distribution of galaxies from the EDR SDSS sample along the cylinders of all sizes up to 250 Mpc. The volume-limited sample of galaxies with $M < -17$ contains 1505 objects.
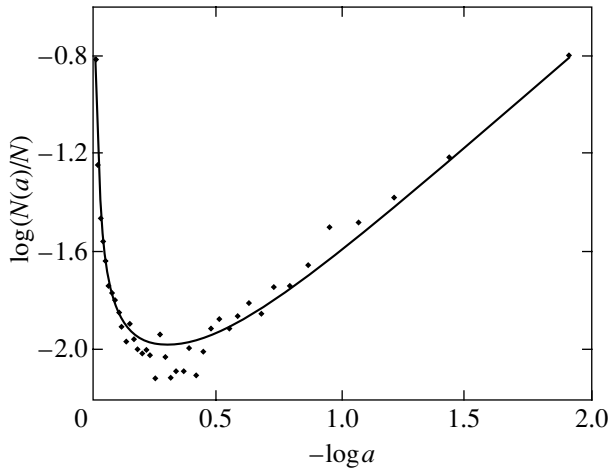

Fig. 6. Same as Fig. 5 on a logarithmic scale. The solid line corresponds to fit (8). For cylinders with scales up to 200 Mpc, the fractal dimension is $D = 2.08$, and the constant is $b = 0$.
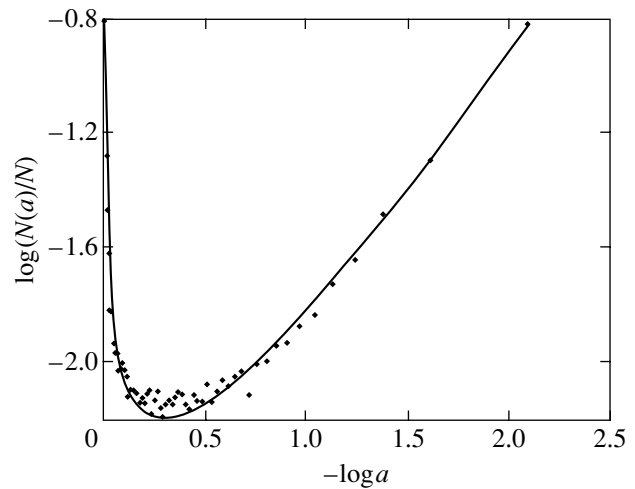

Fig. 8. Same as Fig. 7 on a logarithmic scale.

The Sample of EDR SDSS Galaxies

responding subsamples of LEDA galaxies presented in the table. The first sector contains 1155 galaxies with $M < -17$, $0.01 < z < 0.04$ and coordinates $\alpha = 143°-207°$, $\delta = 23°-28°$. Figure 5 shows the distribution of galaxies in the first sector between the pairs of fixed galaxies on a linear scale. The dots in Fig. 6 indicate the observational data, and the solid line indicates the fit (8). The parameters are $D = 2.08$, $\sigma = 0.015$.

Sector 2 contains 385 galaxies from the LEDA database with $M < -17$, $0.01 < z < 0.04$ and coordinates $\alpha = 0°-57°$, $\delta = -5°-0°$. The dependences for sector 2 are identical to those of sector 1, and the parameters D, σ, R are listed in the table.

To illustrate the application of our method to a sample of galaxies from a survey in the form of a narrow conical sector, we considered one band from EDR SDSS (the data were taken from the SDSS Web page). The table gives the results of our computations of the galaxy distribution in cylinders with lengths up to 250 Mpc in the sector with coordinates $\alpha = 145°-235°$, $\delta = -1°\!.3-1°\!.3$.

Figures 7 and 8 show plots of the distribution of 1505 galaxies along the cylinders of all sizes up to 250 Mpc. The fractal dimension D was estimated from formula (8) to be 2.00. In the latter case, there is apparently evidence for a homogeneous background. The constant of the homogeneous background is $b =$

0.0026. However, this issue requires more detailed analysis.

CONCLUSIONS

In this paper, we have suggested a new method for analyzing stochastic fractal structures and shown that it can be implemented in principle. Our analysis of a sample of LEDA galaxies indicated that the method of segments with two fixed points (the method of selected cylinders) can be successfully used to estimate the fractal dimension of the spatial structures of galaxies in surveys in the form of narrow conical sections. We used a sample of LEDA galaxies as an example to show that the estimated fractal dimension of the spatial distribution of galaxies agrees with the value obtained by the method of a one-point conditional number density (Silos-Labini *et al.* 1998).

The fractal dimension D for the samples of LEDA and EDR SDSS galaxies estimated by our method is 2.1 ± 0.1. The maximum fractal scale is limited by the length of the segments used in our analysis (200 Mpc). An analysis of magnitude-limited samples indicated an insignificant influence of selection effects on the suggested method. The capabilities of the new method will be analyzed in detail in a separate paper. Note only that the main advantage of the method of a conditional column density is that it allows scales comparable to the catalog depth to be analyzed for galaxy surveys in the form of conical sectors and small fields in the sky.

REFERENCES

1. Yu. V. Baryshev and Yu. L. Ezova, Astron. Zh. **74**, 497 (1997) [Astron. Rep. **41**, 436 (1997)].
2. A. Gabrielli, F. Sylos Labini, M. Joyce, and L. Pietronero, *Statistical Physics for Cosmic Structures* (Springer, Berlin, 2004, in press).
3. B. B. Mandelbrot, *The Fractal Geometry of Nature* (Freeman, New York, 1982).
4. V. J. Martinez and E. Saar, *Statistics of the Galaxy Distribution* (Chapman & Hall/CRC, New York, 2002).
5. G. Paturel, Astrophys. J., Suppl. Ser. **124**, 109 (1997).
6. L. Pietronero, Physica A **144**, 257 (1987).
7. F. Sylos-Labini, M. Montuori, and L. Pietronero, Phys. Rep. **293**, 61 (1998).

Translated by A. Dambis

Instability of a Thin Photoevaporable Circumstellar Envelope

K. V. Krasnobaev*

Moscow State University, Vorob'evy gory, Moscow, 119992 Russia

Received January 8, 2004

Abstract—We investigate the stability of a dense neutral shell that is accelerated outward by the hot-gas pressure and that loses its mass through photoionization by radiation from the central star. We assume the H I shell to be thin and use the Lagrangian coordinates to describe its motion. We show that a flow accompanied by cumulative effects emerges during the nonlinear development of the instability. We estimate the influence of the radiative cooling rate on the motion and determine parameters of the gas in the cumulative region. The results obtained are compared with the observations of the nebulae NGC 7293 and NGC 2392. © *2004 MAIK "Nauka/Interperiodica"*.

Key words: *interstellar medium, gaseous nebulae, planetary nebulae.*

Since the question about the origin and parameters of the dense neutral condensations observed in the vicinity of hot stars is of considerable interest in connection with star-formation problems, it figures prominently in studies of the dynamics and evolution of H II regions (Spitzer 1978; Pottash 1984; Osterbrock 1989).

The condensations are currently believed to originate either from the development of a certain type of instability (mainly ionization–shock front instability) or from an enhancement of inhomogeneities behind converging shocks (Vandervoort 1962; Axford 1964; Krasnobaev 1971; Capriotti 1973; Burdyuzha and Ruzmaĭkina 1974; Elmegreen and Lada 1977; Giuliani 1979; Garcia-Segura and Franco 1996; Willams 1999). In particular, Capriotti (1973) showed that globules could be formed in expanding nebulae (such as, e.g., NGC 7293), because the neutral shell is unstable. In the latter case, classical ideas about the evolution of perturbations whose wavelength l is small compared to the shell thickness h were used to analyze the fragmentation of a neutral gas moving with a constant acceleration. If, however, we take into account the fact that h is limited, then, as we show below, cumulative effects that significantly change the structure of the condensations can manifest themselves in the limiting case $h \ll l$ at the expansion phase of the shell when its mass is about a third of the nebular mass M_n.

To reveal the peculiarities of this structure, let us consider the stability of a thin ($h \ll l$) shell that undergoes acceleration g and that loses its mass under radiation from the central star. In general, the external

*E-mail: `vkkaor22@mtu-net.ru`

ionizing flux Φ and the acceleration g are assumed to depend on time t.

The equations that describe the motion of the shell can be obtained by generalizing the equations derived by Ott (1972) to the case where a D-type ionization front is the inner boundary of the flat layer. As a result, the system of equations for the coordinates x and y of the layer and the particle mass $M(\xi, t)$ referred to its initial value in Lagrangian coordinates ξ and t takes the form

$$M\frac{\partial^2 x}{\partial t^2} = \left(-g + \frac{\partial M}{\partial t}\frac{U_r}{\sqrt{\left(\frac{\partial x}{\partial \xi}\right)^2 + \left(\frac{\partial y}{\partial \xi}\right)^2}}\right)\frac{\partial y}{\partial \xi},$$

$$M\frac{\partial^2 y}{\partial t^2} = \left(g - \frac{\partial M}{\partial t}\frac{U_r}{\sqrt{\left(\frac{\partial x}{\partial \xi}\right)^2 + \left(\frac{\partial y}{\partial \xi}\right)^2}}\right)\frac{\partial x}{\partial \xi},$$

$$\frac{\partial M}{\partial t} = -\gamma\frac{\partial x}{\partial \xi}.$$

Here, $g = \triangle p/\sigma$, $\gamma = m_{\rm H}\Phi/\sigma = \rho U_r/\sigma$, where $\triangle p$ is the difference between the pressures on the inner and outer sides of the shell, $\sigma = {\rm const}$ is the surface density at the initial time, $m_{\rm H}$ is the hydrogen atomic mass, and ρ and U_r are the density and relative velocity of the plasma flowing away from the ionization front, respectively. In Eqs. (1), we assume that the photons propagate along the y axis (i.e., the diffuse radiation is disregarded) and that the velocity of the ionization front relative to the neutral particles is low compared to the gas velocity in the layer.

Consider the motion of a flat homogeneous layer as the main motion, with the y axis being perpendicular to the layer. The solution of Eqs. (1) may then be written as

$$x = \xi, \quad y = y_0(t), \quad M = M_0(t), \qquad (2)$$

$$M_0 \frac{\partial^2 y_0}{\partial t^2} = g + \gamma U_r, \quad M_0 = 1 - \int_0^t \gamma(t)dt.$$

Assuming then that $x = \xi + x'$, $y = y_0(t) + y'$, $M = M_0(t) + M'$ and that x', y', M' are small, we find after linearizing (1) that

$$M_0 \frac{\partial^2 x'}{\partial t^2} = -(g + \gamma U_r)\frac{\partial y'}{\partial \xi}, \qquad (3)$$

$$M_0 \frac{\partial^2 y'}{\partial t^2} = (g + \gamma U_r)\left(\frac{\partial x'}{\partial \xi} - \frac{M'}{M_0}\right),$$

$$\frac{\partial M'}{\partial t} = -\gamma \frac{\partial x'}{\partial \xi}.$$

When deriving Eqs. (3), we disregarded the pressure and density perturbations in the ionized gas. The condition under which this approximation is justified can be inferred by considering the wave motions in an H II region whose outer boundary is a neutral shell. Indeed, using the formula from our previous paper (Krasnobaev 2000) to estimate the wave damping time τ_d, we obtain

$$\tau_d = \frac{3}{4}\frac{1}{\tau_T}\left(\frac{l}{\pi a_2}\right)^2, \quad l \gg a_2\tau_T, \qquad (4)$$

where a_2 is the isothermal speed of sound in the H II region, and τ_T is the thermal relaxation time.

Consequently, if τ_i is the characteristic perturbation growth time, then the validity range of Eqs. (3) is limited by the inequality

$$\tau_d \ll \tau_i. \qquad (5)$$

Equations (3) do not include the possible variations in flux Φ that arise from the change in the optical depth of the plasma downstream of the ionization front when the shell is displaced relative to the unperturbed location. These variations are small if

$$l \ll l_r = \frac{m_H U_r}{\beta\rho}, \qquad (6)$$

where β is the total coefficient of photorecombination to excited hydrogen atomic levels, and the order of magnitude of l_r follows, for example, from an analysis of the stability of ionization fronts that propagate through an accelerating gas (Baranov and Krasnobaev 1977).

In general, the solution of Eqs. (3) can be sought in the form $(x', y', M') \propto \exp(ik\xi)$, $k = 2\pi/l$, and the proportionality coefficients are functions of t.

The problem of the stability of motion (2) then reduces to solving a system of ordinary differential equations with time-dependent coefficients. For arbitrary $g(t)$ and $\gamma(t)$, this problem can be solved only numerically. Nevertheless, some of the peculiarities of the motion attributable to mass loss and variable acceleration can be revealed by considering particular analytical solutions of Eqs. (3).

Thus, for example, the influence of $\gamma(t)$ on τ_i can be taken into account if it is considered that for a flat layer, apart from the decrease in M_0, Φ generally also decreases because of the increase in the optical depth of the plasma downstream of the ionization front. In this case, it would be natural to assume roughly that

$$\lambda = \frac{g + \gamma U_r}{M_0} = g_0 = \text{const}, \qquad (7)$$

$$\frac{\gamma}{M_0} = g_1 = \text{const}.$$

Clearly, a uniformly accelerated unperturbed motion of the layer corresponds to equalities (7). It should also be noted that, in view of (2) and (7), $\gamma(t)$ is not an arbitrary function, but satisfies the equation $d\gamma/dt = -g_1\gamma$ and, hence, $\gamma = g_1\exp(-g_1 t)$.

Assuming then that $(x', y', M') \propto \exp(\alpha t + ik\xi)$, we derive a dispersion relation from (3) in the form

$$\frac{\alpha}{\alpha_0} - \left(\frac{\alpha_0}{\alpha}\right)^3 = \frac{g_1}{\alpha_0}, \qquad (8)$$

where $\alpha_0 = \sqrt{kg_0}$ is the growth rate of the classical Rayleigh–Taylor instability, and the parameter g_1/α_0 is proportional to the mass lost per unit area of the layer in time α_0^{-1}. The following expression of g_1/α_0 as a function of the characteristic density of the neutral atoms ρ_0, the layer thickness h, and the wavelength l (assuming that $U_r \sim a_2$) is useful for estimates:

$$g_1 = \frac{\rho a_2}{\sigma M_0}, \quad g_0 = \frac{2\rho a_2^2}{\sigma M_0}, \qquad (9)$$

$$\frac{g_1}{\alpha_0} = \sqrt{\frac{1}{4\pi M_0}\frac{\rho l}{\rho_0 h}}.$$

The plot of α against g_1/α_0 that corresponds to (8) is shown in Fig. 1. We see that the outflow of matter from the ionization front destabilizes the layer by increasing α compared to α_0.

Let us now consider the stability of a layer whose acceleration varies with time. Since such variations are determined by the large-scale dynamics of the H II region (in particular, by the increase or decrease in Φ), an analysis of the solutions of Eqs. (3) with both $\dot{\lambda} = d\lambda/dt > 0$ and $\dot{\lambda} < 0$ is of considerable interest.

The corresponding particular solutions can be found if the characteristic values of ρ, ρ_0, l, and h in (9) are such that $\rho l \ll \rho_0 h$ (there is no contradiction here, because, although $h \ll l$ for a thin layer, $\rho \ll \rho_0$ due to the large temperature difference between the neutral and ionized gases). The mass loss is then negligible and $M \approx 1$. Consequently, $x'(\xi, t)$ and $y'(\xi, t)$ satisfy linear equations with variable coefficient $\lambda(t)$; these equations can also describe the nonlinear evolutionary stage of the perturbations. Indeed, if the photon flux crossing the ionization front depends weakly on the shape of the layer (e.g., when U_r is small enough compared to a_2), then making appropriate changes to the expression for $\partial M / \partial t$ in Eqs. (1) yields a system of equations of form (3) with $M \approx 1$. In general, exact solutions of the nonlinear equations (1) are difficult to find, although, as can be easily verified, there are self-similar solutions with the initial data $x' = y' = 0$ and $\partial y' / \partial t \propto \sqrt{\xi}$ that depend on the variable $t\sqrt{\lambda / \xi}$. However, such solutions have a limited validity range and are not considered below. We only note that, as our numerical calculations show, U_r affects only slightly the characteristics of the self-similar motion.

Now, let $\lambda(t)$ vary as

$$\lambda = \frac{\lambda_0}{(t - t_0)^2}, \quad \lambda_0 = \text{const}, \quad (10)$$

$$t_0 = \text{const},$$

where $|t_0|$ is the characteristic time of change in λ, and $d\lambda/dt > 0$ for $t_0 > 0$ and $d\lambda/dt < 0$ for $t_0 < 0$.

Given (10), the perturbations in the shape of the layer are proportional to $(t - t_0)^\alpha \exp(ik\xi)$, and α is related to k and λ_0 by

$$\alpha^2 (\alpha - 1)^2 = k^2 \lambda_0^2. \quad (11)$$

The values of $\alpha = 1/2 \pm \sqrt{1/4 + k\lambda_0}$ correspond to aperiodic perturbations growing with time; $\alpha^+ = 1/2 - \sqrt{1/4 + k\lambda_0}$ and $\alpha^- = 1/2 + \sqrt{1/4 + k\lambda_0}$ should be chosen for unstable motion with $\dot\lambda > 0$ and $\dot\lambda < 0$, respectively. Decreasing (with increasing t) perturbations in the shape of the layer or the particle velocities in it correspond to the other two roots of Eq. (11).

To analyze the solutions of Eq. (11) characterized by α^+ and α^-, it is appropriate to introduce the parameter $r = \sqrt{k\lambda(0)}|t_0| = \sqrt{k\lambda_0}$. Clearly, the variations in λ are insignificant when $r \gg 1$. In this case, the unperturbed layer moves with uniform acceleration, and, as Zonenko and Chernyĭ (2003) showed, the growth of perturbations is accompanied by the appearance of a cuspidal point in the curve $y(x)$ followed by the collapse of the adjacent parts of the
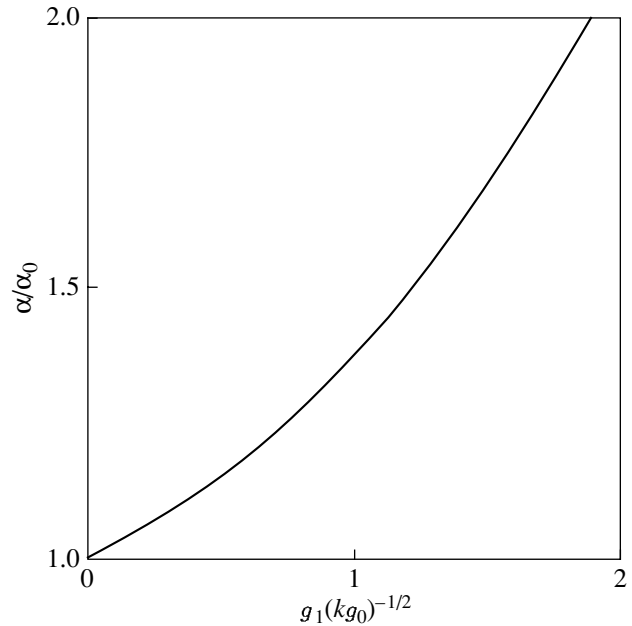

Fig. 1. Instability growth rate versus mass-loss rate.

deformed layer. As a result, inhomogeneities (fingers) oriented along the y axis in which matter of the layer is accumulated as t increases are formed.

If, however, r is finite, then both the collapse time t_c and the y component of the velocity $V_c(t_c)$ relative to the unperturbed layer can differ significantly from their values at $\lambda = \lambda(0)$.

Let t_c^+, t_c^0, and t_c^- be the collapse times for $\dot\lambda > 0$, $\lambda = \lambda(0)$, and $\dot\lambda < 0$, respectively. We then obtain

$$\frac{t_c^+}{t_0} = 1 - \left(\frac{1 - 2\xi}{2\varepsilon \sin 2\pi\xi} \right)^{1/\alpha^+}, \quad (12)$$

$$\frac{t_c^0}{|t_0|} = \frac{1}{r} \ln \left(\frac{1 - 2\xi}{2\varepsilon \sin 2\pi\xi} \right),$$

$$\frac{t_c^-}{t_0} = 1 - \left(\frac{1 - 2\xi}{2\varepsilon \sin 2\pi\xi} \right)^{1/\alpha^-}.$$

Here, ξ is the Lagrangian coordinate of the particle, ε is the amplitude of the initial perturbation in the shape of the layer (ξ and ε are referred to l), and the collapse time t_c is determined from the condition that the particle is located at the point with $x = l/2$.

Using (12), we can easily find the dependence $V_c(t_c)$. As an example, Fig. 2 shows the curves $V_c(t_c)$ at various r for $\varepsilon = 1/(2\pi e)$ (in Fig. 2, t_c and V_c are referred to $|t_0|$ and $V_c(0) = (\partial y'/\partial t)_{0,0}$, respectively). The coordinate $\xi = 0.2$ corresponds to the largest values of t_c for all curves; i.e., at the collapse time that corresponds to this value of ξ, the mass of the matter in the cumulative region is equal to 3/5 of
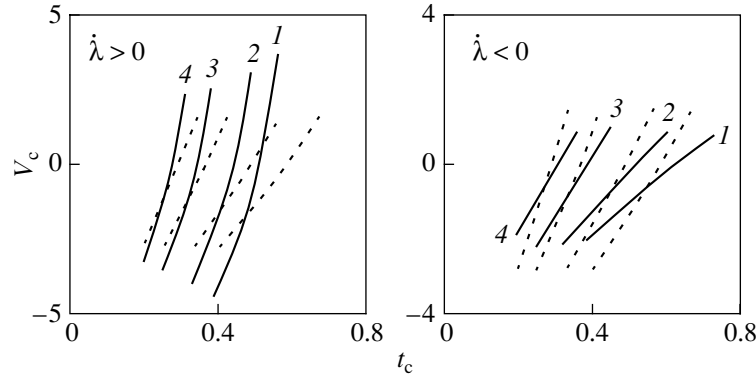
Fig. 2. Gas velocity V_c at the onset of collapse versus time t_c. The solid curves $1-4$ correspond to $r = \sqrt{2\pi}$, 3, 4, and 5. The dashed curves indicate the dependences $V_c(t_c)$ at $\lambda = \lambda(0)$ and for the same r.

the mass of the unperturbed layer contained in the interval $0 \leq \xi \leq 1$. The shape of the layer with the filament formed by the time in question is shown in Fig. 3, where the coordinates x and y are expressed in units of l, $\lambda = \lambda(0)$.

Comparing curves $1-4$ in Fig. 2 with $V_c(t_c)$ at $\lambda = \lambda(0)$ and the same r (dashed lines), we can see that an increase in λ causes V_c to increase faster than in the case of uniformly accelerated motion. If, alternatively, $\dot{\lambda} < 0$, then the increase in V_c naturally slows down. Characteristically, there is a significant difference between the particle velocities in the condensation, and the end of the condensation that moves with an increasing velocity is ahead of the unperturbed layer starting from a certain time.

DISCUSSION AND CONCLUSIONS

Let us now consider the possible appearance of the cumulative effects investigated above using the nebulae NGC 7293 and NGC 2392 as examples. The information about these nebulae used below is contained in the monographs by Pottash (1984) and Khromov (1983), and a high-resolution image of NGC 2392 is accessible at http://antwrp.gsfc.nasa.gov./apod/archivepix.html.

As regards NGC 7293, we use a rough nebular expansion model suggested by Capriotti (1973). Denote the radius and mass of the ionized part of the nebula by R_i and M_i, respectively, and the radius of the nebula upon reaching which its entire mass M_n will be ionized by $R_n = 3 \times 10^{17}$ cm. According to the model, the mass of the neutral shell M_e, its thickness h, acceleration g, and the mass-loss rate γ are related to R_i, M_i, R_n, M_n, and the isothermal speed of sound a_1 in the H I region by

$$M_i = (R_i/R_n)^{3/2} M_n, \qquad (13)$$
$$M_e = [1 - (R_i/R_n)^{3/2}] M_n,$$

$$\lambda = \frac{6a_2^2}{R_n} \frac{(R_i/R_n)^{1/2}}{1 - (R_i/R_n)^{3/2}}, \qquad h = \frac{a_1^2}{\lambda}.$$

Since, in general, $a_1 \approx 10^{-1} a_2$, it follows from (13) that the flat-layer approximation is justified if R_i is not too small compared to R_n.

Next, let us estimate the scales l that agree with inequalities (5) and (6). Taking $\tau_i \sim (l/2\pi\lambda)^{1/2}$ for our estimates and using (4) for τ_d, we represent (5) as

$$l \ll l_d = (4\tau_T/3)^{2/3} (\pi a_2)^{4/3} (2\pi\lambda)^{-1/3}.$$

Assuming then that the gas temperature in the H II region is 10^4 K, $\beta \approx 2 \times 10^{-13}$ cm^{3}s^{-1}, $M_n \approx 0.2 M_\odot$, and $\tau_T \approx (6.3 \times 10^{11} m_H/\rho)$ s (Spitzer 1978), we find the range of acceptable l:

$$h < l < \min(l_d, l_r)$$

or

$$\frac{1 - (R_i/R_n)^{3/2}}{2(R_i/R_n)^{1/2}} < 10^{-15} l < \min \left\{ 5.9 \left(\frac{R_i}{R_n} \right)^{5/6} \right.$$

$$\tag{14}$$

$$\times \left[1 - \left(\frac{R_i}{R_n} \right)^{3/2} \right]^{1/3}, 3.1 \left(\frac{R_i}{R_n} \right)^{3/2} \left. \right\}.$$

It follows from (14) that, for example, at $R_i \sim 0.8 R_n$, about a third of the nebular mass can be concentrated in growing perturbations with scale sizes of $\sim 10^{15}$ cm. Estimates based on the rough model for the expansion of NGC 7293 suggested by Capriotti (1973) show that for perturbations with $l \sim 10^{15}$ cm, inequalities (14) hold when the mass of the shell is smaller than or $\sim 0.3 M_n$. Here, however, the following should be noted:

In the model by Capriotti (1973), the shell fragments even at $R_i \sim 0.4 R_n$, with the fragment sizes being $l \sim h/2 < l_d$ (i.e., $l \sim 3 \times 10^{14}$ cm). However,
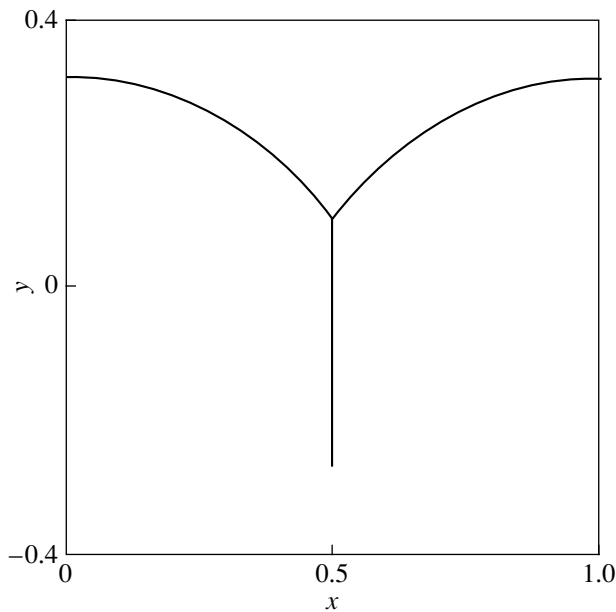
Fig. 3. Shape of the layer with a formed filament ($\lambda = \lambda(0)$).

the l range defined by (14) then formally narrows appreciably, because h increases and l_r decreases. At the same time, fragmentation leads to a decrease in M_e and an increase in λ, causing the effective thickness of the neutral layer to decrease. Thus, (apart from globule-like structures) neutral condensations with significantly differing longitudinal and transverse sizes and with high radial-velocity dispersion can also appear under fragmentation conditions. Interestingly, structures of this type are observed, in particular, in the image of the planetary nebula NGC 2392. The emergence of such structures makes it possible to explain the observation of radially oriented sequences of globules, which often show up against the background of extended condensations. In other words, the radial filaments are generally not (as is occasionally interpreted) shadow regions shielded against direct ionizing radiation from the central star, but serve as the source of globule matter. The mass of the gas contained in the radial filaments, of course, depends on the spectrum and amplitude of the initial perturbations. However, we can estimate an upper limit for the number of condensations N and their characteristic masses M_f. In particular, assuming that $l \sim 10^{15}$ cm for NGC 7293, we obtain $N \sim 10^5$ and $M_f \gtrsim 10^{27}$ g at $R_i \sim 0.4 R_n$. These values of N and M_f are close to those found by Capriotti, although the condensations now have a distinctly different structure.

We emphasize that the conclusions formulated above are based on a rough model of the shell. Therefore, a more accurate allowance for the ionized gas motions, the radiative transfer in the H II region, the fragmentation of the neutral layer, and its interaction with the interstellar medium surrounding the nebula would be appropriate.

In conclusion, note that manifestations of the cumulative effects considered above may also be expected in other objects that contain fairly thin and dense layers of gas (e.g., in supernova remnants).

ACKNOWLEDGMENTS

REFERENCES

1. W. I. Axford, Astrophys. J. **140**, 112 (1964).
2. V. B. Baranov and K. V. Krasnobaev, *Hydrodynamic Theory of Cosmic Plasmas* (Nauka, Moscow, 1977) [in Russian].
3. V. V. Burdyuzha and T. V. Ruzmaĭkina, Astron. Zh. **51**, 346 (1974) [Sov. Astron. **18**, 201 (1975)].
4. E. R. Capriotti, Astrophys. J. **179**, 495 (1973).
5. B. G. Elmegreen and C. J. Lada, Astrophys. J. **214**, 725 (1977).
6. G. Garcia-Segura and J. Franco, Astrophys. J. **469**, 171 (1996).
7. J. L. Giuliani, Astrophys. J. **233**, 280 (1979).
8. G. S. Khromov, *Planetary Nebulae: Physics, Evolution, Cosmogony* (Nauka, Moscow, 1983) [in Russian].
9. K. V. Krasnobaev, Dokl. Akad. Nauk SSSR **196**, 1291 (1971) [Sov. Phys. Dokl. **16**, 92 (1971)].
10. K. V. Krasnobaev, Astrophys. Space Sci. **274**, 307 (2000).
11. D. E. Osterbrock, *Astrophysics of Gaseous Nebulae and Active Galactic Nuclei* (Univ. Sci. Book, California, 1989).
12. E. Ott, Phys. Rev. Lett. **29**, 1429 (1972).
13. S. Pottash, *Planetary Nebulae* (Reidel, Dordrecht, 1984; Mir, Moscow, 1987).
14. L. Spitzer, Jr., *Physical Processes in Interstellar Medium* (Wiley, New York, 1978; Mir, Moscow, 1981).
15. P. O. Vandervoort, Astrophys. J. **135**, 212 (1962).
16. R. J. R. Willams, Mon. Not. R. Astron. Soc. **310**, 789 (1999).
17. S. I. Zonenko and G. G. Chernyĭ, Dokl. Akad. Nauk **390**, 46 (2003) [Dokl. Phys. **48**, 239 (2003)].

Translated by V. Astakhov

Possible Variability of the Magnetic Field of T Tau

D. A. Smirnov[1*], S. A. Lamzin[1**], S. N. Fabrika[2], and G. A. Chuntonov[2]

[1]*Sternberg Astronomical Institute, Universitetskiĭ pr. 13, Moscow, 119992 Russia*

[2]*Special Astrophysical Observatory, Russian Academy of Sciences, Nizhniĭ Arkhyz,*
357147 Karachai-Cherkessian Republic, Russia

Received December 10, 2003

Abstract—Using the Main Stellar Spectrograph of the 6-m Special Astrophysical Observatory telescope equipped with a polametric analyzer, we measured the longitudinal magnetic field component $B_{||}$ for the T Tauri stars T Tau and AS 507 on January 16 and 18 and February 15, 2003. For both stars, we determined only the upper limits on $B_{||}$ from photospheric lines: $+15 \pm 30$ G for T Tau and -70 ± 90 G for AS 507. The magnetic field of AS 507 was not measured previously, while $B_{||}$ for T Tau is lower than its values that we obtained in 1996 and 2002 ($B_{||} \simeq 150 \pm 50$ G), suggesting that the longitudinal magnetic field component in the photosphere of T Tau is variable. We also measured the longitudinal magnetic field component for T Tau in the formation region of the He I 5876 Å emission line. We found $B_{||}$ in this region to be $\simeq +650$, $\simeq +350$, and $\simeq +1100$ G on January 16, 18, and February 15, 2003, respectively. Our observations on January 18 and February 15 correspond to virtually the same phase of the star's rotation period, but the profiles of the He I 5876 Å line differ markedly on these two nights. Therefore, we believe that the threefold difference between the $B_{||}$ values on these nights does not result from observational errors. We discuss the possible causes of the $B_{||}$ variability in the photosphere and the magnetosphere of T Tau. © 2004 MAIK "Nauka/Interperiodica".

Key words: *stars—variable and peculiar, T Tau, AS 507, T Tauri stars, magnetic field, disk accretion.*

INTRODUCTION

T Tauri stars (TTSs) are young ($t < 10^7$ years) low-mass ($M \leq 2M_\odot$) stars at the stage of gravitational contraction toward the main sequence. T Tau belongs to the so-called classical T Tauri stars (CTTSs) whose activity is attributable to mass accretion from a (protoplanetary) disk, while AS 507 most likely belongs to weak-line T Tauri stars (WTTSs) whose line and continuum variability is attributable to solar-type activity (Herbig and Bell 1988; Bertout 1998).

The magnetic fields in both CTTSs and WTTSs not only determine the patterns of their activity, but also play a fundamental role in the evolution of the stellar angular momentum. Therefore, one of the main questions in the physics of young stars is the magnetic field strength and topology. At present, the magnetic field strength is known for fewer than ten TTSs, because the fields are difficult to measure for these objects.

Using the fact that the magnetic field changes the line equivalent widths, depending on the Lande

factor, Guenther *et al.* (1999) and Johns-Krull *et al.* (2001) found, in particular, that the surface-averaged magnetic field strength of T Tau is $B > 2$ kG. On the other hand, Smirnov *et al.* (2003) found the longitudinal magnetic field component $B_{||}$ on the surface of T Tau in 1996 and 2002 to be $\simeq +150 \pm 50$ G, i.e., an order of magnitude smaller than B_s. Both a significant deviation of the stellar field from a dipole and a large inclination of the magnetic dipole axis to the rotation axis of the star could be responsible for such a large discrepancy. To find out which of the explanations is correct, we remeasured $B_{||}$ for T Tau in the winter of 2003. Our results are reported in this paper. In addition, we measured the mean $B_{||}$ for AS 507.

The method of magnetic field measurements used here, as in our previous paper (Smirnov *et al.* 2003), is based on the fact that for the Zeeman splitting of the so-called σ component, the lines are circularly polarized; the components with opposite polarizations are located on both sides of the central wavelength λ_0. If the magnetic field in the line formation region has a longitudinal (directed along the line of sight) component $B_{||}$, then the lines observed in right-hand and left-hand polarized light will be shifted from one

[*]E-mail: `danila@sai.msu.ru`

[**]E-mail: `lamzin@sai.msu.ru`

another by (Babcock 1958):

$$\Delta\lambda_{rl} \simeq 9.3 \times 10^{-10} g\lambda_0^2 B_{\|} \quad m\text{Å}, \qquad (1)$$

where g is the Lande factor of the line under consideration. The wavelength in (1) is in Å, and $B_{\|}$ is in G. This relation allows the mean longitudinal magnetic field component in the line formation region to be determined by measuring $\Delta\lambda_{rl}$ from two spectra taken in right-hand and left-hand polarized light.

OBSERVATIONS AND REDUCTION TECHNIQUES

The spectra of T Tau and AS 507 were obtained on January 16 and 18 and February 15, 2003, on the 6-m Special Astrophysical Observatory telescope using the Main Stellar Spectrograph (Panchuk 2001) equipped with a circular polarization analyzer (Chuntonov 1997). Spectra in the range 5700−6000 Å were taken with a $2K \times 2K$ CCD detector. The spectrograph slit width, $0\overset{''}{.}5$, provided a spectral resolution $R \simeq 15\,000$. The reciprocal dispersion was 0.17 Å per pixel. The weather conditions on the observing nights were stable, with the seeing being within $1\overset{''}{.}5$ most of the time.

We reduced the spectra using the MIDAS software package. To measure the difference between the line positions in the spectra with opposite polarizations, we used a cross-correlation method. This method makes it possible to measure the shift of the line as a whole and has a low sensitivity to errors in continuum placement.

In addition to T Tau and AS 507, we also observed the magnetic star HD 30466 and the giant ϵ Tau; the latter was used as a zero-field standard (see below). Table 1 contains basic information about our observations: the apparent magnitude V of the object, the number of observed pairs of spectra n, the total observing time for the star t_e in minutes, and the signal-to-noise ratio S/N per pixel for each spectrum.

To identify lines in the spectra of T Tau and AS 507, we used information about their relative intensities from the VALD database (Kupka *et al.* 1999) by assuming that $T_{eff} = 5250$ K, $\log g = 3.73$ (White and Ghez 2001) for T Tau and $T_{eff} = 5000$ K and $\log g = 4.0$ (Herbig 1977; Padgett 1996) for AS 507.

To take into account the systematic instrumental errors, we organized the observations as follows. Between exposures, the phase compensator was rotated in such a way that the right-hand and left-hand polarized spectra were interchanged on the CCD array. Let $\Delta\lambda_{rl}^{(1)}$ be the difference between the positions of a line in the spectra with opposite polarizations measured at the initial position of the phase compensator,

Table 1. Observations

Object	V	n	t_e, min	S/N
ϵ Tau	4.9	4	8	400
T Tau	10.0	12	580	150
AS 507	10.3	2	80	150
HD 30466	7.3	1	24	200

and $\Delta\lambda_{rl}^{(2)}$ be the same difference measured after the rotation of the compensator. Then the value

$$\Delta\lambda_{rl} = \frac{\Delta\lambda_{rl}^{(2)} - \Delta\lambda_{rl}^{(1)}}{2}$$

will be free from systematic errors, with the main error being attributable to the tilt of the spectrograph slit. The same quantity was calculated for all measurable lines. Thus, two exposures of the star are required to measure the line shift needed to calculate $B_{\|}$ using Eq. (1).

When an absorption feature was a blend of lines comparable in intensity, we used the effective Lande factor

$$g_{eff} = \frac{\Sigma d_i g_i}{\Sigma d_i},$$

i.e., the weighted mean component of the blend averaged over the central depths d_i taken from the VALD database.

RESULTS

To test our procedure for magnetic field measurements, we observed the magnetic star HD 30466. For this star, Babcock (1958) found $B_{\|} = +2320 \pm 340$ and $B_{\|} = +1890 \pm 130$ G from two independent observations, while Smirnov *et al.* (2003) derived $B_{\|} \simeq 2.0$ kG by estimating the field from only one line, CrI 6661 Å. Based on our observations of 2003, we obtained $B_{\|} \simeq 2.1$ kG for HD 30466 using the CrI 5710 Å line to estimate the field.

The results of our magnetic field measurements from absorption lines of T Tau and AS 507 are presented for each of the three nights in the third column of Table 2. Since the absorption lines are formed in the photospheres of these stars, the measured $B_{\|}$ values pertain to the surfaces of T Tau and AS 507.

The mean values of $B_{\|}$ for T Tau and AS 507 do not differ from zero, within the error limits. To independently check the validity of our allowance for the systematic errors, we observed the star ϵ Tau (G9.5 III). Since this star is a giant, it would be natural to expect that the magnetic field strength in its photosphere is close to zero. Indeed, in 2002,

Table 2. Results of the observations

Date, 2003	Object	$B_{\parallel}$, G	
		photosphere	He I
Jan. 16	T Tau	$+10 \pm 45$	$+640, +720$
	AS 507	-70 ± 85	
Jan. 18	T Tau	-40 ± 50	$+390, +320$
	ϵ Tau	$+7 \pm 11$	
Feb. 15	T Tau	$+75 \pm 50$	$+1090, +1200$
	ϵ Tau	-3 ± 12	

we found $B_{\parallel} = -0.5 \pm 8$ G for this star (Smirnov *et al.* 2003). This time, having reduced the spectra of ϵ Tau using to the same techniques as that for the spectra of T Tau and AS 507, we obtained $B_{\parallel} = +2 \pm 10$ G for this star. This suggests that our method for eliminating the systematic errors is fairly efficient, and that the observed scatter of $B_{\parallel}$ values for T Tau and AS 507 is attributable to random measurement errors.

The histograms in Fig. 1 show the number of absorption lines used to obtain a particular value of $B_{\parallel}$ in the range ± 100 G for T Tau and AS 507. These histograms were constructed from all of the measurements, because the mean $B_{\parallel}$ values for each night are equal, within the error limits. We see that
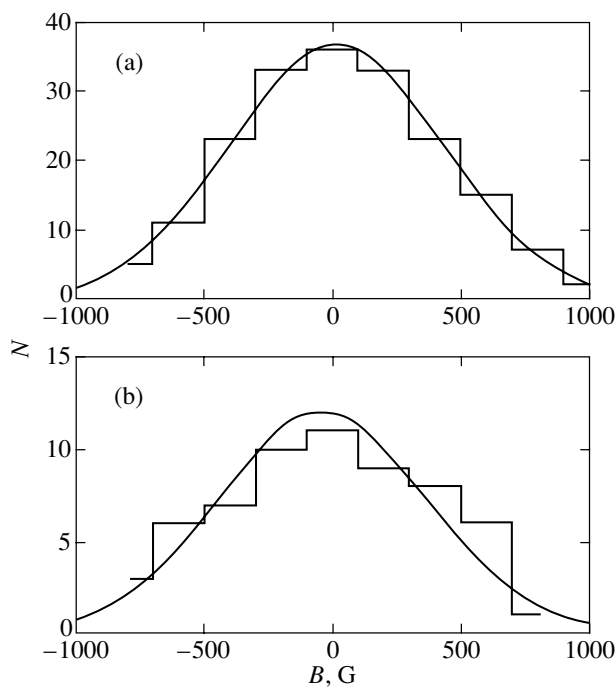

Fig. 1. Histogram showing the number of lines, N, used to obtain a particular value of $B_{\parallel}$ in the range ± 100 G for T Tau (a) and AS 507 (b). The histogram was fitted by a Gaussian for each star.

the histogram for T Tau is well fitted by a Gaussian whose peak corresponds to $B_{\parallel} \simeq +15$ G. A Gaussian pattern of the $B_{\parallel}$ distribution is not so obvious for AS 507, but we attribute this fact to insufficient statistics.

The helium emission lines of CTTSs are currently believed to be formed in accreted matter in the magnetosphere of a young star, i.e., outside its photosphere. Therefore, we separately measured $B_{\parallel}$ for T Tau from the profile of the He I 5876 Å line (this line is not observed in the spectrum of AS 507). The results of these measurements (two measurements on each of the three nights) are given in the fourth column of Table 2. They differ markedly from $B_{\parallel}$ in the photosphere. The largest value (~ 1 kG) was obtained on February 15, 2003 (Fig. 2). Note that for BP Tau, $B_{\parallel} \sim 2.5$ kG in the formation region of the He I 5876 Å line (Johns-Krull *et al.* 1999a) and $B_{\rm s} = 2.1 \pm 0.3$ kG at the photospheric level (Johns-Krull *et al.* 1999b).

CONCLUDING REMARKS

Both program stars exhibit periodic brightness variations which are probably attributable to the axial rotation of the stars. The axial rotation periods of T Tau and AS 507 are $\simeq 3.43^{\rm d}$ (Herbst *et al.* 1986) and $\simeq 2.80^{\rm d}$ (Chugaĭnov *et al.* 1995), respectively. As has been noted above, the mean values of $B_{\parallel}$ in the photospheres of T Tau and AS 507 for individual nights are equal, within the error limits. Therefore, we were unable to check how $B_{\parallel}$ varies as the star rotates.

Since the magnetic field of AS 507 had not been measured previously, we have nothing with which to
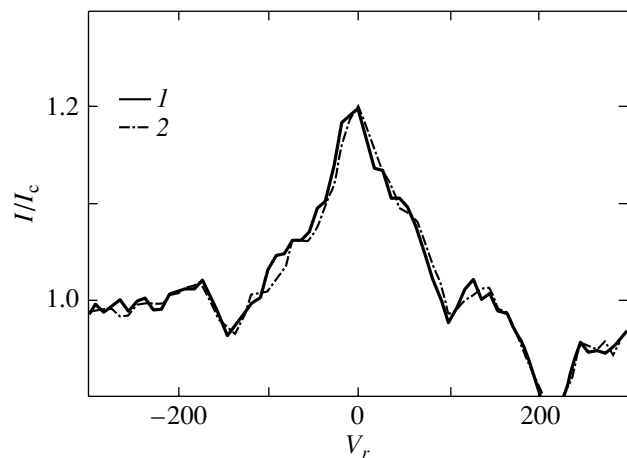

Fig. 2. Profiles of the He I 5876 Å line in right-hand (*1*) and left-hand (*2*) polarized light for the spectrum of T Tau observed on February 15, 2003.
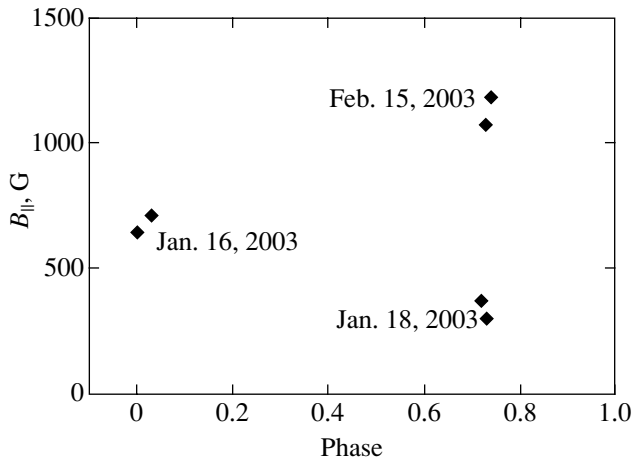
Fig. 3. $B_{\|}$ in the magnetosphere of T Tau versus axial rotation phase.

Fig. 4. Variations in the profiles of the He I 5876 Å line in the spectrum of T Tau from night to night. The date of observation is indicated for each profile on the left, while the mean $B_{\|}$ value on the corresponding night is given on the right.

compare our results. We can only state that $B_{\|} <$ 250 G (at the 3σ level) in the stellar photosphere at the time of our observations.

The value of $B_{\|}$ in the photosphere of T Tau averaged over the three nights was $+15 \pm 30$ G. In other words, in the winter of 2003, the longitudinal magnetic field component in the photosphere of T Tau did not exceed 90 G at the 3σ level, while in 1996 and 2002, it was equal to 160 ± 40 and 140 ± 50 G, respectively (Smirnov *et al.* 2003). According to Student's test, this means that the value of $B_{\|}$ in the winter of 2003 differed from the results of previous measurements with a probability of more than 90%. For this reason, we believe that we have detected variability of the longitudinal magnetic field component in the photosphere of T Tau.

We see from Table 2 that the longitudinal field in the magnetosphere of T Tau varied appreciably from night to night. In Fig. 3, we plotted $B_{\|}$ in the magnetosphere against rotation phase; for simplicity, this phase was counted off from the time of our first observation on January 16. By coincidence, our observations of January 18 and February 15 took place at virtually the same phase, but the values of $B_{\|}$ on these two nights differ by almost a factor of 3.

The cause of this difference is unclear. The correctness of our field measurement from a single line may be called into question. However, the similarity of the $B_{\|}$ values that we obtained on each night, along with the variation of the mean values from night to night, seems to be evidence that the variations of the measured field strength in the magnetosphere are real. In addition, we see from Fig. 4 that the helium line profiles on January 18 and February 15 were different, although they corresponded to the same
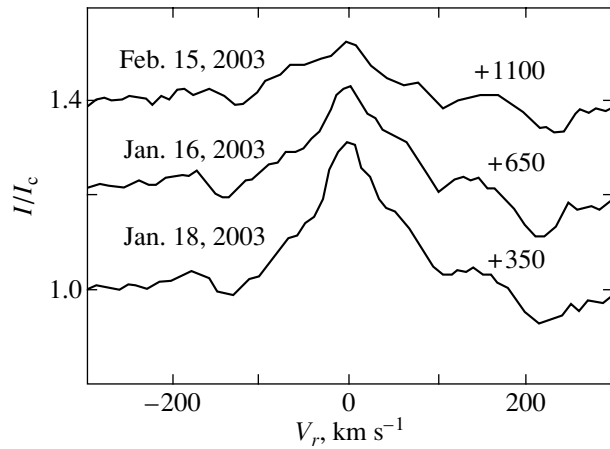
rotation phase; however, this is also typical of other CTTSs (see, e.g., Alencar and Batalha 2002). We can even see from Fig. 4 that there is a certain pattern in the variation of the line profile shape with $B_{\|}$: the larger the value of $B_{\|}$, the lower the intensity of its central peak.

Further observations are required to firmly establish whether the variations of $B_{\|}$ in the magnetosphere are real and to what extent they are associated with the changes in the profile shape of the He I 5876 Å line. In addition to the hypothesis that the magnetospheric field strength/structure is variable, the possibility that the rotation period of the magnetospheric region where the He I 5876 Å line is formed is not equal to the stellar rotation period and, hence, the longitudinal field component is different at the same axial rotation phases of T Tau, is worthy of note.

ACKNOWLEDGMENTS

REFERENCES

1. S. H. P. Alencar and C. Batalha, Astrophys. J. **571**, 378 (2002).
2. H. W. Babcock, Astrophys. J., Suppl. Ser. **3**, 207 (1958).
3. C. Bertout, Ann. Rev. Astron. Astrophys. **27**, 351 (1998).

4. P. F. Chugaĭnov, G. V. Zaĭtseva, and M. N. Lovkaya, Pis'ma Astron. Zh. **21**, 51 (1995) [Astron. Lett. **21**, 457 (1995)].

5. G. A. Chuntonov, Annu. Rep. Spec. Astrophys. Obs. **56**, 36 (1997).

6. E. Guenther, H. Lehmann, J. P. Emerson, and J. Staude, Astron. Astrophys. **341**, 768 (1999).

7. G. H. Herbig, Astrophys. J. **214**, 747 (1977).

8. G. H. Herbig and K. R. Bell, Lick Observ. Bull. 1111 (1988).

9. W. Herbst, J. F. Booth, P. F. Chugaĭnov, *et al.*, Astrophys. J. **310**, 71 (1986).

10. C. M. Johns-Krull, J. A. Valenti, A. P. Hatzes, and A. Kanaan, Astrophys. J. **510**, L41 (1999a).

11. C. M. Johns-Krull, J. A. Valenti, and C. Koresko, Astrophys. J. **516**, 900 (1999b).

12. C. M. Johns-Krull, J. Valenti, S. H. Saar, and A. P. Hatzes, ASP Conf. Ser. **223**, 521 (2001).

13. F. Kupka, N. Piskunov, and T. A. Ryabchikova, Astron. Astrophys., Suppl. Ser. **138**, 119 (1999).

14. V. E. Panchyuk, Preprint No. 154 (Spets. Astrofiz. Obs., 2001).

15. D. L. Padgett, Astrophys. J. **471**, 847 (1996).

16. D. A. Smirnov, S. N. Fabrika, S. A. Lamzin, and G. G. Valyavin, Astron. Astrophys. **401**, 1057 (2003).

17. R. J. White and A. M. Ghez, Astrophys. J. **556**, 265 (2001).

Translated by N. Samus'

Spatial Closeness of the White Hypergiants HD 168607 and HD 168625

E. L. Chentsov* and   E. S. Gorda

Special Astrophysical Observatory, Russian Academy of Sciences, Nizhniĭ Arkhyz,
357147 Karachai-Cherkessian Republic, Russia
Received November 12, 2003

Abstract—Our spectroscopic monitoring of the hypergiants HD 168607 (B9.5 Ia-0) and HD 168625 (B5.5 Ia-0) with resolutions from 15 000 to 70 000 confirms that both stars belong to the Ser OB1 association, proves their spatial closeness, and increases the probability that they constitute a physical pair. © 2004 MAIK "Nauka/Interperiodica".

Key words: *stars, stellar wind, radial velocities, HD 168607, HD 168625.*

INTRODUCTION

The paper by Pasquali *et al.* (2002) has inspired us to write this note. It gives the fourth version of the distance to HD 168625 in the last ten years, which "disengages" the pair of hypergiants HD 168607 and HD 168625.

White hypergiants, the most luminous late B— early A stars, and, in particular, the LBV variables among them, are very rare. Fewer than ten such objects in the Galaxy have been studied by means of high-resolution spectroscopy. They are scattered along the Milky Way from Carina to Cassiopeia more or less uniformly, but there is one striking exception, HD 168607 and HD 168625. These stars are located at the southern edge of the nebula M 17 and are spaced only 1 arcmin apart. Their basic parameters are given in Table 1.

But can this pair be considered physical? Or, to put it more mildly: Can we be sure that these stars belong to the same association (according to Humphreys (1978), to the Ser OB1 association)? The relevance of these questions is obvious: if the distances and motions of the two stars are identical, then, on the one hand, their luminosities and evolutionary statuses can be determined more reliably, and, on the other hand, it is easier to understand the kinematics of their atmospheres and winds. In particular, the radial velocities of the relatively quiet star HD 168625 could help in determining the center-of-mass velocity (V_{sys}) of the very unstable star HD 168607.

The minimum possible linear separation between HD 168607 and HD 168625, if their distance as Ser OB1 members is 2.2 kpc (Humphreys 1978), is

0.6 pc. Such wide visual binaries are not yet known (Halbwachs 1983). At the same time, one cannot help but take into account the low probability of such outstanding objects being neighbors by chance. It suggests a positive answer at least to the second of the above questions. However, even this question is answered negatively in most of the available publications.

To date, of the two stars, more attention has been given to HD 168625; not to the star itself, but to the surrounding gas—dust nebula. Published distance estimates for the nebula lie within the range 0.4 to 2.8 kpc. These are collected in Table 2. The evidence against a common origin and spatial closeness of HD 168607 and HD 168625 is contradictory and unconvincing. But is it now possible to provide convincing evidence for the physical nature of the pair without awaiting an improvement in the accuracy of astrometric measurements by an order of magnitude? We will try to find such evidence based on the radial velocities of HD 168607 and HD 168625 obtained during our spectroscopic monitoring of the two stars.

In the next section, we describe our spectroscopic data and their reduction. Subsequently, we present the data obtained and the conclusions drawn from them.

SPECTROSCOPIC DATA AND ITS REDUCTION

Since the objects are spectroscopically variable to such an extent that they were classified as S Dor variables (van Genderen 2001), their monitoring should have been long enough, especially for the more active star HD 168607. Since, further, important information can be extracted from the profiles of not only stellar lines but also interstellar lines and narrow diffuse

---

*E-mail: `echen@sao.ru`

Table 1. Basic parameters of the stars

Star	α_{2000}	δ_{2000}	V	Sp	$(B-V)_0$	$(B-V)$	$E(B-V)$
HD 168607	$18^h21^m12^s$	$-16°22'01''$	8.16	B9.5 Ia-0	0.01	1.44	1.43
HD 168625	18 21 16	-16 21 52	8.39	B5.5 Ia-0	-0.08	1.33	1.41

Note: V and $(B-V)$ are the mean values from van Genderen *et al.* (1992), $(B-V)_0$ is from FitzGerald (1970), Sp is from our estimates.

Table 2. Distance estimates for HD 168625

d, kpc	Estimation method	Reference
0.4	Trigonometric parallax	Garcia-Lario *et al.* (2001)
1.2	Photometric parallax	Robberto and Herbst (1998)
>2.2	Kinematic, from V_{sys} of nebula	Hutsemekers *et al.* (1994)
2.8	Kinematic, from V_{sys} of star	Pasquali *et al.* (2002)

interstellar bands (DIBs), it was necessary to perform at least some of the observations with a sufficiently high spectral resolution.

We used 13 spectra of HD 168607 obtained from 1992 until 2002 and 6 spectra of HD 168625 obtained from 1997 until 2002 with several echelle spectrometers equipped with CCD arrays. Although the reduction results for the spectra that we obtained previously on photographic plates (Chentsov and Luud 1989) are consistent with the new results, they are less accurate and are not used here. The first three columns of Table 3 contain the date when the spectrum was obtained, the spectrometer used, and the working spectral range. The notes to the table give brief information about the spectrometers: the telescope, the focus, the spectral resolution, and the reference to a paper with a detailed description.

After the extraction of one-dimensional fragments corresponding to individual orders from the two-dimensional images of the spectra, we performed the subsequent reduction (continuum placement, construction of the dispersion curves, positional and photometric measurements) using the DECH 20 code (Galazutdinov 1992). In particular, the positions of the needed features in lines were measured by matching the direct and mirror images of their profiles. The correction for instrumental shifts, which are especially relevant in comparing the radial velocities obtained with different instruments during a long period, were made using telluric O_2 and H_2O

lines. The residual systematic errors did not exceed 2 km s^{-1} for the PFES spectrometer and 1 km s^{-1} for the remaining spectrometers.

RADIAL VELOCITIES FROM STELLAR AND INTERSTELLAR LINES

The radial velocities discussed below are heliocentric. They were measured from the absorption cores and the emission peaks. The residual intensities of the weakest single lines whose velocities could still be determined with acceptable errors (2–3 km s^{-1}) are $r = 0.98$ and 1.02, respectively.

Since the radial velocities of the stars' centers of mass, V_{sys}, are required to resolve the question of interest, we could not restrict ourselves to measuring individual lines, as was done in some of the cited papers, but had to compare the velocities derived from a large set of absorptions and emissions. V_{sys} cannot be directed measured for our objects. Apart from being spectroscopically variable, the various lines in the spectra of both stars always exhibit differential shifts, because their formation regions extend from the pulsating photospheres to the nonstationary winds. The specific features of the spectra are presented in more detail in the atlas by Chentsov *et al.* (2003); here, we note only their main features.

The first Balmer lines in the spectra of both stars originate in the stellar wind. The absorption components of their P Cyg profiles are generally

Table 3. Data on the spectra and heliocentric radial velocities

Date	Spectro-meter	$\Delta\lambda$, nm	V_r, km s^{-1}				
			P Cyg	$V_r(r \to 1)$	V_{em} Fe II	Na I	DIB
HD 168607							
Aug. 14, 1992	L	458−595	−95	16	12:	1	7:
May 28, 1994	L	515−710	−130	7	10:	2	6:
June 18, 1995	C1	480−670	−120	10	10	−	8
Aug. 10, 1995	L	480−675	−130	9	10	1	8
July 4, 1996	P	515−790	−120	9	8	1	8
July 21, 1997	L	540−670	−105	12	9:	3	8:
June 19, 1998	P	410−770	−140	16	10	1	8
July 8, 1998	P	445−770	−145	9	9	1	8
Aug. 14, 1998	C2	430−980	−110	10	8	−7.5	8
June 24, 2000	L	470−633	−100	11	10:	1	8
June 4, 2001	P	455−790	−105	10	7:	0	8
July 29, 2002	N	458−595	−120	17	11:	−7.6	7:
Sep. 27, 2002	MD	545−670	−130	9	9	−7.5	8
			Mean	11.5 ± 0.8	9.2 ± 0.4	−	7.8 ± 0.2
HD 168625							
July 23, 1997	L	540−670	−90:	12	−	1	8:
June 19, 9198	P	410−770	−165	12	10:	1	8
June 4, 1999	L	516−670	−150	16	−	−7.6	9
June 24, 2000	L	470−633	−50	11	−	1	8
July 29, 2002	N	458−595	−16	9	−	−7.6	8
Sep. 27, 2002	MD	545−670	−45	8	8:	−8.7	7
			Mean	$11. \pm 1.0$	9:	−	8.0 ± -0.2

Note: P—PFES spectrometer at the prime focus of the 6-m Special Astrophysical Observatory (SAO) telescope, spectral resolution 15 000 (Panchuk *et al.* 1998); L—LINX spectrometer at the Nasmyth focus of the 6-m SAO telescope, spectral resolution 25 000 (Panchuk *et al.* 1999); C1—spectrometer at the Coude focus of the 1-m SAO telescope, spectral resolution 40 000 (Musaev 1996); C2—Coude spectrometer of the 2-m Terskol Observatory telescope, spectral resolution 40 000 (Musaev *et al.* 1999); MD—spectrometer at the Cassegrain focus of the 2.1-m McDonald Observatory telescope, spectral resolution 64 000 (McCarthy *et al.* 1993); N—NES spectrometer at the Nasmyth focus of the 6-m SAO telescope, spectral resolution 70 000 (Panchuk *et al.* 2002).
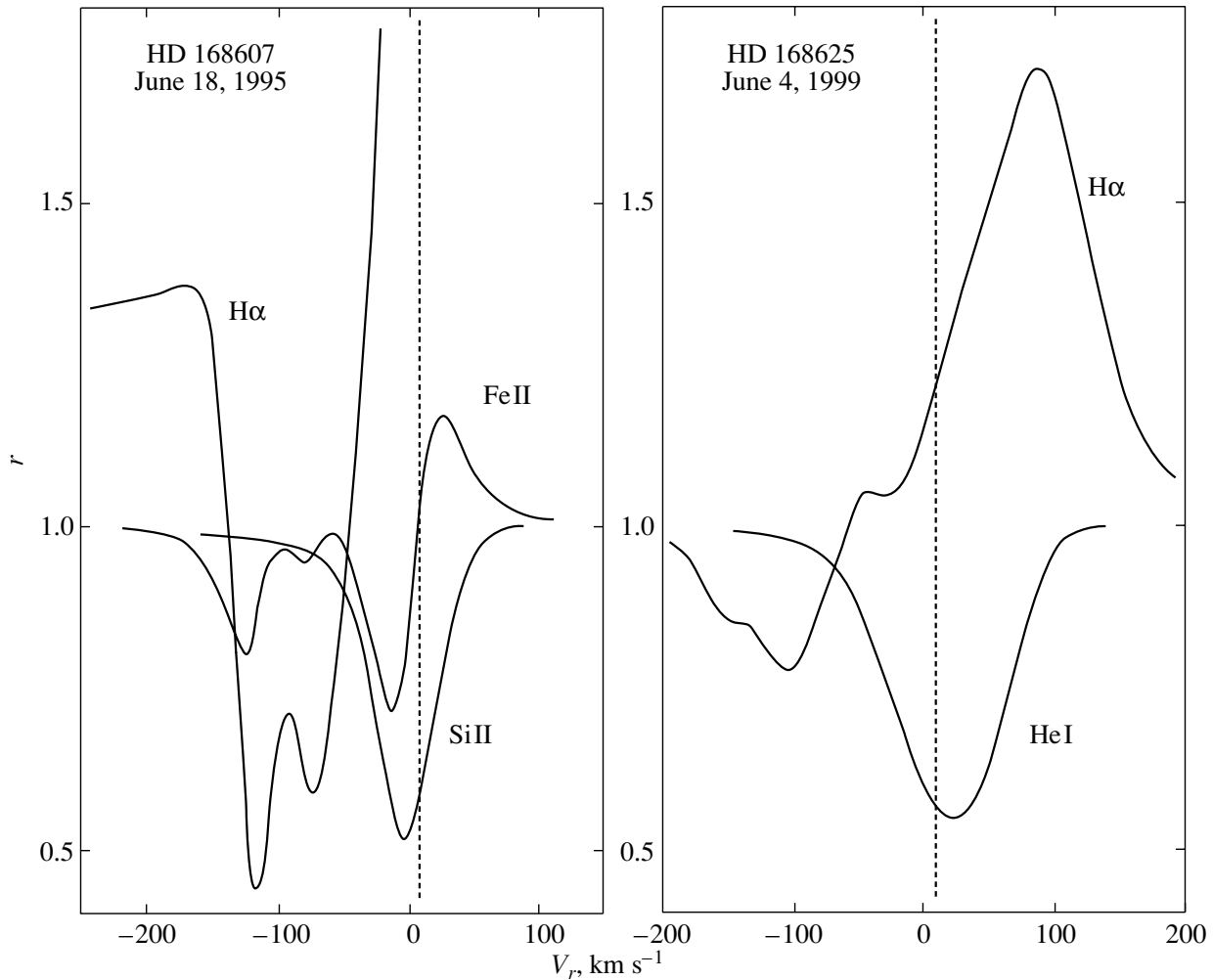
Fig. 1. Profiles of the Hα, Fe II(42) 5169 Å, and Si II(2) 6347 Å lines in the spectrum of HD 168607 taken on June 18, 1995, and of the Hα and He I(11) 5876 Å lines in the spectrum of HD 168625 taken on June 4, 1999. The vertical dashed lines mark the center-of-mass velocities of the stars.

split into several components. The Hα profiles shown in Fig. 1 together with the profiles of some other lines have three components each. In the spectrum of HD 168607, the shapes and parameters of the absorption components of the Balmer lines are copied (more conspicuously) by Fe II lines. The figure shows the Fe II(42) 5169 Å line as an example. Its low-velocity component, which gives $V_r = -14$ km s^{-1}, is deeper than the two remaining components, while in the Hα profile, it is lost on the steep blue slope of the emission. Such profiles exhibiting comparatively low expansion velocities are characteristic of the slow dense winds from hypergigants. The radial velocities pertaining to the most blueshifted absorption components, V_r (P Cyg), are given in the fourth column of Table 3.

Let us now consider the photospheric absorptions of He I, C II, N II, and some heavier ions. One might expect the velocities derived from the weakest lines formed deeper than other lines to be closest to the velocity of the star as a whole. They show no clear asymmetry in the profiles. An asymmetry appears in stronger absorptions: absorption at the base of the wind deepens and stretches their blue wings. This can be seen from Fig. 1 in the profiles of the Si II(2) 6347 Å and He I(11) 5876 Å lines, the deepest absorptions in the spectra of HD 168607 and HD 168625, respectively. In Fig. 2, V_r measured from individual lines or their components are plotted against their residual intensities r. We see a shift in the stronger lines with respect to the weakest ones, which increases with line depth. To approach V_{sys} as closely as possible, we extrapolated $V_r(r)$ to the

continuum level ($r \rightarrow 1$). The values of V_r ($r \rightarrow 1$) obtained in this way are given in the fifth column of Table 3. For HD 168625, a velocity close to the tabulated values (10 ± 2 km s^{-1}) can be derived from that given by Pasquali *et al.* (2002, Fig. 9) by referencing the C II(2) doublet to neighboring telluric lines. The time variations of V_r ($r \rightarrow 1$) are real, but, according to our data, their amplitudes do not exceed 10 km s^{-1}, and the mean values for both stars are the same within the error limits: 11.5 km s^{-1}.

The stationary symmetric Fe II emissions in the red and near infrared spectral ranges (6318, 7513 Å etc.) are more valuable for estimating V_{sys}. They are probably emitted by the extended envelopes of the stars (i.e., the envelopes that are several orders of magnitude smaller than the circumstellar nebula of HD 168625 and that are invisible in direct images). These emissions are barely noticeable in the spectrum of HD 168625; only 2 or 3 of them are measurable, they are much stronger in the spectrum of HD 168607, and, in the best cases, the velocities were obtained for 8−10 lines. The part of the spectrum for HD 168607 containing the Fe II 6318, 6384, and 6385 Å lines is compared with the same part of the spectrum for HD 168625 where they are invisible in Fig. 3. The velocities derived from pure Fe II emissions are indicated by the dashed straight line at $r = 1.0$ in Fig. 2a. These velocities averaged for each spectrum (V_{em}) are given in the sixth column of Table 3. In contrast to V_r ($r \rightarrow 1$), the small variations of V_{em} from date to date are caused only by the measurement errors. The value averaged over the entire data for HD 168607 (9.2 ± 0.4 km s^{-1}) is equal to that for HD 168625 (9:). However, it should be emphasized that it was established much more reliably for the former star than for the latter one. The reason lies not only in the different numbers of measurements; for HD 168607, the numerous Fe II lines with P Cyg profiles mentioned above provide additional information. The velocities measured from the peaks of their emission components (the open circles in Fig. 2a) are uniquely related to the intensities of the absorption components: the weaker they are, the lower the velocities. As we see from Fig. 2a, the lowest V_r values approach V_{em} and improve them.

Thus, it follows from the set of velocity data obtained from absorption and emission lines that the same center-of-mass velocity may be taken for both stars. Based on the emissions alone, we should take $V_{sys} = 9$ km s^{-1}. It is important to note that this value is equal to the mean radial velocity of the nebula M 17 estimated by Clayton *et al.* (1985). However, since the velocities measured from emissions for HD 168625 are still uncertain, we are inclined to a more cautious estimate: $V_{sys} = 10 \pm 1$ km s^{-1}. This
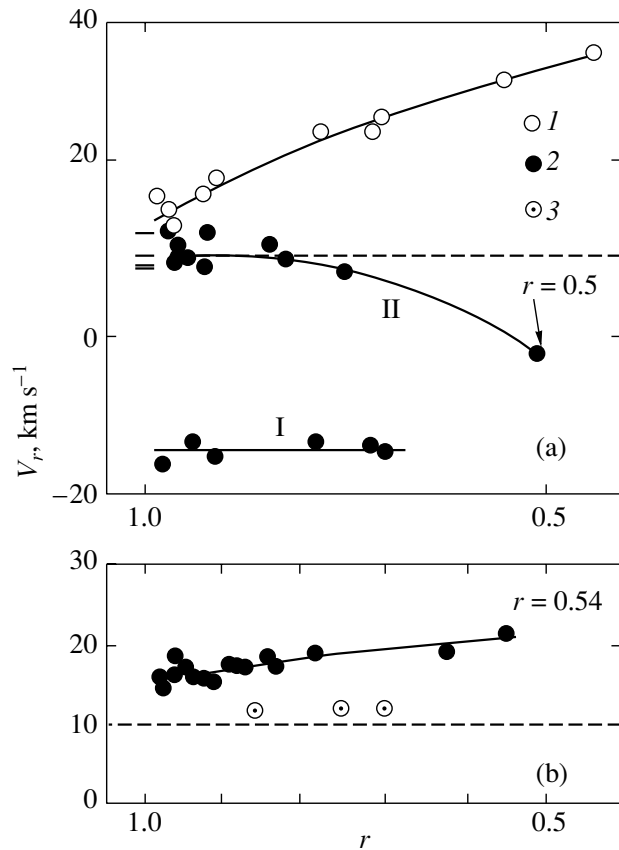

Fig. 2. Heliocentric radial velocities versus residual intensities of the absorptions or absorption components in P Cyg profiles. Each symbol corresponds to an individual line. (a) HD 168607 on June 18, 1995. (*1*) Emission components of P Cyg profiles; (*2*) (curve I) red absorption components of P Cyg profiles (no dependences for the blue components with velocities of −75 and −120 km s^{-1} are shown); (*2*) (curve II) He I, C II, and other absorptions; the symbol at $r = 0.5$ is the Si II 6347 line whose profile is shown in Fig. 1. The dashed straight line at $r = 1.0$ corresponds to the stationary Fe II emissions. (b) HD 168625 on June 4, 1999. *2*: He I, C II, and other absorptions; the symbol at $r = 0.54$ is the He I 5876 line whose profile is shown in Fig. 1. *3*: Fe II(42) and Si II(2) absorptions; the dashed straight line marks the center-of-mass velocities of the stars.

value is marked by the dashed straight lines in Figs. 1 and 2.

The interstellar lines and bands are very strong in the spectra of the stars under consideration; what is especially important, they are almost equally strong in both stars. This is demonstrated by Figs. 4 and 5. At a high resolution and after the removal of the contribution from the telluric H$_2$O spectrum, the Na I (1) lines split into several components. The only difference between the profiles for the two stars that is noticeable in Fig. 4 is a weak dip at $V_r \approx 35$ km s^{-1} for HD 168625.
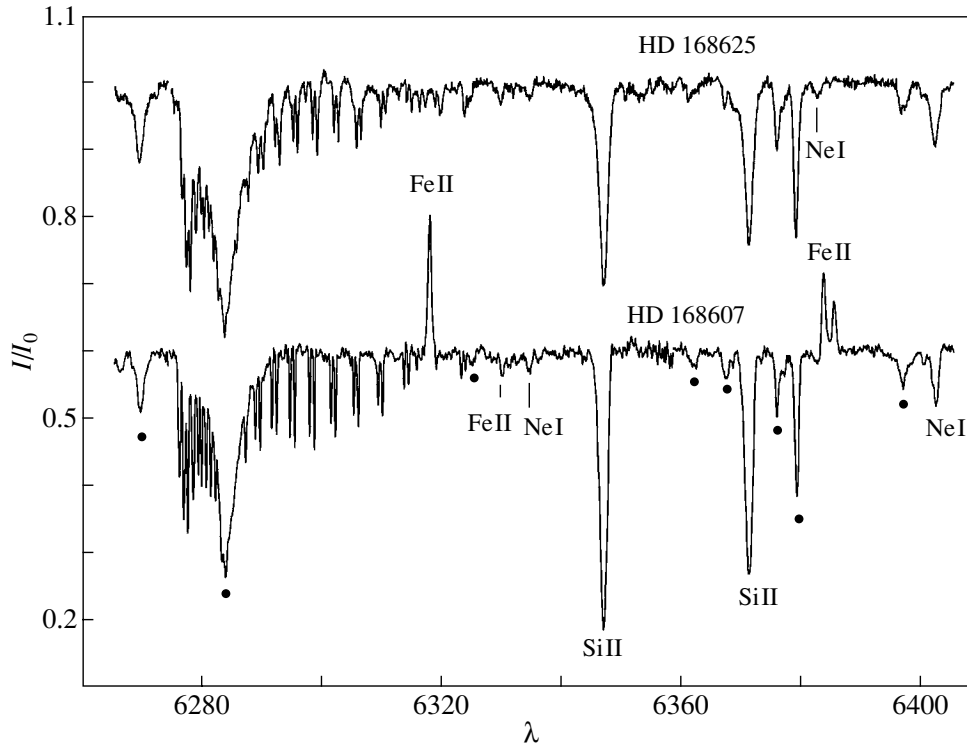
Fig. 3. Comparison of the spectra for HD 168607 and HD 168625 near the stationary Fe II 6318, 6384, and 6385 Å emissions. Identifications of stellar lines are given; the dots mark DIBs. The unmarked narrow absorptions are the telluric O_2 lines.

Since the radial velocity toward our objects ($l = 15°$) increases with distance (Brand and Blitz 1993), this could suggest that the star is at a large distance if its own velocity were not considerably lower. For the remaining components, both the positions and the depths are identical. The two deepest components, which indicate the presence of two main gas clumps on the line of sight, are spaced 14 km s^{-1} apart. The redshifted component ($V_r \approx 6$ km s^{-1}) formed farther on the line of sight than the blueshifted component ($V_r \approx -7$ km s^{-1}) is deeper. This is more clearly seen not in the saturated Na I lines, but in the weaker K I line (unfortunately, we have its well-traced profile only for HD 168607, Fig. 3) and in narrow DIBs.

The narrow DIBs have recently been shown to have their own fine structure (Galazutdinov *et al.* 2002). Besides, in our case, they are split by Galactic rotation, just as the Na I and K I lines. The combined action of both effects can be seen in Fig. 5 for the DIB 6614 Å consisting of three main components and several weaker ones. The profiles in the spectra of the two stars copy themselves in every detail, which would be unlikely to be the case if their distances and the column densities differed significantly. The latter is also true for the interstellar dust. As we see from Table 1, the difference between

the color indices of the stars is offset by the difference between their intrinsic colors.

The seventh column of Table 3 contains the V_r values for NaI (1). When the resolution permitted, the velocities were measured for the two main components; in the remaining cases, they were measured for the lines as a whole. The last column gives the V_r values measured from the cores of the narrowest DIBs: 5797, 6196 Å and others. Their effective wavelengths were taken from the atlas by Galazutdinov *et al.* (2000). The positions of interstellar lines and bands can be determined more accurately than those of weak stellar lines, but our measurements using these lines revealed no differences between the mean velocities for the two stars either.

The small systematic discrepancy between the V_r values for DIBs and the redshifted components of the Na I lines could be due to uncertainties in the laboratory wavelengths for the former and to the blending of the latter with neighboring blueshifted components (the DIBs and the K I lines have equal velocities). It is natural that V_r for interstellar lines and DIBs is slightly lower than V_{em} and, hence, lower than V_{sys}: the effective distance even to the far interstellar clouds is smaller than the distance to our pair of stars.
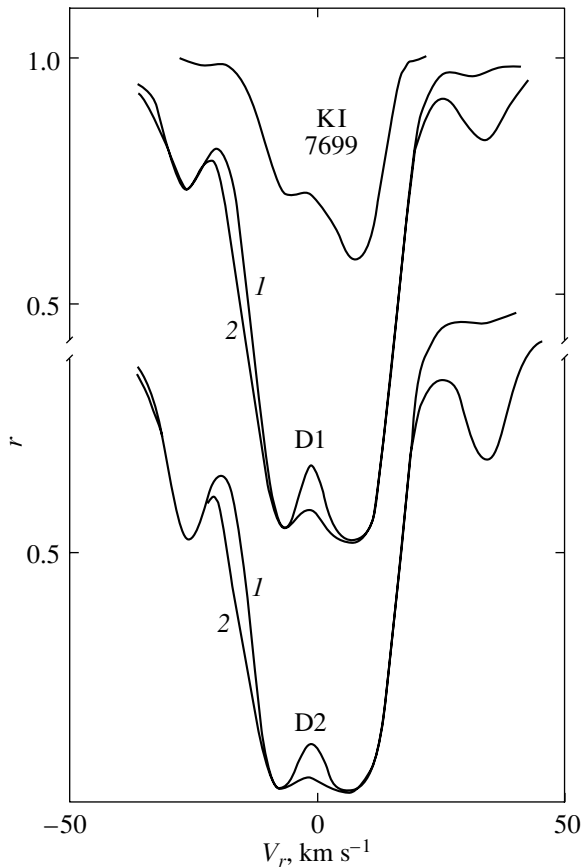
Fig. 4. Interstellar line profiles. From top to bottom: K I(1) 7699 Å in the spectrum of HD 168607 with a resolution of 40 000, Na I(1) 5896 and 5889 Å in the spectra of HD 168607 (curves *1*) and HD 168625 (curves *2*) with a resolution of 70 000. The telluric lines were eliminated.
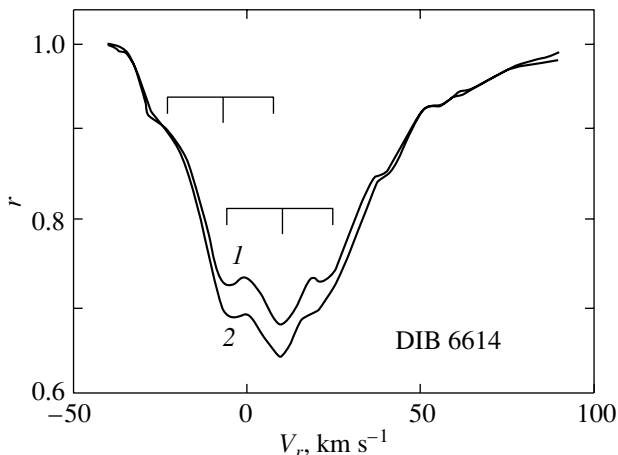

Fig. 5. Profiles of the DIB 6614 Å with a resolution of 64 000 in the spectra of HD 168607 (*1*) and HD 168625 (*2*). The vertical bars indicate the DIB components and their Doppler shifts.

CONCLUSIONS

The attempts to "disengage" the pair of HD 168607 and HD 168625 have found no spectroscopic support. At least four observational facts prevent the assumption that they are neighbors in the sky by chance:

(1) clear spectroscopic signatures of extremely high luminosity for both stars,

(2) identical interstellar reddening,

(3) equal center-of-mass radial velocities of the stars,

(4) coincident profiles of interstellar lines and DIBs and equal radial velocities derived from them.

The first two arguments are generally the weakest. They can be circumvented by assuming that the reddening of the nearer star is partly of a circumstellar origin and that it belongs to low-mass stars with spectra similar to those of hypergiants. HD 168625 is a better candidate for this role: it has an IR excess and is surrounded by a nebula, while both features are absent for HD 168607. However, this assumption is in conflict with the third and fourth facts. The significant distance difference would inevitably manifest itself in a difference between the radial velocities of the stars and between the profiles of interstellar lines and bands. Of course, a physical pair can be "destroyed" even by the small distance difference admitted by the natural luminosity range of hypergiants, but this does not cancel out the main fact: both stars belong to the same group, i.e., they have a common origin, similar ages, etc.

Thus, our new spectroscopic data strongly suggest that HD 168607 and HD 168625 are spatially close to each other and belong to the Ser OB1 association. They also provide evidence for the highly likely connection of these hypergigants with the M 17 complex. While these data do not ultimately prove that HD 168607 and HD 168625 constitute a physical pair, they in any case significantly increase the probability of their physical association. The prospects for a further improvement in observing facilities are primarily related to obtaining high-resolution spectra for neighboring stars (in particular, for stars of the M 17 complex) and milliarcsecond-resolution images of the objects.

program, and the basic research program Extended Objects in the Universe of the Department of Physical Sciences of the Russian Academy of Sciences (the Spectroscopy of Extended Envelopes around Evolved Stars subprogram).

REFERENCES

1. J. Brand and L. Blitz, Astron. Astrophys. **275**, 67 (1993).
2. E. L. Chentsov and L. S. Luud, Astrofizika **31**, 5 (1989).
3. E. L. Chentsov, S. V. Ermakov, V. G. Klochkova, *et al.*, Astron. Astrophys. **397**, 1035 (2003).
4. C. F. Clayton, V. N. Ivchenko, J. Meaburn, and J. R. Walsh, Mon. Not. R. Astron. Soc. **216**, 761 (1985).
5. M. P. FitzGerald, Astron. Astrophys. **4**, 234 (1970).
6. G. A. Galazutdinov, Preprint No. 92 (Spets. Astrofiz. Obs. Ross. Akad. Nauk, 1992).
7. G. A. Galazutdinov, F. A. Musaev, J. Krelowski, and G. A. H. Walker, Publ. Astron. Soc. Pac. **112**, 648 (2000).
8. G. A. Galazutdinov, W. Stachowska, F. Musaev, *et al.*, Astron. Astrophys. **396**, 987 (2002).
9. P. Garcia-Lario, T. Sivarani, M. Parthasarathy, and A. Manchado, *Post-AGB Objects As a Phase of Stellar Evolution,* Ed. by R. Szczerba and S. K. Gorny (Kluwer Acad. Publ., Dordrecht, 2001), p. 309.
10. A. M. van Genderen, Astron. Astrophys. **366**, 508 (2001).
11. A. M. van Genderen, F. C. van den Bosh, F. Dessing, *et al.*, Astron. Astrophys. **264**, 88 (1992).
12. J. L. Halbwachs, Astron. Astrophys. **128**, 399 (1983).
13. R. M. Humphreys, Astrophys. J., Suppl. Ser. **38**, 309 (1978).
14. D. Hutsemekers, E. van Drom, E. Gosset, and J. Melnik, Astron. Astrophys. **290**, 906 (1994).
15. J. K. McCarthy, A. Brendan, A. Sandiford, *et al.*, Publ. Astron. Soc. Pac. **105**, 881 (1993).
16. F. A. Musaev, Pis'ma Astron. Zh. **22**, 795 (1996) [Astron. Lett. **22**, 715 (1996)].
17. F. A. Musaev, G. A. Galazutdinov, A. V. Sergeev, *et al.,* Kinemat. Fiz. Neb. Tel **15**, 3 (1999).
18. V. E. Panchuk, I. D. Najdenov, V. G. Klochkova, *et al.*, Bull. Spec. Astrophys. Observ. **44**, 127 (1998).
19. V. E. Panchuk, V. G. Klochkova, I. D. Naidenov, *et al.,* Preprint No. 139 (Spets. Astrofiz. Obs., 1999).
20. V. E. Panchuk, N. E. Piskunov, V. G. Klochkova, *et al.,* Preprint No. 169 (Spets. Astrofiz. Obs., 2002).
21. A. Pasquali, A. Nota, L. J. Smith, *et al.*, Astron. J. **124**, 1625 (2002).
22. M. Robberto and T. M. Herbst, Astrophys. J. **498**, 400 (1998).

Translated by N. Samus'

Proper Motions of 59 766 Stars Absolutized Using Galaxies in 149 Sky Fields (PUL2)

V. V. Bobylev*, N. M. Bronnikova, and N. A. Shakht

Pulkovo Astronomical Observatory, Russian Academy of Sciences, Pulkovskoe shosse 65, St. Petersburg, 196140 Russia

Received July 16, 2003

Abstract—The PUL2 catalog has been photographically compiled in Pulkovo according to Deutch's plan. The catalog contains the mean coordinates of stars in the ICRS system at epoch J2000.0 and their original absolute proper motions. The photographic observations were performed with a normal astrograph. The first and second epochs of the photographic plates are 1937−1965 and 1969−1986, respectively. The PUL2 fields uniformly cover the northern sky. The mean difference between the epochs is 24 years. At least three pairs of plates are available for each field. There are one-hour and five-minute exposures on all plates. One pair of plates was taken with a diffraction grating. Only bright reference stars were measured on the pairs of plates with a grating. Based on a reduction model with six constants and using faint (15^m2) reference stars, we determined the relative proper motions of the stars. We used ∼700 galaxies for absolutization. The mean errors in the relative proper motions of the PUL2 stars are 5.5 mas yr^{-1} (milliarcseconds per year) in $\mu_\alpha \cos\delta$ and 5.9 mas yr^{-1} in μ_δ. When using galaxies, the mean absolutization error is 7.9 mas yr^{-1} in both coordinates. By comparing the PUL2 and HIPPARCOS catalogs, we determined the components of the residual rotation vector $\boldsymbol{\omega}$ for HIPPARCOS relative to the extragalactic (equatorial) coordinate system: $\omega_{x,y,z} = (-0.98, -0.03, -1.66) \pm (0.47, 0.38, 0.42)$ mas yr^{-1}. The mean error of one absolute proper motion of a bright PUL2 star in external convergence is 9 mas yr^{-1} in both coordinates. © 2004 MAIK "Nauka/Interperiodica".

Key words: *star clusters and associations, stellar dynamics, astrometry, catalogs, ICRS system, absolute proper motions.*

INTRODUCTION

At the first Astrometric Conference, Gerasimovich and Dneprovskiĭ (1933) put forward the idea of compiling a fundamental catalog of faint stars (CFS) using extragalactic nebulae to determine the absolute proper motions of stars. This approach yields an independent approximation to the inertial coordinate frame. Since the absolute proper motions of stars obtained in this way are free from the precession effect of the Earth's axis, they can serve as a basis for checking the determination of the precession constant and for studying the kinematics of various groups of stars in the Galaxy. At that time, the absolute proper motions of a large number of stars could be determined only by means of photographic astrometry. To perform the formulated task, Neuĭmin (1940) compiled the first list of galaxies. It contains a description of 271 galaxies located in 143 fields. Systematic observations of areas with galaxies were begun in 1939 at three observatories:

in Pulkovo, Moscow, and Tashkent. At the 8th General Assembly of the IAU, Deutch (1954) proposed using telescopes like a normal astrograph in both hemispheres to take photographs of selected fields with galaxies to determine the absolute proper motions of stars ("Deutch's plan"). Thanks to the efforts of Deutch, many observatories worldwide took part in the program of determining the absolute proper motions of stars using galaxies as reference objects. The Pulkovo zone covers the declination range −5° to +90° and includes 157 fields. For these fields, Deutch *et al.* (1955) compiled a catalog of 1508 galaxies. Each galaxy was described in terms of its appearance, shape, brightness, size, and suitability for measurements.

The first Pulkovo catalog of absolute proper motions for 14 600 stars to the 15th photographic magnitude in 85 fields of the Pulkovo zone was published by Fatchikhin (1974); we denote this catalog by PUL1. Plates taken during the period 1937−1941 served as the first epochs in PUL1. Photographs of the second epochs were taken during the period 1959−1967 using glass. The combined GPM (Ry-

bka and Yatsenko 1997b) and GPM1 (Rybka and Yatsenko 1997a) catalogs were compiled by combining 20 catalogs of the CFS program, which also included PUL1. The PUL2 catalog was compiled from original observational material. About 20 plates of the first epochs are common to PUL2 and PUL1. A technique different from that of the PUL1 catalog was used to measure all PUL2 plates. The PUL2 photographic observational material for the second epochs does not overlap with the PUL1 material.

The PUL2 catalog shares about 1200 common stars with the HIPPARCOS catalog (ESA 1997), which is of current interest in checking the referencing of HIPPARCOS to the extragalactic coordinate system. The inertiality estimate for the proper motions of HIPPARCOS stars that was first obtained by Kovalevsky *et al.* (1997) is only tentative. The problem is that the photographically determined absolute proper motions of stars, for example, the proper motions of stars in the Kyiv CFS (Rybka and Yatsenko 1997b), NPM1 (Clemola *at al.* 1994), and SPM (Platais *et al.* 1995) catalogs have a fairly strong magnitude dependence with a coefficient of ~ 1 mas yr^{-1} per magnitude. The magnitude equation of such an order for the NPM and SPM programs, in which 16^m stars serve as reference ones, leads to a shift in the proper motions of bright ($8-10^m$) stars by $\approx 8-6$ mas yr^{-1}. Significant differences in determining the components of the vector $\boldsymbol{\omega}$ as a function of the magnitude were found for the Kyiv CFS program (Kislyuk *et al.* 1997). The NPM1 catalog revealed a magnitude equation that has a major effect on the ω_z determination (Kovalevsky *et al.* 1997). Because of the magnitude equation, Kovalevsky *et al.* (1997) did not use any of the solutions of the NPM program, which shares the largest number of common stars with the HIPPARCOS catalog, to derive the final solution when determining the ω_z component. Platais *et al.* (1995) found a noticeable magnitude equation in the positions and proper motions of SPM stars, but it was eliminated by comparing the positions of SPM and HIPPARCOS stars. This method for eliminating the magnitude equation fundamentally reduces the originality of the results of the comparison of the SPM and HIPPARCOS programs. In fact, the ω_z estimate by Kovalevsky *et al.* (1997) is based solely on the results of the comparison of SPM and HIPPARCOS stars.

Here, based on the most complete list of common stars shared by PUL2 and HIPPARCOS and by PUL2 and TRC (Kuzmin *et al.* 1999; Hog *et al.* 1998), we redetermined the components of $\boldsymbol{\omega}$—the vector of residual rotation of the ICRS system with respect to the extragalactic coordinate system.

OBSERVATIONS

The catalog of absolute proper motions of stars was compiled in Pulkovo photographically using galaxies as reference objects. The observations were performed with a normal astrograph ($F = 3.5$ m, $D = 0.33$ m, $2° \times 2°$ field). Plates of the first and second epochs were taken during the periods $1937-1965$ and $1969-1986$, respectively. The mean difference between the epochs is 24 years. There are at least three pairs of plates for each area, of which one was taken with a diffraction grating. On the plates taken with a grating, the first-order diffraction satellites were attenuated by 4^m2 with respect to the central stellar image. All pairs of plates have one-hour and five-minute exposures.

Observational material was obtained for 157 areas in accordance with the list by Deutch *et al.* (1955). The fields with numbers 4, 13, 45, 59, 81, 135, and 143 were excluded after examining all plates of the first epochs, because no measurable images of galaxies were obtained in these fields.

Plates of the second epochs were taken in such a way that the difference between the epochs was no less than 20 years and that the hour angles on the plates of the two epochs were equal.

The observing conditions in Pulkovo deteriorated significantly in the early 1980s: the illumination of the sky increased first, through the expansion and city lights of Leningrad, and, second, because of the greenhouses illuminated at night that were constructed 2 to 3 km south of Pulkovo. The plates with a one-hour exposure had a large veil. The plates of the second epochs for fields with negative declinations were particularly difficult to take. For example, 14 and 12 plates were taken for fields nos. 31 ($\delta = -4°56'$) and 29 ($\delta = -5°00'$), respectively. For 88 and 32 areas, three measurable plates of the second epochs were chosen from $4-6$ and $7-10$ available plates, respectively.

Agfa-Astro emulsions were mainly used when taking photographs of the first epochs; photographs of the second epochs were taken on ORWO Zu-1, ORWO Zu-2, and Kodak 103aO plates.

Much of the available observational material was obtained by N.V. Fatchikhin: 37% at the first epoch and 16% at the second epoch. At the first epoch, V.V. Lavdovskiĭ and F.F. Bulatova-Kalikhevich obtained 30% and 15% of the material, respectively. For the second epochs, N.M. Bronnikova, O.N. Orlova, and L.S. Koroleva took 30, 21, and 12% of the plates. The remaining observers took less than 20% of the plates at both the first and second epochs.

MEASUREMENTS

Plate measurements were begun in Pulkovo in 1971. The following persons took part in the measurements: A.N. Deutch (1971−1979), V.V. Lavdovskiĭ (1971−1978), O.N. Orlova (1971−1984), N.V. Fatchikhin (1971−1984), I.I. Kumkova (1976−1977), S.S. Smirnov (1977−1978), N.A. Shakht (1975−1987), N.M. Bronnikova (1980−1988), V.V. Bobylev (1982−1988), and S.A. Lepeshenkova (1985−1988). The largest number of plates were measured by O.N. Orlova (23%), N.A. Shakht (21%), N.M. Bronnikova (14%), and N.V. Fatchikhin (13%).

The measuring technique included the following steps:

(1) Before the measurements, each pair of plates was examined with a blink comparator to find stars with large proper motions, $|\mu| > 0.05''$ yr^{-1}, in the entire plate field.

(2) All of the stars within a circle of radius $20'$ at Galactic latitudes $|b| < 40°$ and within a circle of radius $30'$ at Galactic latitudes $|b| > 40°$ were measured on each pair of plates. Reference stars were measured within a circle $10'$ larger in radius, i.e., $30'$ and $40'$, respectively. For this purpose, two circles of the corresponding radius were drawn on one of the plates of the best quality on the glass side and then 60 uniformly distributed points were plotted inside the circle of reference stars. Since reference stars in the measurements were chosen near these points, the distribution of reference stars was uniform in the plate field.

(3) The plates were oriented for epoch 1950.0 in the measuring device using a preselected pair of stars. The orientation accuracy was ±0.1 mm. This procedure was necessary because the proper motions of the stars were determined from the differences between the measured stellar coordinates.

(4) Two systems of reference stars were chosen in the measurements: bright and faint reference stars with photographic magnitudes 13^m5−13^m8 and 15^m0−15^m7.

(5) Four sharp markers chosen in the plate corners were measured to check the stability of the plate in the measuring device. Appropriate corrections for the displacement of these markers, which generally did not exceed 3−4 μm, were applied to the measurements. The markers were measured every day at the beginning and at the end of the measurements.

(6) Bright check stars common to the AGK3 catalog (Diekvoss *et al.* 1975) and, subsequently, to the PPM catalog (Rëser and Bastian 1991) were chosen beforehand. The following order of measurements was always used: (a) measurements of the check markers at four positions of the reversal prism; (b)

measurements of galaxies at four positions of the reversal prism; (c) measurements of check stars: one-hour and five-minute images; (d) measurements of all the stars within the $20'$−$30'$ circle; (e) measurements of reference stars outside the $20'$−$30'$ circle; (f) both the one-hour and five-minute images were measured for bright reference stars; (g) after measuring half of the plate field, the second measurement of galaxies was made; (h) finally the check stars were remeasured, and stars with large proper motions and galaxies were measured.

All plates were measured using an Ascorecord device. The measurements were finished in 1988. The random measurement errors for galaxies are a factor of 1.5−2 larger than the measurements errors for PUL2 reference stars (Bronnikova and Shakht 1987).

MAGNITUDES

The photographic magnitudes of the PUL2 stars were determined by measuring the plates of the normal astrograph that were taken with a diffraction grating. The diffraction grating placed in front of the objective of the telescope yielded well-measurable first-order diffraction satellites attenuated by 4^m2 with respect to the central stellar image. The photographic magnitudes of AGK3 stars determined with an accuracy of ±0^m2 were used as standards. When there were check stars within the plate field with magnitudes from 8^m to 12^m5, the diffraction satellites had magnitudes from 12^m2 to 16^m7. These were bright enough to construct the characteristic curve for stars with magnitudes from 8^m to 16^m7 and to determine the magnitudes for all of the measured stars. The plates intended to determine the magnitudes were measured during the period 1986−1998 with the Ascoris semiautomatic iris photometer. The measurers were the following: N.M. Bronnikova (105 fields), N.A. Shakht (32 fields), V.V. Bobylev (10 fields), and Z.N. Ipatova (Kazan' University, 3 fields).

The accuracy of the magnitude measurements in the PUL2 catalog was analyzed by Bronnikova *et al.* (1996). The internal error in the PUL2 photographic magnitudes is ±0^m02−0^m08. The external error in the PUL2 photographic magnitudes for the bulk of the measured faint stars is ±0^m3.

Stars brighter than 8^m were measured with the largest errors, because the light from bright and nearby diffraction satellites in this case fall within the aperture when their central images are measured.

The limiting magnitudes in each area differ greatly, depending on the observing conditions and the position in the sky. There are areas with a limiting magnitude of 13^m1 (area no. 28) or 13^m9 (area no. 29); on the other hand, there are areas with a limiting magnitude of 18^m0 (area no. 110).
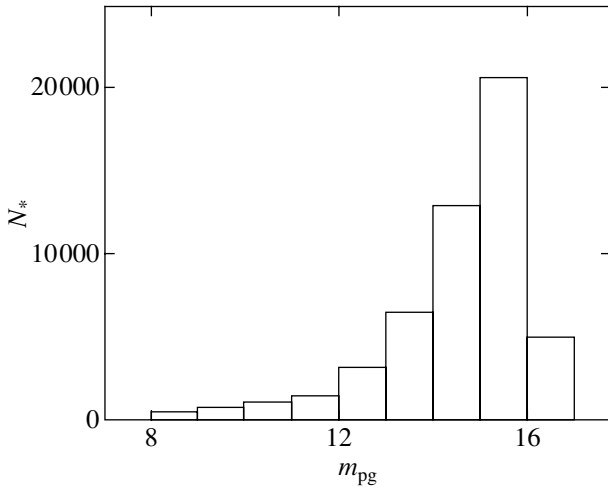
Fig. 1. Distribution of PUL2 stars in photographic magnitude.

THE REDUCTION MODEL

The Relative Proper Motions of Stars

We use an indirect absolutization method as the basis for deriving the absolute proper motions of PUL2 stars. It implies that, at the first stage, the proper motions of the stars being measured are determined relative to a group of reference stars. We use a reduction model with six constants:

$$\Delta x = a_x x + b_x y + c_x, \qquad (1)$$
$$\Delta y = a_y x + b_y y + c_y,$$

where $\Delta x = x_2 - x_1$ and $\Delta y = y_2 - y_1$ are the differences between the measured coordinates, the subscripts denote the epoch of observation, and $a_{x,y}, b_{x,y}, c_{x,y}$ are the plate constants. To determine the plate constants for each pair of plates from reference stars, conditional equations of type (1) are set up and solved by the least-squares method in each coordinate separately; the process is iterative and continues until $|\mu| = \sqrt{\mu_x^2 + \mu_y^2} < 0.05''$ yr^{-1} for any reference star. The relative proper motions of the stars being measured can be determined using the formulas

$$\mu_x = (\Delta x - (a_x x + b_x y + c_x))M/\Delta\tau, \quad (2)$$
$$\mu_y = (\Delta y - (a_y x + b_y y + c_y))M/\Delta\tau,$$

where μ_x and μ_y are the stellar proper motions; M is the scale of the telescope: $M = 59.56''$ mm^{-1} for the Pulkovo normal astrograph; $\Delta\tau = \tau_2 - \tau_1$ is the difference between the epochs in years; x and y are the measured coordinates of the star in mm; and Δx and Δy are the differences between the measured coordinates of the star.

For each PUL2 area, there are at least three pairs of plates, one of which was taken with a diffraction grating. All pairs of plates have one-hour and five-minute exposures. On the plates taken with a grating, only bright reference stars with a one-hour exposure were measured. The centers of each of the three pairs of plates almost always differ by no more than $10'$ (10 mm). For bright stars (the total of which number in the catalog is 18 250: check, bright reference stars, and some of the stars being measured) for which one-hour and five-minute images and images of the diffraction satellites are available, the weighted mean proper motions were determined, and their random errors in internal convergence were estimated. The proper motion of each bright star was derived, on average, from five independent exposures: three one-hour and two five-minute exposures. For this purpose, the following procedure developed and analyzed by Bobylev (1995) was applied:

(1) All proper motions of the stars were reduced to the system of one-hour exposures. This procedure is necessary, because our preliminary analysis of various exposures has shown that the relative proper motions of stars are determined with the smallest random errors precisely from one-hour exposures. The system of five-minute exposures has the largest errors in the stellar proper motions.

(2) A system of faint (15^m2) reference stars was used to derive both the relative and absolute proper motions of stars. The mean number of such stars on each plate is 50.

(3) The weights were determined by analyzing the mutual differences between the stellar proper motions. The necessity of applying weights stems from the fact that we have heterogeneous observational material, because different exposures, different photographic emulsions, and a diffraction grating on one of the pairs of plates were used. To determine the weights, we used bright reference stars, because these are available for all five exposures. On average, there are 55 bright reference stars on each pair of plates. The relative proper motion of each star was calculated as a weighted mean of $n \leq 8$ independent exposures using the formula

$$\overline{\mu} = \frac{\sum_{i=1}^{n} p_i \mu_i}{\sum_{i=1}^{n} p_i}, \qquad (3)$$

where p_i is the weight of exposure i, $i = 1, \ldots, 8$. The weights were calculated using the formula

$$p_i = \left(\frac{0.014}{\sigma_i}\right)^2, \qquad (4)$$

where σ_i is the dispersion of exposure i in arcsec yr^{-1}; the coefficient $0.014''$ yr^{-1} is the largest mean dispersion whose numerical value was determined from a preliminary analysis. The random error in the proper
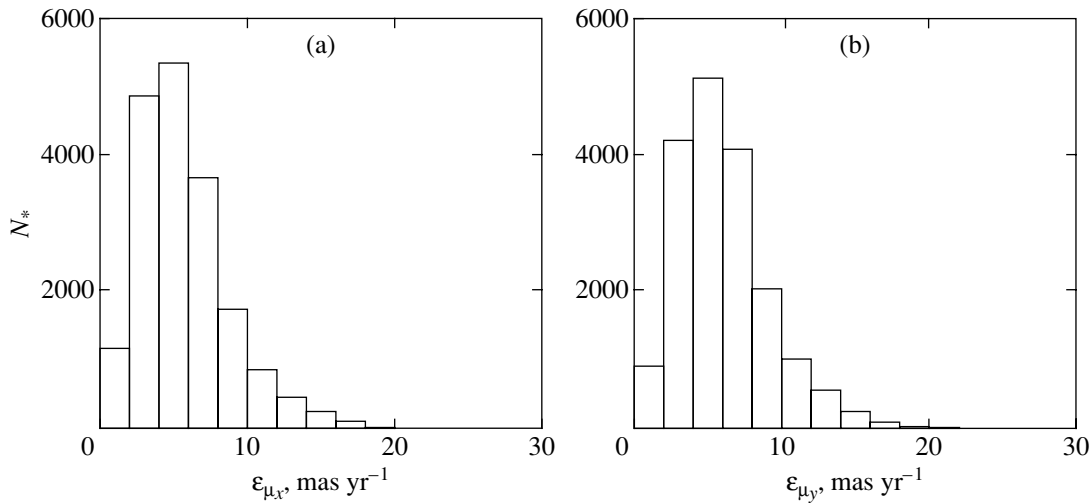
Fig. 2. Distribution of the random errors in the relative proper motions for PUL2 stars: (a) in μ_x with a mean ± 5.5 mas yr^{-1} and (b) in μ_y with a mean ± 5.9 mas yr^{-1}.

motion of a star was calculated as the error of the weighted mean using the formula

$$\varepsilon_\mu = \sqrt{\frac{\sum\limits_{i=1}^{n} p_i (\mu_i - \overline{\mu})^2}{(n-1)\sum\limits_{i=1}^{n} p_i}}. \qquad (5)$$

(4) Each pair of plates was checked for the presence of a magnitude equation. Since no significant magnitude equation was found (Bobylev 1996), we applied no corrections for the magnitude equation to the proper motions of the PUL2 stars.

Figure 1 shows the distribution of PUL2 stars in photographic magnitude. As can be seen from this figure, faint ($\sim 15^m$) stars constitute the bulk of PUL2.

Figure 2 shows the distribution of the random errors in the relative proper motions of all PUL2 stars that were calculated using formula (5). The mean random errors in $\mu_\alpha \cos \delta$ and μ_δ are ± 5.5 and ± 5.9 mas yr^{-1}, respectively.

As can be seen from Fig. 3, the random errors in the relative proper motions of PUL2 stars have no statistically significant dependence on photographic magnitude.

In Fig. 4, the random errors in the relative proper motions of PUL2 stars are plotted against the star position on the plate $d = \sqrt{x^2 + y^2}$, i.e., the distance of the star from the plate center. As can be seen from Fig. 4, the errors in both coordinates increase significantly only outside the $d = 50$ mm ($50'$) circle.

Absolutization

Absolutization is the reduction of the derived relative proper motions of stars to the inertial coordinate frame that is specified in our case by extragalactic objects.

An indirect absolutization method using faint (15^m2) reference stars as an intermediate reference system (Kiselev and Bobylev 1997) serves as the basis for absolutizing the PUL2 relative proper motions.

In this case, the absolutization correction (reduction) for each area, $R_{x,y}$, is calculated as a mean of the proper motions of galaxies in this area taken with the opposite sign:

$$R_x = -(\overline{\mu}_{\text{gal}})_x, \qquad (6)$$
$$R_y = -(\overline{\mu}_{\text{gal}})_y.$$

With regard to referencing to the extragalactic coordinate system, PUL2 is not a homogeneous catalog, because each area contains a different number of galaxies. On average, there are three or four well-measurable images of galaxies in each field. We used a total of about 700 galaxies to absolutize the PUL2 catalog. Since, with rare exceptions, no faint reference stars were measured on plates taken with a grating, the absolutization corrections were calculated mainly as the means of two pairs of plates taken with one-hour exposures. In cases where no faint reference stars were measured on plates taken with a grating, the stellar proper motions were reduced to the system of faint reference stars with a one-hour exposure of the corresponding other pair of plates through common bright reference stars. An analysis of the PUL2 catalog (Bobylev 2000) has shown that the absolutization correction in area no. 72 is
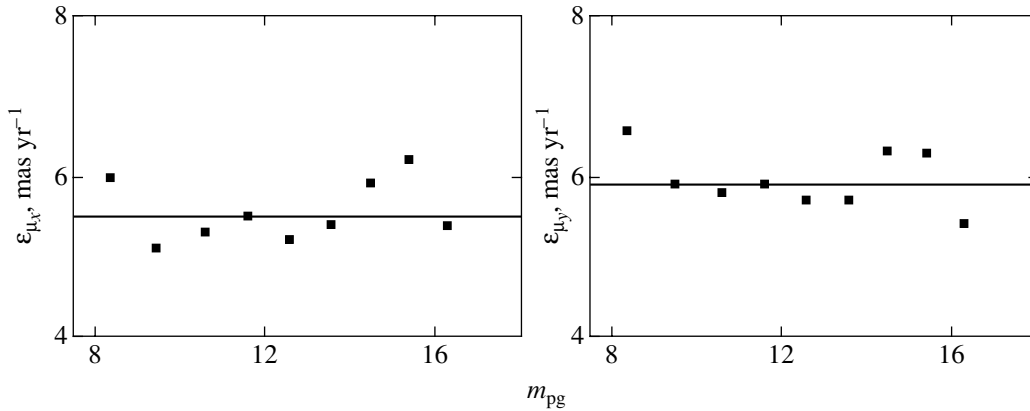
Fig. 3. Random errors in the relative proper motions of PUL2 stars versus photographic magnitude.
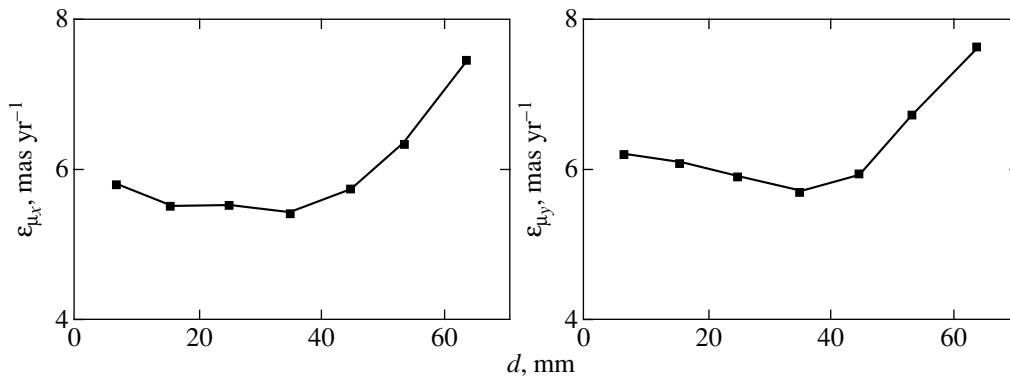

Fig. 4. Random errors in the relative proper motions of PUL2 stars versus star position on the plate.

unreliable. Therefore, only the relative stellar proper motions are of interest in this area.

The PUL2 relative proper motions were derived from two systems of reference stars, bright and faint. For the ten selected areas, there are also the absolute stellar proper motions determined directly, i.e., using galaxies as reference objects (Bobylev 1995). An analysis of three reference systems (Bobylev 1995) showed that when bright stars are used as reference ones, the random errors in the absolute stellar proper motions are comparable to those obtained by using faint reference stars. In this approach, however, the systematic error of the local translation, which was first theoretically analyzed by Kiselev (19989), plays a significant role; its role is quite insignificant when using faint reference stars. Therefore, the system of faint reference stars formed the basis for deriving the PUL2 stellar proper motions.

On average, according to the Oort−Lindblad model (Bobylev 2000), the absolutization error in the PUL2 catalog is ±7.9 mas yr^{-1}.

Equatorial Coordinates of Stars

TRC stars were used as reference ones to calculate the equatorial coordinates of the PUL2 stars. The choice of the reference catalog was dictated by the fact that the stellar proper motion in the TRC catalog does not exceed 0.22″ yr^{-1}. The referencing was performed with a mean random error of ±0.2−0.3″ in each coordinate at the epoch of observation of the second epochs of the PUL2 catalog. The mean coordinates of the PUL2 stars were calculated using at least two pairs of plates of the second epochs. The mean epoch of observation for the plates of the second epochs of the PUL2 catalog is 1975.1. The coordinates of the stars on each of the plates of the second epoch were reduced to epoch J2000.0 using the mean PUL2 absolute proper motions. The mean random errors in the stellar coordinates at epoch J2000.0 calculated in internal convergence are 0.10″−0.14″ in each coordinate. The absolute values of the differences between the coordinates of PUL2 and TRC stars at epoch J2000.0 over the entire plate field do not exceed 5″, the mean of the PUL2−TRC coordinate differences is +0.1″ in each coordinate, and the mean dispersion of the differences is 0.7″ in each coordinate

over the entire plate field and $0.3''$ at the field center. The derived stellar coordinates completely solve the problem of identifying PUL2 stars with stars from other catalogs. The problem of determining highly accurate coordinates of stars in the ICRS system using the Pulkovo database was solved when compiling the PUL3 catalog (Khrutskaya *et al.* 2002).

DESCRIPTION OF THE PUL2 CATALOG

The electronic version of the PUL2 catalog contains 59 766 rows with 92 columns each. Each row contains the following:

(1) columns 1−9, right ascension of the star in the ICRS system at epoch J2000.0, in degrees;

(2) columns 10−18, declination of the star in the ICRS system at epoch J2000, in degrees;

(3) columns 19−25, relative proper motion of the star $\mu_\alpha \cos \delta$, in arcsec yr^{-1};

(4) columns 26−31, random error in the relative proper motion of the star in $\mu_\alpha \cos \delta$, in arcsec yr^{-1};

(5) columns 32−38, relative proper motion of the star μ_δ, in arcsec yr^{-1};

(6) columns 39−44, random error in the relative proper motion of the star in μ_δ, in arcsec yr^{-1};

(7) columns 46−49, photographic magnitude;

(8) column 51, number of independent exposures used to determine the mean stellar proper motion and to calculate the random error in the stellar proper motion;

(9) columns 53−58, absolutization correction R_x, in arcsec yr^{-1}, which must be applied to the relative stellar proper motion to obtain the absolute stellar proper motion;

(10) columns 59−64, absolutization correction R_y, in arcsec yr^{-1}, which must be applied to the relative stellar proper motion to obtain the absolute stellar proper motion;

(11) columns 66−68, field number in the list of the CFS plan (Deutch *et al.* 1955);

(12) columns 70−75, star number in the HIPPARCOS catalog;

(13) columns 77−80, identification star number TYCID1 copied from the TRC catalog;

(14) columns 82−85, identification star number TYCID2 copied from the TRC catalog;

15) column 87, identification star number TYCID3 copied from the TRC catalog;

16) columns 89−92, star number in the field from the PUL2 catalog.

As a sample, Table 1 gives the first 28 rows of the PUL2 catalog. All information is contained in the electronic appendix to this journal. The volume occupied by the electronic catalog is 6.8 Mb.

DETERMINING THE VECTOR $\boldsymbol{\omega}$

The PUL2 catalog contains 1192 stars common to HIPPARCOS and 4385 stars common to TRC.

Table 2 gives the components of the vector of residual rotation of the ICRS system with respect to extragalactic objects $\boldsymbol{\omega}$ $(\omega_x, \omega_y, \omega_z)$ obtained from PUL2−TRC differences as a function of various magnitude constraints. To determine $\omega_x, \omega_y, \omega_z$, we used equations in the form in which they were suggested and used by Lindegren and Kovalevsky (1995):

$$\Delta\mu_\alpha \cos \delta = \omega_x \cos \alpha \sin \delta \qquad (7)$$
$$+ \omega_y \sin \alpha \sin \delta - \omega_z \cos \delta,$$

$$\Delta\mu_\delta = -\omega_x \sin \alpha + \omega_y \cos \alpha, \qquad (8)$$

where the PUL2−TRC differences between the stellar proper motions appear on the left-hand sides. As can be seen from Table 2, a weak magnitude dependence is observed for the component ω_x. For ω_y and, most importantly, ω_z, there is virtually no magnitude dependence. As can be seen from the table, bright stars have smaller errors of a unit weight $\sigma_\circ$; i.e., their proper motions are more accurate than those of faint stars. This was achieved because at least five independent exposures were used to calculate the proper motions of bright PUL2 stars (in this case, at least three pairs of plates for each area was used). We may conclude that the technique used to compile the PUL2 catalog allowed us to minimize the influence of the random error of the magnitude equation in the stellar proper motions.

The Pulkovo normal astrograph, just like any lens objective, has a coma-type error that depends on the star position relative to the optical center (a detailed analysis of 19 objectives similar to the normal astrograph of the Sky Map Program can be found in the paper by Kuimov (1998)). Table 3 gives the components $\omega_x, \omega_y, \omega_z$ obtained by comparing the proper motions of PUL2 and TRC stars as a function of various constraints on the distance of the star from the field center (plate center). An analysis of this table leads us to conclude that small systematic changes in $\omega_x, \omega_y, \omega_z$ take place as the center is approached, without being catastrophic. As the center is approached, the magnitude of ω_z increases. The working constraint on d is $d < 60$ mm, and we used it to obtain the results in Tables 2, 4, and 5. The large d reaching 85 mm should be explained. In several areas, the mismatch between the centers of the pairs of plates reaches 20−30 mm. In these cases, on each specific pair of plates on which the proper motions of stars with large motions were determined, the value of d does not exceed ~60 mm. In contrast, in the combined list for such areas, d reaches large values, but this parameter is formal and does not reflect the actual

Table 1. PUL2 catalog, the first 28 rows

α	δ	$\mu_\alpha \cos\delta$	e_{μ_α}	μ_δ	e_{μ_δ}	m_{pg}	N_{exp}	R_x	R_y	OBL	HIP	TYCID			PUL
												1	2	3	
1.50204	28.27700	−0.0179	0.0101	0.0045	0.0163	7.5	5	−0.0058	−0.0037	1	502	1735	1573	1	4
1.62157	27.89601	−0.0213	0.0030	−0.0214	0.0088	10.4	5	−0.0058	−0.0037	1		1735	1568	1	6
1.62185	27.09005	0.0027	0.0063	−0.0219	0.0050	11.7	5	−0.0058	−0.0037	1	536	1732	807	1	8
1.64808	28.55334	−0.0015	0.0042	−0.0223	0.0147	7.5	5	−0.0058	−0.0037	1	540	1735	2372	1	10
2.02042	27.66363	0.0240	0.0034	0.0090	0.0084	11.3	5	−0.0058	−0.0037	1		1735	2067	1	12
2.25048	28.24753	−0.0015	0.0015	−0.0103	0.0082	6.6	5	−0.0058	−0.0037	1	728	1735	1440	1	14
2.41334	27.30053	−0.0130	0.0030	−0.0102	0.0079	11.1	3	−0.0058	−0.0037	1		1732	367	1	16
2.54298	27.76490	−0.0065	0.0091	−0.0030	0.0113	10.8	3	−0.0058	−0.0037	1		1735	1806	1	18
2.84280	27.24023	−0.0186	0.0038	−0.0107	0.0080	9.9	5	−0.0058	−0.0037	1		1733	423	1	20
2.91574	28.22511	0.0423	0.0073	0.0159	0.0081	9.6	5	−0.0058	−0.0037	1	946	1736	1261	1	22
2.94083	27.51030	0.0170	0.0080	−0.0327	0.0097	8.7	5	−0.0058	−0.0037	1	952	1736	561	1	24
2.95611	27.18509	0.0896	0.0053	−0.0152	0.0063	9.3	5	−0.0058	−0.0037	1		1733	566	1	26
2.95947	28.42319	−0.0959	0.0090	0.0471	0.0129	7.8	5	−0.0058	−0.0037	1	956	1736	1574	1	28
3.01489	27.09929	0.2858	0.0063	−0.0873	0.0056	9.6	5	−0.0058	−0.0037	1	974				30
2.42234	27.49885	0.0029		−0.0282		15.2	2	−0.0058	−0.0037	1					32
2.41390	27.45649	−0.0025		−0.0035		14.9	2	−0.0058	−0.0037	1					33
2.41231	27.47737	0.0291		−0.0177		15.0	2	−0.0058	−0.0037	1					34
2.40775	27.48041	0.0006		−0.0250		15.7	2	−0.0058	−0.0037	1					35
2.36005	27.49712	−0.0036	0.0088	−0.0483	0.0117	11.6	4	−0.0058	−0.0037	1		1732	93	1	36
2.34138	27.48204	−0.0242		−0.0088		14.8	2	−0.0058	−0.0037	1					38
2.34144	27.46355	0.0109		−0.0213		15.3	2	−0.0058	−0.0037	1					39
2.31909	27.43306	0.0362		−0.0085		14.9	2	−0.0058	−0.0037	1					40
2.31613	27.50531	−0.0138		−0.0098		15.7	2	−0.0058	−0.0037	1					41
2.30057	27.48285	−0.0254		−0.0755		14.8	2	−0.0058	−0.0037	1					42
2.29592	27.47816	0.0069		0.0103		15.3	2	−0.0058	−0.0037	1					43
2.29062	27.48818	−0.0180		−0.0181		15.7	2	−0.0058	−0.0037	1					44
2.28923	27.49338	−0.0048		−0.0033		15.6	2	−0.0058	−0.0037	1					45
2.25859	27.50863	0.0089	0.0075	−0.0213	0.0038	14.1	4	−0.0058	−0.0037	1					46
...															

influence of the coma of the telescope objective on the accuracy of determining the stellar proper motions.

Table 4 gives the components $\omega_x, \omega_y, \omega_z$ obtained from the PUL2−TRC differences as a function of the color index. An analysis of this table leads us to conclude that the color equation has the strongest effect on the determination of ω_x and does not affect the determination of ω_z. In Fig. 5, residual PUL2−TRC differences between the stellar proper motions are plotted against magnitude. As can be seen from this figure, the PUL2 proper motions have no statistically significant magnitude dependence.

Table 5 gives the components $\omega_x, \omega_y, \omega_z$ obtained from the PUL2−HIP differences as a function of magnitude constraints. We may conclude that ω_x was determined from the PUL2−HIP difference with the

Table 2. Components of the vector $\boldsymbol{\omega}$, ω_x, ω_y, ω_z (in mas yr^{-1}), obtained from PUL2−TRC differences for various magnitude ranges of stars

V	σ_{o}	N_*	ω_x	ω_y	ω_z
$6.0-13^m$	±10.7	3872	-0.11 ± 0.23	$+0.57 \pm 0.20$	-1.55 ± 0.22
$6.0-10.1^m$	±10.7	2002	-0.45 ± 0.32	$+0.44 \pm 0.28$	-1.38 ± 0.29
$10.1-13^m$	±11.0	1870	$+0.24 \pm 0.34$	$+0.70 \pm 0.29$	-1.75 ± 0.32

Note: σ_{o} is the error of a unit weight (in mas yr^{-1}), and N_* is the number of common stars.

Table 3. Components of the vector $\boldsymbol{\omega}$, ω_x, ω_y, ω_z (in mas yr^{-1}), obtained from PUL2−TRC differences for various values of d

d, mm	σ_{o}	N_*	ω_x	ω_y	ω_z
$0-85$	±11.0	4104	-0.16 ± 0.23	$+0.42 \pm 0.20$	-1.50 ± 0.21
$0-40$	±10.6	2417	$+0.14 \pm 0.26$	$+0.32 \pm 0.25$	-1.99 ± 0.26
$40-85$	±11.7	1687	-0.62 ± 0.39	$+0.56 \pm 0.32$	-0.79 ± 0.35

Table 4. Components of the vector $\boldsymbol{\omega}$, ω_x, ω_y, ω_z (in mas yr^{-1}), obtained from PUL2−TRC differences

$B-V$	σ_{o}	N_*	ω_x	ω_y	ω_z
0.47^m	±11.0	1901	$+0.16 \pm 0.34$	$+0.57 \pm 0.29$	-1.60 ± 0.31
1.24^m	±10.9	1971	-0.38 ± 0.33	$+0.58 \pm 0.28$	-1.50 ± 0.30

Table 5. Components of the vector $\boldsymbol{\omega}$, ω_x, ω_y, ω_z (in mas yr^{-1}), obtained from PUL2−HIP differences

V	σ_{o}	N_*	ω_x	ω_y	ω_z
$2-12.5^m$	±10.7	1004	-0.98 ± 0.47	-0.03 ± 0.38	-1.66 ± 0.42
$6-12.5^m$	±10.6	972	-1.12 ± 0.47	$+0.14 \pm 0.39$	-1.70 ± 0.42
$2-8.55^m$	±11.0	502	-0.75 ± 0.65	$+0.18 \pm 0.56$	-1.89 ± 0.61
$8.55-12.5^m$	±10.4	502	-1.28 ± 0.67	-0.25 ± 0.52	-1.38 ± 0.57

lowest accuracy, and that the magnitude equation and the coma have no significant effect on the determination of ω_z.

DISCUSSION

The values of ω_z obtained here (Table 5) are in good agreement with $\omega_z = -1.4 \pm 0.5$ mas yr^{-1}. The latter was derived from the PUL2−HIP differences for 644 bright stars using special constraints (Bobylev 1998).

The NPM1 catalog reveals a magnitude equation that has a major effect on the determination of ω_z (Kovalevsky *et al.* 1997). For example, the values of $(\omega_x, \omega_y, \omega_z)$ calculated without any magnitude constraints are $(-0.70, -0.27, -2.14)$ mas yr^{-1}, while the values of $(\omega_x, \omega_y, \omega_z)$ calculated in the range $10.6-12.2^m$ are $(-0.85, +0.16, +0.60)$ mas yr^{-1}. Because of the magnitude equation, Kovalevsky *et al.* (1997) did not use any of the solutions of the NPM program, which shares the largest number of common stars with the HIPPARCOS catalog,
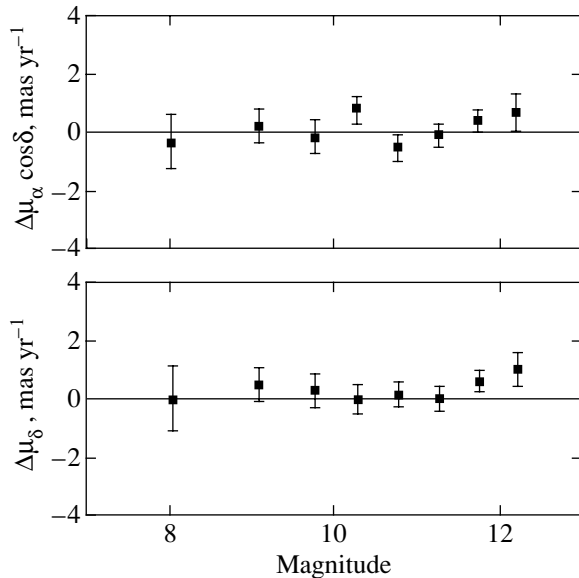
Fig. 5. Residual PUL2−TRC differences between the stellar proper motions versus magnitude.

to derive the final solution when determining the component ω_z.

In the component ω_z of such programs as Kyiv CFS ($\omega_z = -1.07 \pm 0.80$ mas yr^{-1}), NPM ($\omega_z = -2.14$ mas yr^{-1}), SPM ($\omega_z = -0.30 \pm 0.07$ mas yr^{-1}), and VLBI ($\omega_z = -0.33 \pm 0.30$ mas yr^{-1}), there is agreement (these values were taken from the paper by Kovalevsky *et al.* (1997)). In this case, ω_z differs markedly from zero. Our value of $\omega_z = -1.66 \pm 0.42$ mas yr^{-1} agrees with the above values and shows that the problem of controlling the inertiality of the ICRS system has not yet been ultimately solved. A kinematic analysis of the proper motions of HIPPARCOS stars (Bobylev 2004) indicates that the ICRS system has a noticeable rotation with an angular velocity -0.36 ± 0.09 mas yr^{-1} around the Galactic y axis. In the equatorial coordinate system, the angular velocity of the rotation around the Galactic y axis depends precisely on ω_z.

CONCLUSIONS

The PUL2 catalog is the end result of the long-term work of the large staff of the Pulkovo Observatory aimed at implementing Deutch's plan. An advantage of the PUL2 catalog is that, in contrast to similar catalogs (NPM, Kyiv CFS, and SPM), it has no statistically significant magnitude dependence of the absolute stellar proper motions.

The values of $\omega_x, \omega_y, \omega_z$ obtained by comparing the proper motions of PUL2 and HIPPARCOS stars may be used to derive the most probable components of the vector $\boldsymbol{\omega}$, in particular, the most problematic component ω_z.

REFERENCES

1. V. V. Bobylev, Candidate's Dissertation in Mathematical Physics (Glavn. Astron. Obs., St. Petersburg, 1995).
2. V. V. Bobylev, Izv. Glavn. Astron. Obs. **210**, 243 (1996).
3. V. V. Bobylev, in *Proceedings of the IV Meeting of Astronomical Society* (Sovrem. Pisatel', Moscow, 1998), p. 66 [in Russian].
4. V. V. Bobylev, Izv. Glavn. Astron. Obs. **214**, 275 (2000).
5. V. V. Bobylev, Pis'ma Astron. Zh. **30**, 289 (2004) [Astron. Lett. **30**, 159 (2004)].
6. N. M. Bronnikova and N. A. Shakht, Izv. Glavn. Astron. Obs. **204**, 52 (1987).
7. N. M. Bronnikova, V. V. Bobylev, N. A. Shakht, and S. A. Usovich, Izv. Gos. Astron. Obs. **210**, 250 (1996).
8. A. R. Clemola, R. B. Hanson, and B. F. Jones, *Galactic and Solar System Optical Astrometry,* Ed. by L. V. Morrison and G. F. Gilmore (Cambridge Univ. Press, 1994), p. 20.
9. A. N. Deutch, IAU Trans. **8**, 789 (1954).
10. A. N. Deǐch, V. V. Lavdovskiǐ, and N. V. Fatchikhin, Izv. Glavn. Astron. Obs. **154**, 14 (1955).
11. W. Diekvoss, O. Heckmann, H. Kox, *et al.*, *Star Catalog of Position and Proper Motions North − 2.5° Declination* (Bergedorf, Hamburg, 1975), Vols. 1−8.
12. N. V. Fatchikhin, Tr. Glavn. Astron. Obs., Ser. II **81**, 3 (1974).
13. B. P. Gerasimovich and N. I. Dneprovskiǐ, in *Proceedings of the Astronomical Conference, Pulkovo, 1933*, p. 137 [in Russian].
14. *The HIPPARCOS and Tycho Catalogues*, ESA SP-1200 (ESA, 1997).
15. E. Hog, A. Kuzmin, U. Bastian, *et al.*, Astron. Astrophys. **333**, L65 (1998).
16. E. V. Khrutskaya, M. Yu. Khovrichev, and N. M. Bronnikova, Izv. Glavn. Astron. Obs. **216**, 336 (2002).
17. A. A. Kiselev, *Theoretical Foundations of Photographic Astrometry* (Nauka, Moscow, 1989) [in Russian].
18. A. A. Kiselev and V. V. Bobylev, *Structure and Evolution of Stellar Systems,* Ed. by T. A. Agekian, A. A. Mülläri, and V. V. Orlov (St. Petersburg, 1997), p. 199.

19. V. S. Kislyuk, S. P. Rybka, A. I. Yatsenko, *et al.*, Astron. Astrophys. **321**, 660 (1997).

20. J. Kovalevsky, L. Lindegren, M. A. C. Perryman, *et al.*, Astron. Astrophys. **323**, 620 (1997).

21. A. Kuzmin, E. Hog, U. Bastian, *et al.*, Astron. Astrophys., Suppl. Ser. **136**, 491 (1999).

22. K. V. Kuimov, Doctoral Dissertation in Mathematical Physics (Sternberg Astron. Inst. Mos. Gos. Univ., Moscow, 1998).

23. L. Lindegren and J. Kovalevsky, Astron. Astrophys. **304**, 189 (1995).

24. G. N. Neuĭmin, *Working Catalogue of Extragalactic Nebulae for the Faint Stars Catalogue Clasure,* Uch. Zap. Kazan. Univ. **100** (4), 86 (1940).

25. I. Platais, T. M. Girard, W. F. van Altena, *et al.*, Astron. Astrophys. **304**, 141 (1995).

26. S. Rëser and U. Bastian, *PPM Star Catalogue. Position and Proper Motions of 181 731 Stars >−2.5°* (Publ. Astronomischers Rechen.-Inst., Heidelberg, 1991−1993), Vols. 1−4.

27. S. P. Rybka and A. I. Yatsenko, Kinemat. Fiz. Neb. Tel **13**, 70 (1997a).

28. S. P. Rybka and A. I. Yatsenko, Astron. Astrophys., Suppl. Ser. **121**, 243 (1997b).

Translated by V. Astakhov

Pulsations of Microwave Emission and Flare Plasma Diagnostics

A. V. Stepanov[1]*, Yu. G. Kopylova[1], Yu. T. Tsap[2],
K. Shibasaki[3], V. F. Melnikov[4], and T. B. Goldvarg[5]

[1]*Pulkovo Astronomical Observatory, Russian Academy of Sciences, Pulkovskoe shosse 65, St. Petersburg, 196140 Russia*

[2]*Crimean Astrophysical Observatory, p/o Nauchnyi, Crimea, 334413 Ukraine*

[3]*National Astronomical Observatory, Nobeyama, Japan*

[4]*Research Institute of Radiophysics, Nizhni Novgorod State University, ul. Bolshaya Pechorskaya 25/14, GSP-51, Nizhni Novgorod, 603950 Russia*

[5]*Kalmyk State University, Élista, Russia*

Received January 15, 2004

Abstract—We consider the modulation of nonthermal gyrosynchrotron emission from solar flares by the ballooning and radial oscillations of coronal loops. The damping mechanisms for fast magnetoacoustic modes are analyzed. We suggest a method for diagnosing the plasma of flare loops that allows their main parameters to be estimated from peculiarities of the microwave pulsations. Based on observational data obtained with the Nobeyama Radioheliograph (17 GHz) and using a technique developed for the event of May 8, 1998, we determined the particle density $n \approx 3.7 \times 10^{10}$ cm^{-3}, the temperature $T \approx 4 \times 10^7$ K, and the magnetic field strength $B \approx 220$ G in the region of flare energy release. A wavelet analysis for the solar flare of August 28, 1999, has revealed two main types of microwave oscillations with periods $P_1 \approx 7$, 14 s and $P_2 \approx 2.4$ s, which we attribute to the ballooning and radial oscillations of compact and extended flare loops, respectively. An analysis of the time profile for microwave emission shows evidence of coronal loop interaction. We determined flare plasma parameters for the compact ($T \approx 5.3 \times 10^7$ K, $n \approx 4.8 \times 10^{10}$ cm^{-3}, $B \approx 280$ G) and extended ($T \approx 2.1 \times 10^7$ K, $n \approx 1.2 \times 10^{10}$ cm^{-3}, $B \approx 160$ G) loops. The results of the soft X-ray observations are consistent with the adopted model. © 2004 MAIK "Nauka/Interperiodica".

Key words: *Sun, flare loops, MHD oscillations, ballooning mode, gyrosynchrotron emission, plasma diagnostics.*

INTRODUCTION

More than 30 years ago, Rosenberg (1970) proposed associating the short-period pulsations of type IV radio bursts with the magnetohydrodynamic (MHD) oscillations of coronal loops. Subsequently, this idea was developed by many authors (see the reviews by Aschwanden (1987, 2003)), but no convincing evidence for the validity of this approach has been found until recently.

In the late 1990s, ultraviolet observations with a high spatial resolution from the TRACE satellite revealed oscillations of coronal loops in active regions (Aschwanden *et al.* 1999), which provided a strong impetus for the rapid development of a promising new direction of research called coronal seismology. Such great interest is largely explained by the possibility of a further improvement in the methods for diagnosing

the coronal magnetic fields in the region of flare energy release (see, e.g., Zaĭtsev and Stepanov 1982; Nakariakov and Ofman 2001; Kopylova *et al.* 2002).

It is well known that the radial fast magnetoacoustic (FMA) oscillations of coronal loops can lead to second (0.5−5 s) oscillations of emission from solar flares (Rosenberg 1970; Zaĭtsev and Stepanov 1982; Kopylova *et al.* 2002). Emission oscillations with a period $P = 10−30$ s are commonly observed; these oscillations are generally attributed to Alfvén or kink modes (Zaĭtsev and Stepanov 1989; Qin *et al.* 1996). At the same time, if the plasma parameter $\beta = 8\pi\kappa nT/B^2$ is not too small, then the ten-second oscillations can be attributed to the development of a ballooning mode (Kopylova and Stepanov 2002). In this case, the corresponding disturbances will cause no appreciable change in the magnetic energy of the system (Mikhaĭlovskiĭ 1971), and they must be generated more efficiently than

kink modes, because the gas pressure inside the flare loop increases. In particular, this is suggested both by microwave observations with the Nobeyama Radioheliograph (Shibasaki 1998) and by the physical model (Shibasaki 2001).

The radial and ballooning oscillations are similar in properties to FMA modes, because they cause a periodic variation of the loop cross section. Therefore, they must be strongly damped: their Q cannot be too high ($Q \leq 10-30$), which is in satisfactory agreement with the observational data obtained in various wavelength ranges (see, e.g., Asai et al. 2001). In this case, as Zaĭtsev and Stepanov (1982) showed, the Q-factor of the FMA oscillations in flare loops is determined by electron thermal conduction. In several cases, however, ion viscosity plays a more significant role in the dissipation of these modes (Kopylova et al. 2002). Consequently, the damping mechanisms for the modes under consideration should be studied additionally.

The generation of FMA oscillations in coronal loops causes changes in the magnetic field strength, the characteristic sizes of the emitting region, and the plasma temperature and density. As a result, emission oscillations with periods $P = 1-30$ s can manifest themselves simultaneously in many wavelength ranges. At the same time, since the gyrosynchrotron emission is highly sensitive to magnetic field variations, searching for a correlation between the FMA oscillations of loops and the modulation of microwave emission from solar flares is of particular interest. In this paper, based on the main principles of the technique proposed by Zaĭtsev and Stepanov (1982), we estimate the plasma parameters from the pulsation characteristics of nonthermal gyrosynchrotron emission; this technique is widely used to diagnose the plasma of both solar (see, e.g., Qin et al. 1996) and stellar (Mathioudacis et al. 2003) flares. A detailed analysis of the dissipative and modulation processes associated with the generation of MHD oscillations in flare loops underlies this technique.

In the next section, we analyze the physical properties of the ballooning and radial modes and discuss the peculiarities of their dispersion relations. In Section 2, we consider the damping mechanisms for the FMA oscillations of coronal magnetic loops. In Section 3, attention is concentrated on the modulation of nonthermal gyrosynchrotron emission by FMA oscillations and on the methods for diagnosing the flare plasma using microwave pulsation parameters. Section 4 is devoted to applications of the proposed technique. In the Conclusion, we formulate our main results.

1. BALLOONING AND RADIAL OSCILLATIONS

Two (drift and MHD) approximations can be used to describe the ballooning mode of flute perturbations. The difference between these two approaches is that, in the drift approximation, the magnetization currents are disregarded, while in the MHD approximation, the displacement current is ignored by formally assuming it to be equal to zero (Tsap and Kopylova 2003). In ideal MHD, which also remains valid for a magnetized plasma with isotopic gas pressure (Volkov 1964), flute perturbations develop through the imbalance between the forces exerted on a given plasma volume. As follows from the linearized MHD equations, the expression for the second variation of the potential energy of a system with a sharp boundary can be represented as (Meyer et al. 1977)

$$\delta W = \delta W_{\mathrm{i}} + \delta W_{\mathrm{e}} + \oint_S \frac{\langle p \rangle}{R} \xi_n^2 dS,$$

where the subscripts correspond to the change in energy inside (i) and outside (e) the magnetic configuration, while the last term describes the effects attributable to the action of the centrifugal force $\langle p \rangle / R$, $\langle p \rangle = p_{\mathrm{e}} - p_{\mathrm{i}}$ is the gas pressure difference, and ξ_n is the transverse displacement. It is easy to show that, in the solar corona, where the radius of curvature of magnetic field lines $R \gg r$ (r is the small loop radius), the curvature effects in the first two terms on the right-hand side of this equation may be disregarded; i.e., it describes the well-studied oscillations of the magnetic flux tube. If, however, the radius of curvature R is small enough and if the gas pressure difference inside and outside the loop is large, then the surface integral can play a significant role. In particular, this integral is responsible for the generation of ballooning oscillations and flute instability. We particularly emphasize that the above equation is valid only for conservative systems; i.e., it describes only the nonemitting modes. Thus, by the ballooning oscillations of coronal loops, we mean the FMA modes slightly modified by the centrifugal force (the perturbations are elongated along the magnetic field) that do not generate MHD waves in the surrounding medium. Their period, as that for the corresponding modes of the magnetic flux tube (Nakariakov et al. 2003), is determined by the longitudinal loop scale. The estimates obtained in ideal MHD using the method of normal modes also provide evidence for the analogy between the flute and FMA modes. As applied to the Earth's magnetosphere, Burdo et al. (2000) used the system of linear differential equations of ideal MHD in curvilinear coordinates to show that the dispersion relations for

magnetoacoustic and ballooning oscillations at small values of β and the gas pressure gradient are almost identical. This suggests that the modes under consideration are similar in physical properties; in particular, the same dissipative processes must govern their damping.

The dispersion relation for the ballooning mode can be represented as (Mikhaĭlovskiĭ 1974; Pustil'nik 1973)

$$\omega^2 - k_{||}^2 v_A^2 = -\frac{p}{R\rho d};\qquad(1)$$

$$d = \begin{cases} a, & a \gg \lambda_\perp \\ \lambda_\perp, & a \ll \lambda_\perp. \end{cases}$$

Here, $a = n(\partial n/\partial x)^{-1}$ and $\lambda_\perp$ are, respectively, the scale size of the plasma density nonuniformity and the transverse (to the magnetic field) size of the plasma tongue, and $v_A = B/\sqrt{4\pi\rho}$ is the Alfvén speed. Since the loop footpoints are frozen in the photosphere, the relation $k_{||} = N\pi/L$ holds for the longitudinal component of the wave vector, where N is the number of oscillating regions that fit into the loop length L. Setting the period $P_1 = 2\pi/\omega$, we then obtain from (1)

$$P_1 = \frac{2L}{v_A} \left(N^2 - \frac{L\beta}{2\pi d} \right)^{-1/2}.\qquad(2)$$

Taking $L = 10^9 - 10^{10}$ cm, $d = 10^8 - 10^9$ cm, and $\beta \sim 0.1$ for flare loops, we conclude from (2) that $L\beta/(2\pi d) \ll 1$; i.e., the period of the ballooning oscillations is

$$P_1 \approx \frac{2L}{v_A N}.\qquad(3)$$

Relation (3) is formally identical to the equation derived previously by Pustil'nik (1973). However, this author assumed the square of the frequency to be negative ($\omega^2 < 0$), i.e., considered the absolute instability, which is not related to the free oscillations of the magnetic loop.

For the period P_2 of the radial oscillations of a coronal loop (sausage modes), we use the expression (Zaĭtsev and Stepanov 1982)

$$P_2 = \tilde{r}/\sqrt{c_s^2 + v_A^2}, \tilde{r} = 2\pi r/\eta_j.\qquad(4)$$

Here, $\eta_j = 2.4, 5.52,$ and 8.65 correspond to zeros of the Bessel function $J_0(\eta)$, where $\eta = \omega r/\sqrt{c_s^2 + v_A^2}$, c_s is the speed of sound, and r is the radius of the transverse loop cross section. Equation (4) was derived for the emitting modes, i.e., for the loop oscillations that lead to the generation and propagation of traveling MHD waves in the surrounding medium. When the condition $J_0(\eta) = 0$ is satisfied, from which (4) follows, the perturbation amplitude of

the total pressure (the sum of the gas and magnetic pressures) at the outer loop boundary is small, which sharply reduces the outflow of oscillation energy into the outer region (Kopylova *et al.* 2002). Thus, Eq. (4) reflects the relationship between the eigenfrequencies of the loop oscillations and the acoustic damping mechanism (Zaĭtsev and Stepanov 1975; Kopylova *et al.* 2002).

At small plasma parameters β, when $\omega < k_{||}v_A$, no traveling waves are generated in the outer loop region (Roberts 1986). Hence, using Eq. (4) to estimate the radial oscillation period can lead to incorrect conclusions. However, since in this case

$$l < v_A P_2/2,\qquad(5)$$

taking the characteristic values of the Alfvén speed in the corona $v_{A_e} \approx 10^8$ cm s^{-1} and the period $P_2 = 1-10$ s, we obtain $l < 0.5 \times (10^8 - 10^9)$ cm from (5). Consequently, the possibility of the generation of short-period nonemitting radial modes in the solar corona appears problematic.

2. THE DAMPING OF FMA OSCILLATIONS

As follows from observations, the density of the matter ρ_i inside flare loops is two to three orders of magnitude higher than its density ρ_e outside (Doschek 1994). As a result, the acoustic damping of the radial FMA oscillations of coronal loops caused by the emission of MHD waves into the surrounding medium becomes insignificant (Zaĭtsev and Stepanov 1975; Kopylova *et al.* 2002). In addition, at $k_{||}^2/k_\perp^2 \approx (r/L)^2 \geq \rho_e/\rho_i$ (the so-called thick loop), the condition for total internal reflection of FMA waves is satisfied, and the flux tube is an ideal cavity (Meerson *et al.* 1978). Therefore, we restrict our analysis below only to dissipative processes. The oscillation damping decrements attributable to Joule (γ_j) and radiative (γ_r) losses as well as to thermal conduction (γ_c) and ion viscosity (γ_v) can be represented as (Braginskiĭ 1963; Tsap 2000)

$$\gamma_j = \frac{1}{\sqrt{2}} \frac{m}{M} \frac{\omega^2}{\omega_{Bi}^2} \nu_{ei},\qquad(6)$$

$$\gamma_r = \frac{2\pi}{3} \frac{n^2 R(T)}{B^2} \sin^2\theta,\qquad(7)$$

$$\gamma_c = \frac{1}{3} \frac{M}{m} \frac{\omega^2}{\nu_{ei}} \beta^2 \cos^2\theta \sin^2\theta,\qquad(8)$$

$$\gamma_v = \frac{1}{12} \sqrt{\frac{M}{2m}} \frac{\omega^2}{\nu_{ei}} \beta \sin^2\theta.\qquad(9)$$

Here, m and M are the electron and ion masses, respectively; $\theta = \arctan(k_\perp/k_{||})$ is the angle between the direction of the magnetic field **B** and the wave

vector $\mathbf{k}$; $\omega_{Bi} \approx 9.6 \times 10^3$, B is the ion gyrofrequency; $R(T) = 5 \times 10^{-20}/\sqrt{T}$ is the radiative loss function for the temperature range $T = 10^6 - 10^7$ K (Priest 1982); and the effective electron−ion collision frequency is

$$\nu_{ei} = \frac{5.5n}{T^{3/2}} \ln\left(10^4 \frac{T^{2/3}}{n^{1/3}}\right) \approx 60\frac{n}{T^{3/2}}. \qquad (10)$$

Kopylova *et al.* (2002) showed that ion viscosity is mainly responsible for the energy losses of the quasi-transverse oscillations in coronal loops. Meanwhile, the flare loops are inhomogeneous. Thus, for example, the loop top region often has enhanced plasma density and temperature (see, e.g., Petrosian *et al.* 2002). This suggests that the FMA oscillations of loops are generated through flare energy release not in the entire loop, but in some local regions with the highest gas pressure. As a result, the approximation of quasi-transverse oscillations ($k_{\parallel} \ll k_{\perp}$) becomes inapplicable. To find out which of the dissipation mechanisms dominates at various angles θ, let us compare the damping decrements. It follows from formulas (6)−(10) that at typical plasma parameters of coronal flare loops $T \approx 10^7$ K, $n \approx 10^{10} - 10^{11}$ cm^{-3}, and $\theta = 30° - 90°$, $\beta = 0.03 - 0.3$ (Doschek 1994), the damping of FMA oscillations is determined by thermal conduction and ion viscosity, with

$$\frac{\gamma_v}{\gamma_c} \approx \frac{4 \times 10^{-3}}{\beta \cos^2 \theta}. \qquad (11)$$

Assuming the plasma parameter in (11) to be $\beta = 0.1$, we conclude that the energy losses due to ion viscosity are smaller than those due to thermal conduction for $\theta \leq 78°$. Since $\theta \approx \arctan(l/r)$ for coronal loops, where l is the scale size of the longitudinal perturbation, electron thermal conduction plays a crucial role in the dissipation of oscillations for $l/r < 5-6$ (Zaĭtsev and Stepanov 1982).

3. THE MODULATION OF EMISSION AND FLARE PLASMA DIAGNOSTICS

Let us consider the influence of the radial and ballooning oscillations of coronal loops on the non-thermal microwave emission from solar flares for which the gyrosynchrotron mechanism is generally responsible (Bastian 1998). Since the microwave emission at frequencies >10 GHz is optically thin (Bastian 1998), its spectral flux can be represented as

$$F_f = \eta_f D\Omega, \qquad (12)$$

where Ω is the solid angle of the source, and D is its geometrical thickness. In this case, for the nonthermal gyrosynchrotron emission coefficient η_f (Dulk

and Marsh 1982),

$$\frac{\eta_f}{Bn_a} = 3.3 \times 10^{-24-0.52\delta} \qquad (13)$$

$$\times (\sin \Theta)^{-0.43+0.65\delta} \left(\frac{f}{f_B}\right)^{1.22-0.90\delta},$$

where n_a is the density of the accelerated electrons, $\Theta > 20°$ is the angle between the magnetic field direction and the line of sight, $\delta = 2-7$ is the spectral index of the accelerated electrons, and $f_B = eB/(2\pi mc)$ is the electron gyrofrequency ($f/f_B = 10-100$).

Relation (13) was derived for an isotropic population of accelerated particles. Since the emission coefficient η_f depends strongly on the electron pitch-angle distribution (Fleishman and Melnikov 2003), this assumption imposes severe constraints on the applicability of (13) to specific flare events. However, there is currently ample evidence that a coronal loop can be represented as a magnetic trap (a magnetic bottle) in which the trapped electrons are responsible for the observed microwave emission. For intense flares, moderate and strong diffusion characterized by an almost isotropic particle distribution must dominate in coronal magnetic bottles (Stepanov and Tsap 2002).

Previously, Kopylova *et al.* (2002) studied the influence of the FMA oscillations of loops on the density modulation of the trapped particles responsible for the microwave emission in terms of the coronal magnetic bottle model. According to the results obtained, their density does not vary in the regime of moderate diffusion ($n_a = $ const). Taking into account (13), we then obtain

$$\eta_f \propto B^{0.9\delta-0.22}. \qquad (14)$$

Using (12) and (14) and the conservation condition for the longitudinal magnetic flux ($D \propto B^{-1/2}$, $\Omega \propto B^{-1/2}$), we find that

$$F_f \propto B^{0.9\delta-1.22}. \qquad (15)$$

We define the modulation depth as $\Delta = (F_{\max} - F_{\min})/F_{\max}$, where $F_{\max}$ and $F_{\min}$ are the maximum and minimum fluxes. If the oscillation amplitude of the magnetic field is $\delta B \ll B$, then, according to (15), we obtain

$$\Delta = 2\xi\frac{\delta B}{B}, \xi = 0.9\delta - 1.22. \qquad (16)$$

As we see from relations (16), for the gyrosynchrotron mechanism, the FMA oscillations of a magnetic flux tube can lead to a significant modulation of the emission. Thus, for example, if $\delta B = 0.05B$ and $\delta = 4.5$, then the modulation depth is $\Delta \approx 0.3$.

Table 1. Formulas for calculating the plasma parameters from the characteristics of the emission pulsations caused by the ballooning and radial oscillations of a coronal loop

Ballooning oscillations	Radial oscillations
$T = 2.42 \times 10^{-8} \dfrac{L^2 \varepsilon_1}{N^2 P_1^2}$	$T = 1.2 \times 10^{-8} \dfrac{\tilde{r}^2 \varepsilon_2}{P_2^2 \chi}$
$n = 5.76 \times 10^{-11} \dfrac{Q_1 L^3 \varepsilon_1^{7/2} \sin^2 2\theta}{N^3 P_1^4}$	$n = 2 \times 10^{-11} \dfrac{Q_2 \tilde{r}^3 \varepsilon_2^{7/2} \sin^2 2\theta}{P_2^4 \chi^{3/2}}$
$B = 6.79 \times 10^{-17} \dfrac{Q_1^{1/2} L^{5/2} \varepsilon_1^{7/4} \sin 2\theta}{N^{5/2} P_1^3}$	$B = 2.9 \times 10^{-17} \dfrac{Q_2^{1/2} \tilde{r}^{5/2} \varepsilon_2^{7/4} \sin 2\theta}{P_2^3 \chi^{5/4}}$

Note: $\chi = 10\varepsilon/3 + 2$, the temperature T is in K, the density n is in cm^{-3}, and the magnetic field B is in G.

Assuming that the ballooning and radial oscillations are generated in flare loops through a sharp rise in the gas pressure, we obtain for the plasma parameter (Zaĭtsev and Stepanov 1982)

$$\beta \approx 2\delta B/B = \Delta/\xi \equiv \varepsilon. \qquad (17)$$

As we showed in the previous section, if the angle between the direction of the magnetic field **B** and the wave vector $\theta < 78°$, then electron thermal conduction makes the largest contribution to the damping of the FMA oscillations of coronal loops. Therefore, given (8), the Q-factor can be represented as

$$Q = \frac{\omega}{\gamma_c} \approx 6.5 \times 10^{-2} \frac{PnT^{-3/2}}{\beta^2 \sin^2 2\theta}. \qquad (18)$$

Combining relations (3), (4), (16)−(18) yields formulas for determining the flare plasma parameters from the characteristics of the microwave pulsations caused by the ballooning and radial oscillations of coronal loops (see Table 1).

4. APPLYING THE DIAGNOSTICS METHOD

As an illustration of the suggested plasma diagnostics method, let us consider two flare events whose microwave emission exhibited quasi-periodic pulsations that corresponded in time scale to the radial and ballooning oscillations of coronal magnetic loops.

The Flare of May 8, 1998

This M 3.1 X-ray class event occurred in the active region NOAA 8210 with coordinates S15 W82 in the time interval 01:49−02:17 UT. Figure 1a shows the time profile for the emission of the impulsive phase of the flare obtained with the Nobeyama Radioheliograph at a frequency of 17 GHz (Nakajima *et al.* 2002). It follows from a Fourier analysis that the characteristic microwave pulsation period is $P_1 \approx 16$ s. The hard X-ray source observed from the

Yohkoh satellite (Sato *et al.* 1998) in channels L (14−23 keV) and M$_1$ (23−33 keV) is shown in Fig. 2b. The nonuniformity of its structure strongly suggests that a ballooning mode can be generated. Therefore, we may assume that the observed radio pulsations whose phase and period instability is attributed to small differences in the sizes of the oscillating regions (Fig. 1b) are caused by the oscillations of plasma tongues.

An analysis of the images for hard X-ray sources (see Fig. 1b) shows that four plasma tongues ($N = 4$) with enhanced brightness fit along the flare loop $L \approx 8 \times 10^9$ cm in length. Like in a standing wave, they must oscillate in phase (otherwise, the emission pulsations will be smoothed out). Since the ratio of the characteristic perturbation scales is $l/r \approx 2.25$, the angle $\theta = \arctan(l/r) \approx 66° < 78°$, suggesting that electron thermal conduction plays a dominant role in the damping of ballooning oscillations (see Section 2). The mean relative modulation depth Δ_1 and the oscillation Q_1 can be easily determined from Fig. 1a: $\Delta_1 \approx 0.3$ and $Q_1 \approx \pi s \approx 25$, where s is the number of oscillations. We obtain the plasma parameter $\beta \approx 0.11$ from (16) and (17). Based on a a thick target model (see, e.g., Lee *et al.* 2002), we estimated the spectral index $\delta = 4.5$ using hard X-ray observations (Fig. 1b). Using the formulas in the left part of Table 1, we found the temperature $T \approx 4 \times 10^7$ K, the particle density $n \approx 3.7 \times 10^{10}$ cm^{-3}, and the magnetic field strength $B \approx 220$ G in the region of flare energy release.

The Flare of August 28, 1999

The impulsive phase of this M 2.8 X-ray class solar flare was observed in the time interval 00:55−00:58 UT in the active region NOAA 8674 with coordinates S25 W11 (Yokoyama *et al.* 2002). Microwave observations with the Nobeyama Radioheliograph (17 and 34 GHz) showed that the flare region
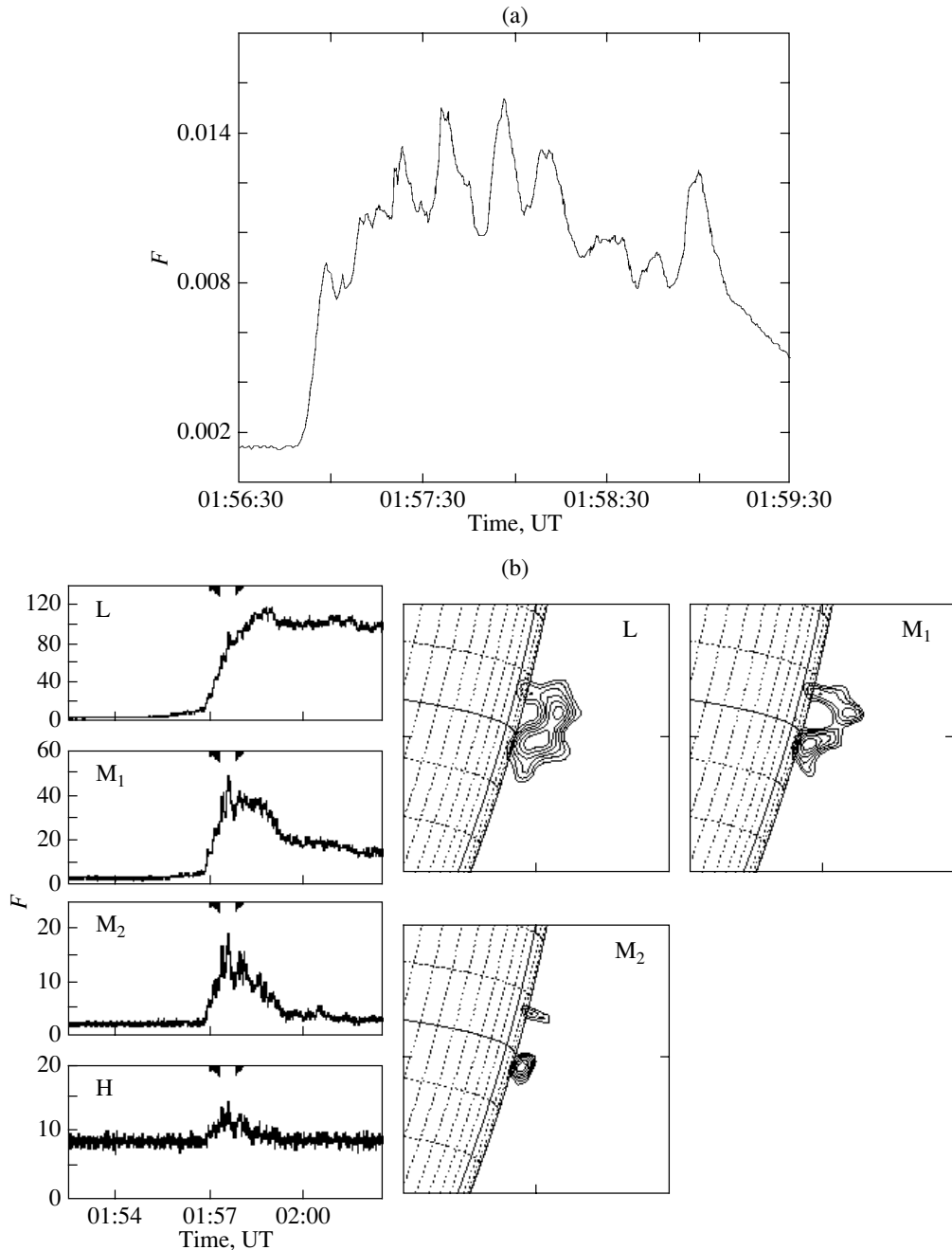
(a)

(b)

Fig. 1. (a) Time profile for the microwave emission from the solar flare of May 8, 1998, obtained with the Nobeyama Radioheliograph (17 GHz). The relative difference between the flare and background spectral fluxes is along the vertical axis. (b) The time profiles for the hard X-ray fluxes in channels L (14−23 keV), M_1 (23−33 keV), M_2 (33−53 keV), and H (53−93 keV) obtained onboard the Yohkoh satellite (left panel) and an image of hard X-ray sources in channels L, M_1, and M_2.

consisted of two emission sources. The first, compact ($\leq 10''$) source was located near a sunspot, while the second source was above the first one and slowly propagated along an extended ($>70''$) X-ray coronal loop with a velocity of $\approx 1.4 \times 10^4$ km s^{-1} (Yokoyama et al. 2002). The flare was accompanied by a quasi-periodic modulation of the microwave emission with various time scales (see Fig. 2b).

The microwave observations (Fig. 2b) were pro-

cessed by means of a wavelet analysis (Vityazev 2001). We used the Morlet wavelet $\psi(t) = \exp(-t^2/2) \times \exp(i2\pi t)$ as the basis for constructing the integral wavelet transform of our time series $f(t_k)$, $k = 1, \ldots, m$

$$W_\psi(a,b) = \frac{1}{\sqrt{a}} \int\limits_{-\infty}^{+\infty} f(t_k)\psi^*\left(\frac{t-b}{a}\right) dt, \quad (19)$$
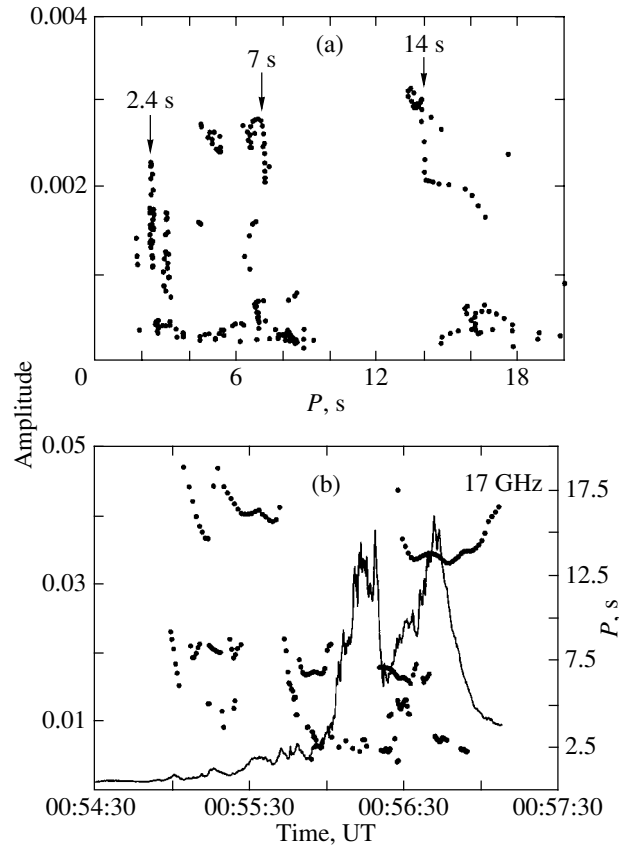
Fig. 2. (a) Dynamic oscillation spectrum constructed by means of a wavelet analysis for the solar flare of August 28, 1999. (b) Time variations of the oscillation period and the time profile for the emission obtained with the Nobeyama Radioheliograph (17 GHz) for the event of August 28, 1999.

where $*$ denotes complex conjugation, and the scale factors a and b determine the extension and shift of the basis wavelet, respectively. In applying the wavelet transform, we found a correlation between the series $f(t_k)$ being analyzed and the chosen wavelet $\psi(t)$, which was extended and shifted in realization length (Vityazev 2001). As a result, a two-dimensional array of coefficients $W_\psi(a, b)$ was formed, from which we calculated the amplitude of the dynamic spectrum

$$A = \sqrt{(8/m\pi)[(\mathrm{Re}W_\psi)^2 + (\mathrm{Im}W_\psi)^2]}.$$

The significance level was taken to be 0.9 and was found as follows:

$$S(P) = 1 - (1 - C^2(P))^{(2m-1)/2-1},$$

where $C(P)$ is is the coefficient of multiple linear correlation between the time series being studied and the wavelet.

The results of our wavelet analysis for the emission intensity at 17 GHz are shown in Figs. 2a and 2b. As follows from the dynamic oscillation spectra constructed by using the procedure described above, the maximum pulsation amplitudes corresponded to

three characteristic periods, $P \approx 14, 7, 2.4\,\mathrm{s}$ (Fig. 2a), whose values changed slightly as the flare developed (Fig. 2b).

The process of flare energy release may be assumed to have been accompanied by the interaction between two neighboring loops through the development of ballooning instability in the compact loop. Indeed, as we see from Fig. 2b, the first type of oscillations with $P_1 \approx 14\,\mathrm{s}$, which we identify with the ballooning mode, has a time gap (00:55:45–00:56:30 UT) that coincides with the onset of propagation of the energetic electron front along the extended loop (Yokoyama *et al.* 2002). It would be natural to attribute this feature to a rise in the gas pressure during flare energy release and to the violation of oscillation conditions in the compact loop, leading to the development of ballooning instability and the injection of hot plasma into the neighboring extended loop. As soon as the compact loop was liberated from the excess pressure, the oscillations of plasma tongues resumed (see the first peak in Fig. 2b). We consider the 7-s oscillations as the second harmonic of the ballooning oscillations, because their behavior was similar to that of the 14-s oscillations and their amplitudes were smaller.

Table 2. Flare plasma parameters for the event of August 28, 1999

Parameters	Extended loop	Compact loop
T, K	2.5×10^7	5.2×10^7
n, cm^{-3}	$(0.5-2.1) \times 10^{10}$	$(1.2-4.8) \times 10^{10}$
B, G	$105-210$	$140-280$
β	0.04	0.11

Since the oscillations with $P_2 \approx 2.4$ s emerged only after the first plasma injection into the large loop (see Fig. 2b), radial modes are most likely responsible for this oscillation branch. The generation of the latter was also determined by an increase in the gas pressure in the extended loop through the injection of hot plasma and energetic particles from the compact loop.

Let us make some estimates in terms of the scenario described above. Since, according to observations, the radius of the cross section of the extended loop is $r = 3 \times 10^8$ cm, $\tilde{r} = 2.62r \approx 7.86 \times 10^8$ cm for the fundamental harmonic of the radial modes ($j = 1$). The pulsation Q-factors are $Q_1 \approx 10$ and $Q_2 \approx 15$, the relative modulation depths are $\Delta_1 \approx 0.4$ and $\Delta_2 \approx 0.1$, and the spectral indices are $\delta_1 = 5.5$ and $\delta_2 = 4$ (Yokoyama *et al.* 2002). Specifying the an-

Fig. 3. Time profiles for the emission measure EM and temperature T of the flare coronal plasma obtained using the technique by Thomas *et al.* (1985) from GOES soft X-ray observations: (a) the flare of May 8, 1998; (b) the flare of August 28, 1999.

gle $\theta = 45°-75°$ for the extended and compact loops ($L = 2 \times 10^9$ cm) in which the radial and ballooning oscillations were generated, respectively, we then calculate the loop parameters presented in Table 2 using the formulas from Table 1. Note that the compact loop, which was directly associated with the primary source of energy release, had higher temperature, density, and magnetic field strength.

The plasma density and temperature for the flares under consideration can be estimated independently from GOES soft X-ray observations. Based on the technique described by Thomas *et al.* (1982), we plotted the effective temperature T and the emission measure for thermal electrons $EM = n^2V$ against time (see Fig. 3). It follows from this figure that the characteristic emission measure and plasma temperature are $EM \sim 10^{49}$ cm^{-3} and $T \sim 10^7$ K, respectively. Taking the volume of the flare loop to be $V \approx \pi r^2 L$, we can determine the plasma density. For the events of May 8, 1998, and August 28, 1999, we obtain, respectively, $V \approx 5 \times 10^{27}$ cm^3, $n \approx 4 \times 10^{10}$ cm^{-3}; $V_1 + V_2 \approx 3.5 \times 10^{27}$ cm^3 (V_1 and V_2 are the volumes of the extended and compact loops), $n \approx 5 \times 10^{10}$ cm^{-3}.

Thus, the plasma temperature T and density n for the flares of May 8, 1998, and August 28, 1999, estimated by using our technique, are consistent with the independent diagnostics based on soft X-ray emission.

CONCLUSIONS

We have considered the dispersion relations and the damping mechanisms for the ballooning and radial oscillations of coronal loops. Based on our results and on an analysis of the modulation of nonthermal gyrosynchrotron emission by FMA modes, we suggest a method for diagnosing the flare plasma using such observed microwave pulsation characteristics as the modulation depth, the Q-factor, and the period of the oscillations. This makes it possible to estimate the density, the temperature, and the magnetic field in the region of flare energy release.

We have shown that ion viscosity and electron thermal conduction mainly contribute to the damping of FMA oscillations, and that the ratio of the damping decrements for these processes is $\gamma_v/\gamma_c \sim \cos^{-2}\theta$. Therefore, the Q-factor of the ballooning and local radial oscillations of flare loops is mainly determined by electron thermal conduction.

As follows from the dispersion relations, the second oscillations of coronal loops are most likely caused by radial modes (see also the review by Aschwanden 2003). In turn, we attributed the observed ten-second oscillations to the ballooning oscillations
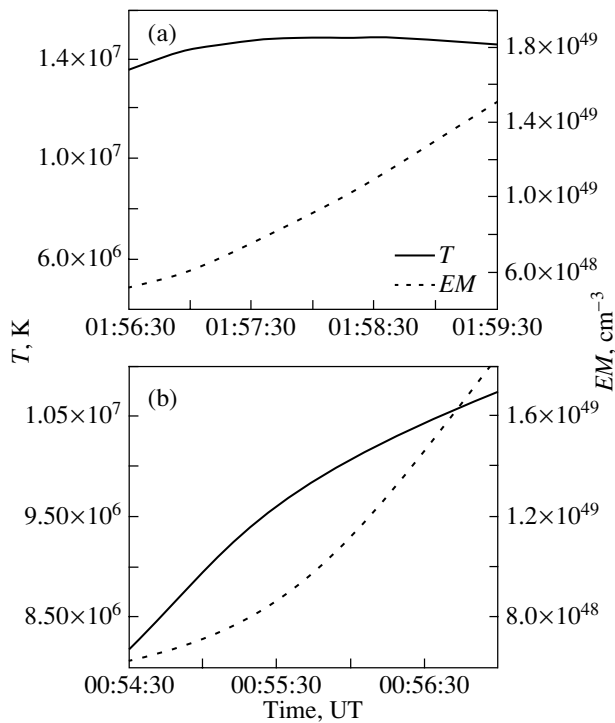
of coronal loops that can be generated in local regions with an enhanced gas pressure (Shibasaki 2001).

To determine the plasma parameters, we chose two solar flares whose microwave emission was accompanied by pulsations with various time scales. The apparent shapes of the emission sources in various wavelength ranges, the characteristic periods, and the relationship between the dynamics of energy release and features of the emission oscillations suggest that the fine structure of the emission for the events of May 8, 1998 and August 28, 1999, was determined by the generation of ballooning and radial oscillations in coronal loops. Using our technique, we have estimated the flare plasma parameters whose values are consistent with the independent diagnostics based on GOES X-ray observations.

ACKNOWLEDGMENTS

REFERENCES

1. A. Asai, M. Shimojo, H. Isobe, *et al.*, Astrophys. J. **562**, L103 (2001).
2. M. J. Aschwanden, Solar Phys. **111**, 113 (1987).
3. M. J. Aschwanden, *NATO Advanced Research Workshops,* NATO Sci. Ser. II, Ed. by R. von Fay Siebenburgen, K. Petrovy, B. Roberts, and M. J. Aschwanden (Kluwer Acad., Dordrecht, 2003), p. 22.
4. M. J. Ashwanden, L. Fletcher, C. J. Schrijver, *et al.*, Astrophys. J. **520**, 880 (1999).
5. T. S. Bastian, in *Proceedings of the Nobeyama Symp. NRO No. 479,* Ed. by T. Bastian, N. Gopalswamy, and K. Shibasaki (Nobeyama Radio Obs., Nagano, 1998), p. 211.
6. S. I. Braginskiĭ, Vopr. Teor. Plazmy **1**, 183 (1963).
7. O. S. Burdo, O. K. Cheremnykh, and O. P. Verkhoglyadova, Izv. Ross. Akad. Nauk, Ser. Fiz. **64**, 1896 (2000).
8. G. A. Doschek, in *Proceedings of the Kofu Symp. NRO No. 360,* Ed. by S. Enome and T. Hirayama (Nobeyama Radio Obs., Nagano, 1994), p. 173.
9. G. A. Dulk and K. A. Marsh, Astrophys. J. **259**, 350 (1982).
10. G. D. Fleishman and V. F. Melnikov, Astrophys. J. **587**, 823 (2003).
11. Yu. G. Kopylova and A. V. Stepanov, Izv. Glavn. Astron. Obs. **216**, 555 (2002).
12. Yu. G. Kopylova, A. V. Stepanov, and Yu. T. Tsap, Pis'ma Astron. Zh. **28**, 870 (2002).
13. J. Lee, D. E. Gary, J. Qiu, *et al.*, Astrophys. J. **572**, 609 (2002).
14. M. Mathioudacis, J. H. Seiradakis, D. R. Williams, *et al.*, Astron. Astrophys. **403**, 1101 (2003).
15. B. I. Meerson, P. V. Sasorov, and A. V. Stepanov, Solar Phys. **58**, 165 (1978).
16. F. Meyer, H. U. Schmidt, and N. O. Weiss, Mon. Not. R. Astron. Soc. **179**, 741 (1977).
17. A. B. Mikhaĭlovskiĭ, *Theory of Plasma Instabilities* (Consultants Bureau, New York, 1974; Atomizdat, Moscow, 1971), Vol. 2.
18. H. Nakajima, K. Shibasaki, T. Yokoyama, *et al.*, *Nobeyama Radioheliograph Catalog of Events No. 3* (Nobeyama Radio Obs., Nagano, 2002).
19. V. M. Nakariakov, V. F. Melnikov, and V. E. Reznikova, Astron. Astrophys. **412**, L7 (2003).
20. V. M. Nakariakov and L. Ofman, Astron. Astrophys. **372**, L53 (2001).
21. V. Petrosian, T. Q. Donaghy, and J. M. McTiernan, Astrophys. J. **569**, 459 (2002).
22. E. R. Priest, *Solar Magnetohydrodynamics* (Reidel, Dordrecht, 1982; Mir, Moscow, 1985).
23. L. A. Pustil'nik, Astron. Zh. **50**, 1211 (1973) [Sov. Astron. **17**, 763 (1973)].
24. Z. Qin, C. Li, Q. Fu, and Z. Gao, Solar Phys. **163**, 383 (1996).
25. B. Roberts, *Solar System Magnetic Fields,* Ed. by E. R. Priest (Nobeyama Radio Obs., Nagano, 1986), p. 37.
26. H. Rosenberg, Astron. Astrophys. **9**, 159 (1970).
27. J. Sato, M. Sawa, S. Masuda, *et al.*, *The Yohkoh HXT Image Catalogue. October 1991−August 1998* (Nobeyama Radio Obs., Nagano, 1998).
28. K. Shibasaki, in *Proceedings of the Nobeyama Symp. NRO No. 479,* Ed. by T. Bastian, N. Gopalswamy, and K. Shibasaki (Nobeyama Radio Obs., Nagano, 1998), p. 419.
29. K. Shibasaki, Astrophys. J. **557**, 326 (2001).
30. A. V. Stepanov and Y. T. Tsap, Solar Phys. **211**, 135 (2002).
31. R. J. Thomas, R. Starr, and C. J. Crannell, Solar Phys. **95**, 323 (1985).
32. Y. T. Tsap, Solar Phys. **194**, 131 (2000).
33. Yu. T. Tsap and Yu. G. Kopylova, in *Proceedings of the International Seminar on Solar and Stellar Physics*, Ed. by B. B. Mikhalyaev, V. V. Mustsevoĭ, and A. A. Solov'ev (Kalmyk. Gos. Univ., Elista, 2003), p. 123.
34. V. V. Vityazev, *Wavelet Analysis of Time Series* (St. Peterburg. Gos. Univ., 2001).
35. T. F. Volkov, Vopr. Teor. Plazmy **4**, 3 (1964).
36. T. Yokoyama, H. Nakajima, K. Shibasaki, *et al.*, Astrophys. J. **576**, L87 (2002).
37. V. V. Zaĭtsev and A. V. Stepanov, Pis'ma Astron. Zh. **8**, 248 (1982) [Sov. Astron. Lett. **8**, 132 (1982)].
38. V. V. Zaĭtsev and A. V. Stepanov, Pis'ma Astron. Zh. **15**, 154 (1989) [Sov. Astron. Lett. **15**, 66 (1989)].
39. V. V. Zaĭtsev and A. V. Stepanov, Issled. Geomagn. Aéron. Fiz. Solntsa **37**, 3 (1975).

Translated by V. Astakhov

Variations of Microwave Emission from Solar Active Regions

G. B. Gelfreikh[1], Yu. T. Tsap[2*], Yu. G. Kopylova[1],
T. B. Goldvarg[3], Yu. A. Nagovitsyn[1], and L. I. Tsvetkov[2]

[1] *Pulkovo Astronomical Observatory, Russian Academy of Sciences, Pulkovskoe shosse 65, St. Petersburg,*
196140 Russia
[2] *Crimean Astrophysical Observatory, p/o Nauchnyi, Crimea, 334413 Ukraine*
[3] *Kalmyk State University, Elista, Russia*
Received October 17, 2003

Abstract—Based on observational data obtained with the RT-22 Crimean Astrophysical Observatory radio telescope at frequencies of 8.6 and 15.4 GHz, we investigate the quasi-periodic variations of microwave emission from solar active regions with periods $T_{\mathrm{p}} < 10$ min. As follows from our wavelet analysis, the oscillations with periods of 3−5 min and 10−40 s have the largest amplitudes in the dynamic power spectra, while there are virtually no oscillations with $T_{\mathrm{p}} < 10$ s. Our analysis shows that acoustic modes with $T_{\mathrm{p}} \lesssim 1$ min strongly dissipate in the lower solar corona due to thermal conduction losses. The oscillations with $T_{\mathrm{p}} = 10−40$ s are associated with Alfvén disturbances. We analyze the influence of acoustic and Alfvén oscillations on the thermal mechanisms of microwave emission in terms of the homogeneous model. We discuss the probable coronal heating sources. © *2004 MAIK "Nauka/Interperiodica".*

Key words: *Sun, active regions, microwave emission, MHD waves, corona.*

INTRODUCTION

With the launch of the SOHO (1995) and TRACE (1998) satellites, a new direction of astrophysical research called coronal seismology (Roberts 2000; Poedts 2002) has developed rapidly. Such a great interest is primarily associated with the solution of the problem of solar coronal heating by magnetohydrodynamic (MHD) waves and with the possibility of a further improvement in the methods for diagnosing the magnetic fields in the upper solar atmosphere (see, e.g., Nakariakov and Ofman 2001).

At present, two mechanisms are generally invoked to account for the high temperature of the solar corona (Priest *et al.* 2002). According to the first of these, the MHD waves generated by convective motions in the photosphere are responsible for its heating. According to the second mechanism, the corona heats up through the reconnection of magnetic field lines accompanied by microflares. In our opinion, the wave approach appears more attractive, because the formation of small-scale current sheets in the solar corona through the twisting of magnetic field lines caused by photospheric motions (Parker 1988) seems problematic. In addition, as estimates indicate (Hudson 1991), the energy of microflares is evidently

insufficient to provide the high temperature of the coronal plasma.

Optical, ultraviolet, and X-ray observations of waves and oscillations in the upper solar atmosphere have a number of significant shortcomings. In particular, the typical signal accumulation and readout time on the SOHO and TRACE instruments is several tens of seconds, which severely limits the possibilities for investigating MHD waves with short periods ($\lesssim 1$ min). The latter most likely determine the high temperature of the solar corona (see, e.g., Priest 1982). Such observations can provide only scanty information about the magnetic field strengths in the upper solar atmosphere. Meanwhile, the gyroresonance microwave emission from active regions is highly sensitive to magnetic field variations, and the time resolution of currently available radio telescopes reaches several milliseconds. Therefore, a study of the various manifestations of MHD disturbances in the upper solar atmosphere at radio frequencies is of particular value.

The most detailed observations of microwave pulsations from active regions, although with a low time resolution of about 10 s, were performed with the VLA and Nobeyama radio interferometers (Gelfreikh *et al.* 1999; Shibasaki 2001; Nindos *et al.* 2002). A Fourier analysis revealed that the most prominent oscillations above sunspots were those with

---

*E-mail: `yur@crao.crimea.ua`

a period $T_p \approx 3$ min. This result is in satisfactory agreement with optical and ultraviolet observations (Staude 1999; Brynildsen *et al.* 1999). At the same time, the microwave oscillations had a large spread (1−20%) in modulation depth (Shibasaki 2001; Nindos *et al.* 2002).

Gelfreikh *et al.* (1999) (see also Nindos *et al.* 2002; Hildebrandt and Staude 2002) assumed the radio pulsations with $T_p \approx 3$ min to be associated with oscillations of the height of the base of the transition region; i.e., the modulation depth of the gyroresonance emission is determined by the increase in temperature and the change in magnetic field with height. In this case, the effects due to the modulation of the plasma density and temperature by acoustic waves were disregarded. According to numerical calculations, the displacement amplitude of the transition region above sunspots is 25−50 km. However, the typical gyroresonance layer thicknesses do not exceed several hundred kilometers even in the corona (Alissandrakis *et al.* 1980). Therefore, this approach may be considered justified if emitting layers with an optical depth $\tau \lesssim 1$ are located at the level of the transition region. Otherwise, variations in the height of the base of the transition region will not lead to an appreciable modulation of the gyrosynchrotron emission, and it will be determined by density and temperature fluctuations (see also Shibasaki 2001).

Here, we investigate the quasi-periodic variations of microwave emission from solar active regions. In the next two sections, we outline the observing technique and describe the procedure for analyzing the observational data from the RT-22 Crimean Astrophysical Observatory (CrAO) radio telescope by using wavelet methods. Subsequently, we consider the dissipative processes associated with acoustic and Alfvén modes. Particular attention is paid to the problem of solar coronal heating. We then analyze the influence of MHD disturbances on the modulation of thermal microwave emission from active regions. In conclusion, we present and discuss our main results.

THE OBSERVING TECHNIQUE

In September 2001, observations of the sun were performed using an RT-22-based diagnostic complex at two wavelengths, 2.0 cm (15.4 GHz) and 3.5 cm (8.6 GHz), with a spatial resolution of $3\rlap{.}'6$ and $6\rlap{.}'0$, respectively. The polarimeter was able to record the Stokes parameters I and $V = I_R - I_L$, where I_R and I_L are the intensities of the microwave emission components with right-hand (R) and left-hand (L) circular polarizations. The sensitivity of the radio telescope was 0.1 s.f.u (1 s.f.u. $= 10^{-22}$ W m^{-2} Hz^{-1}). The RT-22 control, data acquisition and processing system (Baranov *et al.* 1998) recorded signals by their

sequential transformation for each of the four low-frequency channels fed to an ADC through an analog switching unit with a switching frequency of 100 GHz and a signal accumulation time of 1 s. The averaged data were written to magnetic media.

The process of observations consisted in scanning the solar disk in right ascension with a $2'$ declination step, pointing the antenna based on the radio emission peak of the local source at the shortest wavelength, and tracking the selected active region. The object to be observed was chosen by estimating prognostic parameters for each of the sources detected on the solar disk by using both scanning data and data accessible via the Internet (e.g., http://www.bbso.njit.edu). The same active region, NOAA 9628, was observed from September 17 through 24, which allowed us to obtain continuous (up to 8 h) series of intensity and polarization observations with a time resolution of 1 s over a fairly long period. The conversion to solar flux units (s.f.u.) and the transformation of temporal data to a uniform grid were made using a program developed by A.V. Melnikov (Pulkovo Astronomical Observatory, Russian Academy of Sciences), which included normalization and allowance for spurious signals.

OBSERVATIONAL DATA ANALYSIS

Since the time series being studied might be expected to contain quasi-periodic pulsations of distinctly different scales and to have appreciable deviations from strict periodicity (the pulsation amplitude and period vary with time, the oscillations are in the form of trains), a Fourier analysis can lead to incorrect conclusions (Vityazev 2001). Therefore, we analyzed the RT-22 observational data by using the wavelet transform whose basis was formed from well-localized (in frequency and time) wavelet functions. This transform allowed us not only to construct a signal spectrum similar to that yielded by a Fourier analysis, but also to trace the variations in its main characteristics.

To analyze the time series, we chose the Morlet wavelet which is a harmonic oscillation modulated by a Gaussian:

$$\psi(t) = \exp(-t^2/\alpha_0^2)[\exp(i\omega_0 t) - \exp(-\omega_0{}^2\alpha_0^2/4)].$$

The form of this function (the system of maxima and minima that approach zero outside a short time interval) determines one of its advantages— it is well adaptable to a time−frequency analysis, which is important for an accurate determination of short periods. When choosing the coefficients $\alpha_0^2 = 2$ and $\omega_0 = 2\pi$, the basis wavelet function $\psi(t) = \exp(-t^2/2)\exp(i2\pi t)$ makes it possible to interpret the wavelet spectra in terms of the traditional Fourier

decomposition and to measure the oscillation amplitude and period directly on the plot of the spectrum.

Based on $\psi(t)$, we constructed an integral wavelet transform of the sequence being studied:

$$W_\psi(a,b) = \frac{1}{\sqrt{a}} \int\limits_{-\infty}^{+\infty} f(t)\psi^* \left(\frac{t-b}{a} \right) dt,$$

where the superscript $*$ denotes complex conjugation, and the scale factor $a = 2^q$ ($q = 1, 2, \ldots, N_q$) acts as the oscillation period in the Fourier spectrum and determines the extension of the basis wavelet. The parameter N_q was chosen in such a way that 2^{N_q} did not exceed the number of elements in the original sequence. Using the shift parameter $b = 1, 2, \ldots, N_b$, we specified the time localization of $\psi(t)$.

When applying the wavelet transform, we found a correlation between the series $f(t)$ being analyzed and the chosen wavelet $\psi(t)$, which was extended and shifted in realization length. As a result, a two-dimensional array of coefficients $W_\psi(a, b)$ was formed; from this array, we calculated the amplitude of the dynamic spectrum

$$A = \sqrt{8/(\pi N_b)[(\mathrm{Re}W_\psi)^2 + (\mathrm{Im}W_\psi)^2]}.$$

The significance level was taken to be 0.9 and was found as follows:

$$P(T_\mathrm{p}) = 1 - (1 - C^2(T_\mathrm{p}))^{N_b/2-1},$$

where $C(T_\mathrm{p})$ is the coefficient of multiple linear correlation between the time series $f(t)$ being studied and the wavelet $\psi(t)$.

Figure 1 shows a typical example of the local microwave pulsation spectrum for the active region obtained in the time interval 05:25−06:05 UT for quasiperiodic oscillations with $T_\mathrm{p} < 10$ min whose modulation depth generally did not exceed 3%. We see from this figure that the oscillations with the well-known periods of $\sim$180 and 300 s have the largest amplitudes. We also distinguish harmonics of 3-min oscillations with $T_\mathrm{p} = 60-100$ s and short-period oscillations with $T_\mathrm{p} = 10-40$ s, whereas no pulsations with $T_\mathrm{p} < 10$ s manifested themselves in any realization.

We also used wavelet methods to investigate the variations of oscillation periods with time. As follows from Fig. 2, which is based on polarization measurements, quasiperiodic MHD disturbances are generated in the solar atmosphere in the form of short trains that reflect the peculiarities of the wave generation and propagation. A detailed analysis of all our observational series for the active region NOAA 9628 shows that, on average, the oscillation Q-factor is

$Q = \pi t_e/T_\mathrm{p} \lesssim 7-8$, where t_e is the characteristic time during which the oscillation amplitude decreases by a factor of e.

We performed a correlation analysis of the time series for the polarized and nonpolarized emissions. In general, the correlation coefficients were found to be no larger than 0.5. This can be easily explained by the low spatial resolution of the telescope and by the inhomogeneity of the active region (the oscillations of individual structures in the active region with different degrees of polarization and periods are added and averaged). At the same time, the peaks in the dynamic spectra of the polarized emission proved to be more prominent.

DISSIPATION OF ACOUSTIC AND ALFVÉN WAVES

Let us consider the dissipation mechanisms of the acoustic waves that are similar in properties to the slow MHD modes generated in magnetic flux tubes.

The thermal energies released due to ion viscosity, E_v, and electron thermal conduction, E_c, as well as the radiative losses E_r after averaging over the oscillation period can be represented as follows (Gordon and Hollweg 1983; Priest 1982):

$$E_\mathrm{v} = \frac{\eta_0}{6}(\nabla\delta\mathbf{v})^2, \quad \eta_0 = 0.96nk_\mathrm{B}T\tau_i; \qquad (1)$$

$$E_\mathrm{c} = \frac{\kappa_\parallel}{2}\left(\frac{k}{\omega}\right)^2 k_\mathrm{B}T(\gamma-1)^2(\nabla\delta\mathbf{v})^2,$$

$$\kappa_\parallel = 3.16\frac{nk_\mathrm{B}T\tau_e}{m};$$

$$E_\mathrm{r} = \frac{(3-\gamma)(5-\gamma)}{16}\frac{n^2R(T)}{\omega^2}(\nabla\delta\mathbf{v})^2,$$

$$R(T) = \frac{5\times10^{-20}}{\sqrt{T}}.$$

Here, the standard notation is used, and the characteristic ion and electron collision times τ_i and τ_e are related by (Braginskiĭ 1963)

$$\tau_i = \sqrt{\frac{2M}{m}}\tau_e \approx 17\frac{T^{3/2}}{n\Lambda}\ \mathrm{s}, \qquad (2)$$

where M and m are the proton and electron masses, respectively; and $\Lambda = 25.3 - 1.15\log n + 2.3\log T$ is the Coulomb logarithm in which the temperature is given in eV. Note that the dependence of the radiative loss function $R(T)$ on temperature T adopted in (1) corresponds to the temperature range $T = 10^6-10^{7.6}$ K for an optically thin source (Priest 1982).

We write the damping decrement $\nu < \omega$ as
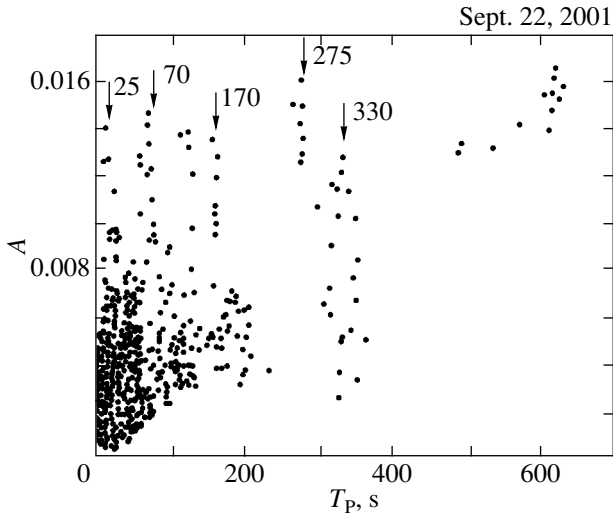
$$\nu = \frac{E}{2W}. \qquad (3)$$

Sept. 22, 2001

Fig. 1. Example of the local microwave pulsation spectrum for the polarized (8.6 GHz) emission from the active region NOAA 9628 obtained in the time interval 05:25–06:05 UT. The amplitude A is given in arbitrary units.
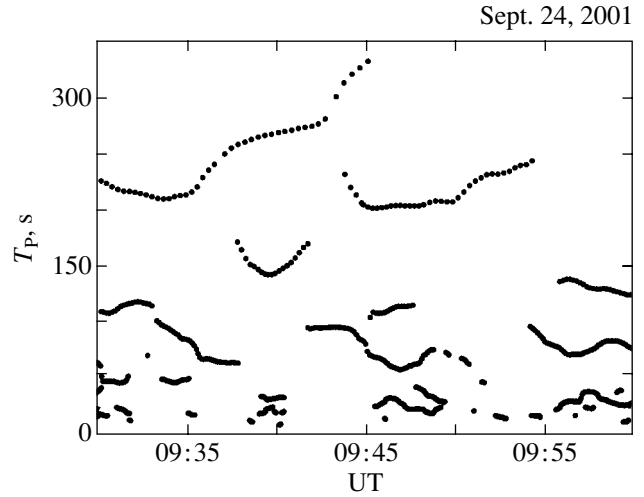
Sept. 24, 2001

Fig. 2. Example of the variations of oscillation periods with $T_p < 350$ s for the polarized (8.6 GHz) emission from the active region NOAA 9628.

Here, W is the period-averaged energy density of the waves. For acoustic waves at low values of the plasma parameter $\beta \approx c_s^2/v_A^2 \ll 1$, where $c_s = \sqrt{\gamma k_B T/M}$ and $v_A = B/\sqrt{4\pi n M}$ are the speed of sound and the Alfvén speed, respectively, the latter can be represented as (Braginskiĭ 1963)

$$W = c_s^2 \frac{\delta\rho^2}{2\rho}, \qquad (4)$$

where ρ is the plasma density. Using the linearized continuity equation

$$-i\omega\delta\rho + \rho\nabla\delta\mathbf{v} = 0$$

and substituting (1), (2), and (4) in (3), we find for the damping decrements attributable to ion viscosity, electron thermal conduction, and radiative losses that

$$\nu_v \approx 0.1\omega^2 \frac{T^{3/2}}{n}, \quad \nu_c \approx 10\omega^2 \frac{T^{3/2}}{n}, \qquad (5)$$

$$\nu_r \approx 5 \times 10^{-5} \frac{n}{T^{3/2}}.$$

The latter equations suggest that the dissipation of acoustic oscillations in the lower corona is governed by electron thermal conduction; i.e., the damping decrement is $\nu_\Sigma = \nu_v + \nu_c + \nu_r \approx \nu_c$. Since the period is $T_p = 2\pi/\omega$, we then derive from (5)

$$\frac{\nu_\Sigma}{\omega} \approx 63 \frac{T^{3/2}}{nT_p}. \qquad (6)$$

Assuming the temperature and density in (6) to be $T = 10^6$ K and $n = 10^9$–10^{10} cm^{-3}, respectively, we obtain $\nu_\Sigma/\omega \approx 63 \times (0.1$–$1)/T_p$. Therefore, acoustic

oscillations with $T_p \lesssim 1$ min are subject to strong dissipation. In this case, their amplitude decreases by a factor of e in time $t_e = 1/\nu_\Sigma \approx 2.5 \times (10^{-3}$–$10^{-2})T_p^2$, which is 0.15–1.5 min for $T_p = 60$ s. This conclusion is in good agreement with both SOHO and TRACE observations (Ireland *et al.* 1999; De Moortel *et al.* 2000) and with numerical simulations (De Moortel *et al.* 2000; Nakariakov *et al.* 2000; Tsiklauri and Nakariakov 2001).

Since Alfvén disturbances, in contrast to acoustic waves, do not compress the plasma, they are subject to dissipative processes to the smallest degree among the MHD modes in the solar atmosphere. If, however, their periods are less than several tens of seconds, then these waves will be strongly damped in the chromosphere as they propagate from the photosphere into the corona due to the large energy losses caused by collisions between ions and neutrals (De Pontieu *et al.* 2001). In this case, the generation of Alfvén waves with $T_p > 10$ s in the upper solar chromosphere seems problematic. Indeed, one might expect the generation of these modes by a source with scale sizes H to be effective only if the length of the emitted wave is $\lambda = v_A T_p \lesssim H$. For $v_A = 3 \times 10^7$ cm s^{-1} and $T_p = 20$ s, we then obtain $H \gtrsim 6 \times 10^8$ cm, which is much larger than the thickness of the upper chromosphere. Thus, Alfvén disturbances may be assumed to be responsible for the detected microwave oscillations with short periods ($T_p = 10$–40 s); it is these disturbances that determine the high temperature of the coronal plasma. Therefore, let us make some estimates.

The energy flux of Alfvén waves can be represented as

$$F = \frac{\rho \delta v^2}{2} v_{\mathrm{A}}. \tag{7}$$

Assuming that $\rho = 10^{-15}-10^{-14}$ g cm^{-3}, $v_{\mathrm{A}} = 10^8$ cm s^{-1}, and $\delta v = 10^7$ cm s^{-1} in the lower corona, we obtain $F = 0.5 \times (10^7-10^8)$ erg cm^{-2} s^{-1} from (7) (according to De Moortel *et al.* (2000), $F \approx 4 \times 10^2$ erg cm^{-2} s^{-1} for acoustic waves). Thus, since the fluxes of 3×10^5 and 10^7 erg cm^{-2} s^{-1} (Porter *et al.* 1994) are required for quiet and active regions, respectively, in contrast to acoustic modes, Alfvén waves may well heat the coronal plasma.

In the case of phase mixing, the dissipation scale length for Alfvén waves (Heyvaerts and Priest 1983; Roberts 2000) is

$$d = v_{\mathrm{A}} \left(\frac{3l^2 T_{\mathrm{p}}^2}{2\pi^2 \eta} \right)^{1/3}, \tag{8}$$

where l is the characteristic scale of change in Alfvén speed v_{A}, and η is the kinematic viscosity. Taking $v_{\mathrm{A}} = 10^8$ cm s^{-1}, $l = 3 \times 10^8$ cm, $T_{\mathrm{p}} = 20$ s, and $\eta = 4 \times 10^{13}$ cm^2 s^{-1}, we obtain $d \approx 5.2 \times 10^9$ cm from (8). This value is comparable to the loop length and suggests that the wave energy can be effectively transferred to the coronal plasma. If resonance oscillations are generated in the loop, their Q-factor is

$$Q = \left(\frac{3\pi l^2}{2\eta T_{\mathrm{p}}} \right)^{1/3} \approx 8. \tag{9}$$

This estimate is in satisfactory agreement with microwave observations. Note also that, since $T_{\mathrm{p}} = 2L/v_{\mathrm{A}}$ for the fundamental mode, Eq. (9) suggests a weak dependence of the oscillation Q on the magnetic field B and the loop length L.

MODULATION OF MICROWAVE EMISSION

Let us consider the influence of acoustic and Alfvén disturbances on the modulation of thermal microwave emission from active regions in terms of the homogeneous model.

We define the modulation depth as

$$M = \frac{\delta I(x)}{I(x)}, \tag{10}$$

where $\delta I(x) = I(x + \delta x) - I(x)$ is the change in intensity caused by a disturbance with an amplitude $\delta x \ll x$.

Acoustic Modes

For optically thick sources,

$$I_1 \propto T, \tag{11}$$

whereas for optically thin sources, which can also contribute significantly to the microwave emission from active regions (Hildebrandt and Staude 2002; Alissandrakis *et al.* 1980; White and Kundu 1997) when the bremsstrahlung or magnetobremsstrahlung radiation mechanisms are at work (Zheleznyakov 1977),

$$I_2 \propto \begin{cases} n^2/\sqrt{T} & (\text{ bremsstrahlung}) \\ nT^s & (\text{ magnetobremsstrahlung}), \end{cases} \tag{12}$$

where $s \geq 2$ is the cyclotron harmonic number.

We assume that the variations in density, δn, and temperature, δT, caused by small acoustic disturbances are adiabatic: $n^{3/2}/T = $ const. We then obtain from (10)–(12)

$$M_1 = \delta T/T,$$

$$M_2 = \begin{cases} (5/6)\delta T/T & (\text{ bremsstrahlung}) \\ (s + 2/3)\delta T/T & (\text{ magnetobremsstrahlung}). \end{cases} \tag{13}$$

According to (13), the modulation depth M for the bremsstrahlung mechanism does not vary significantly with optical depth τ. At the same time, for magnetobremsstrahlung, its value depends markedly on τ and increases with harmonic number s for an optically thin source. If it is also considered that the gyroresonance layers with $s \leq 4$ make a dominant contribution to the microwave emission from solar active regions (see, e.g., Alissandrakis *et al.* 1980), then, other things being equal, M can increase only severalfold when passing from an optically thick source to an optically thin one.

Alfvén Modes

Disturbances of this type do not compress the plasma, but only change the direction of the magnetic field. Therefore, they will not modulate the emission from an optically thick source in the approximation under consideration. In addition, since τ for the bremsstrahlung mechanism depends relatively weakly on the angle α between the magnetic-field direction and the wave vector, we restrict our analysis below to the influence of Alfvén disturbances on the modulation of optically thin gyroresonance emission.

The optical depth for harmonics with $s \geq 2$ in the quasilongitudinal approximation is (Zheleznyakov 1964)

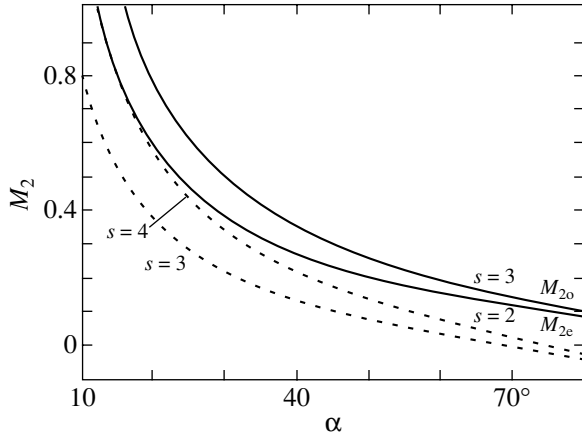$$\tau \propto \sin^{2s-2} \alpha (1 \pm \cos \alpha)^2,$$

Fig. 3. Modulation depth M_2 of an optically thin source versus angle α between the magnetic-field direction and the wave vector of the ordinary (o) and extraordinary (e) waves ($\delta\alpha = 2°$).

where the upper and lower signs correspond to the extraordinary (e) and ordinary (o) waves, respectively. Since $I \propto \tau$, according to (10), the modulation depth is

$$M_{2e} = \{(2s - 2)\cot\alpha - 2\tan(\alpha/2)\}\delta\alpha, \quad (14)$$

$$M_{2o} = \{(2s - 2)\cot\alpha + 2\cot(\alpha/2)\}\delta\alpha. \quad (15)$$

We emphasize that M_{2e} is an alternating quantity. Thus, taking $s = 3$ in (14), it is easy to show that M_{2e} is negative starting from $\alpha = \arccos(1/3) \approx 70°$.

The functions $M_{2e}(\alpha)$ for $s = 3, 4$ and $M_{2o}(\alpha)$ for $s = 2, 3$ are plotted in Fig. 3. This figure shows that the modulation depths can reach large values; they increase with increasing harmonic number s and decrease with increasing angle α. Notice that the modulation of the ordinary wave is more effective than that of the extraordinary wave. As applied to observations, this suggests that, if the variations in Stokes parameters I and V are caused by Alfvén disturbances, they can be both in phase and in antiphase. Indeed, for a source located in a region with positive polarity, the perturbation amplitude of the Stokes parameter $\delta V = \delta I_R - \delta I_L$ may prove to be negative, although waves with right-hand circular polarization ($I_R > I_L$) dominate in the emission.

DISCUSSION AND CONCLUSIONS

Based on the observational data obtained with the RT-22 CrAO radio telescope in September 2001, we analyzed the microwave pulsations from active solar regions. Using a wavelet analysis to search for periodicities with $T_p < 10$ min, we revealed the following.

(1) The oscillations with periods $T_p = 3-5$ min and $T_p = 10-40$ s have the largest amplitude in the dynamic power spectra.

(2) The oscillations (waves) have the shape of low-Q trains (on average, $Q \lesssim 7-8$).

(3) No second ($T_p < 10$ s) oscillations were found in any realization.

We emphasize that microwave oscillations from active regions with $T_p < 1$ min were previously detected by Zandanov *et al.* (1984) using the Siberian Solar Radio Telescope (SSRT).

It follows from TRACE observations that the intensity oscillation periods at the footpoints of coronal loops depend on the location of the latter in the active region (De Moortel *et al.* 2002). Thus, for example, 3-min oscillations dominate above magnetic spots, while 5-min oscillations dominate in other regions. As follows from microwave observations, the oscillations with $T_p \approx 5$ min have large amplitudes, thereby indicating that radio sources outside sunspots contribute significantly to the modulation of emission from active regions. We consider the oscillations with periods of $1-2$ min as harmonics of the oscillations with $T_p = 3-5$ min. Note, therefore, that owing to TRACE observations, King *et al.* (2003) have recently managed to reveal harmonics of the 5-min oscillations in coronal loops.

Here, we have shown that acoustic modes with periods $T_p < 1$ min strongly dissipate in the lower solar corona due to thermal conduction losses. In our view, this is one of the reasons why these modes have not yet been detected on the TRACE and SOHO satellites. This circumstance and the absence of oscillations with $T_p < 10$ s in the power spectrum suggest that the short-period ($T_p = 10-40$ s) oscillations are produced by Alfvén waves. This conclusion is consistent with the results by De Pontieu *et al.* (2001) according to which Alfvén modes with periods shorter than several tens of seconds strongly dissipate in the solar chromosphere as they propagate from the photosphere into the corona. The possibility that the Alfvén waves with $T_p = 10-40$ s are generated directly in the upper solar chromosphere through the reconnection of magnetic field lines or the nonlinear interaction with acoustic waves whose spectrum is at a maximum in the range $3-5$ min also seems unlikely.

In our opinion, Alfvén waves with $T_p \gtrsim 10$ s may be responsible for the heating of the solar corona. Being generated by small-scale convective motions, they are capable of effectively transferring the coronal plasma energy by the phase mixing mechanism. Whether second oscillations exist in active regions is still an open question (Rudawy *et al.* 2002). The MHD pulsations with $T_p \ll 10$ s can be generated only through flare-driven energy release (Aschwanden 2001).

As follows from the homogeneous model, the modulation efficiency of thermal magnetobrems-

strahlung by acoustic modes depends significantly on the optical depth, the variations of which can make an appreciable contribution to the observed spread in microwave modulation depths detected with Nobeyama and VLA. Nevertheless, the observed values, which can reach 20%, cannot be explained in terms of the homogeneous model. Therefore, when the modulation mechanisms associated with MHD oscillations are considered, the temperature and magnetic-field nonuniformities in the upper solar atmosphere should be taken into account.

Our results suggest that Alfvén disturbances for an optically thin source can lead to large fluctuations of gyroresonance emission. Since the modulation efficiency for ordinary waves is appreciably higher than that for extraordinary waves, the variations in Stokes parameters I and V can be both in phase and in antiphase.

ACKNOWLEDGMENTS

REFERENCES

1. C. E. Alissandrakis, M. R. Kundu, and P. Lantos, Astron. Astrophys. **82**, 30 (1980).
2. M. J. Aschwanden, Astrophys. J. **560**, 1035 (2001).
3. N. V. Baranov, M. A. Mironov, P. S. Nikitin, and L. I. Tsvetkov, Kinemat. Fiz. Neb. Tel **14**, 89 (1998).
4. S. I. Braginskiĭ, Vopr. Teor. Plazmy **1**, 183 (1963).
5. N. Brynildsen, D. Kjeldseth-Moe, and P. Maltby, Astrophys. J. **517**, 159 (1999).
6. G. B. Gelfreikh, V. Grechnev, T. Kosugi, and K. Shibasaki, Solar Phys. **185**, 177 (1999).
7. B. E. Gordon and J. V. Hollweg, Astrophys. J. **266**, 373 (1983).
8. J. Heyvaerts and E. R. Priest, Astron. Astrophys. **117**, 220 (1983).
9. J. Hildebrandt and J. Staude, *Poster Proceedings of the 1st Potsdam Thinkshop on Sunspots and Starspots,* Ed. by K. G. Strassmeier and A. Washuettl (Astrophys. Inst. Potsdam, 2002), p. 95.
10. H. S. Hudson, Solar Phys. **133**, 357 (1991).
11. J. Ireland, R. W. Walsh, R. A. Harrison, and E. R. Priest, Astron. Astrophys. **347**, 355 (1999).
12. D. B. King, V. M. Nakariakov, E. E. Deluca, *et al.*, Astron. Astrophys. **404**, L1 (2003).
13. I. De Moortel, J. Ireland, and R. W. Walsh, Astron. Astrophys. **355**, L23 (2000).
14. I. De Moortel, J. Ireland, A. W. Hood, and R. W. Walsh, Astron. Astrophys. **387**, L13 (2002).
15. V. M. Nakariakov and L. Ofman, Astron. Astrophys. **372**, L53 (2001).
16. V. M. Nakariakov, E. Verwichte, D. Berghmans, and E. Robbrecht, Astron. Astrophys. **362**, 1151 (2000).
17. A. Nindos, C. E. Alissandrakis, G. B. Gelfreikh, *et al.*, Astron. Astrophys. **386**, 658 (2002).
18. E. N. Parker, Astrophys. J. **330**, 474 (1988).
19. S. Poedts, in *Proceedings of the SOLMAG: Magnetic Coupling of the Solar Atmosphere Euroconference IAU Coll. No. 188,* Ed. by H. Sawaya-Lacoste (ESA Publ. Div., Noordwijk, 2002), ESA SP-505, p. 273.
20. B. De Pontieu, P. C. Martens, and H. S. Hudson, Astrophys. J. **558**, 859 (2001).
21. L. J. Porter, A. Klimchuk, and P. A. Sturrock, Astrophys. J. **435**, 482 (1994).
22. E. R. Priest, *Solar Magnetohydrodynamics* (Reidel, Dordrecht, 1982; Mir, Moscow, 1985).
23. E. R. Priest, J. F. Heyvaerts, and A. M. Title, Astrophys. J. **576**, 533 (2002).
24. B. Roberts, Solar Phys. **193**, 139 (2000).
25. P. Rudawy, K. J. H. Phillips, P. Read, *et al.*, in *Proceedings of the 10th Europian Solar Physics Meeting,* Ed. by A. Wilson (ESA Publ. Div., Noordwijk, 2002), ESA SP-506, p. 967.
26. K. Shibasaki, Astrophys. J. **550**, 1113 (2001).
27. J. Staude, ASP Conf. Ser. **184**, 113 (1999).
28. D. Tsiklauri and V. M. Nakariakov, Astron. Astrophys. **379**, 1106 (2001).
29. V. V. Vityazev, *Wavelet Analysis of Time Series* (St. Petersburg Univ., St. Petersburg, 2001) [in Russian].
30. S. M. White and M. R. Kundu, Solar Phys. **174**, 53 (1997).
31. V. G. Zandanov, T. A. Treskov, and A. M. Uralov, Issled. Geomagn. Aeronomii Fiz. Solntsa **68**, 21 (1984).
32. V. V. Zheleznyakov, Izv. Vyssh. Uchebn. Zaved., Ser. Radiofiz. **7**, 67 (1964).
33. V. V. Zheleznyakov, *Electromagnetic Waves in Cosmic Plasma* (Nauka, Moscow, 1977) [in Russian].

Translated by V. Astakhov

A Theory of the Equilibrium Figure and Gravitational Field of the Galilean Satellite Io: The Second Approximation

V. N. Zharkov[*]

Schmidt Joint Institute of Physics of the Earth, Russian Academy of Sciences, ul. Bol'shaya Gruzinskaya 10, Moscow, 123810 Russia

Received February 16, 2004

Abstract—We construct a theory of the equilibrium figure and gravitational field of the Galilean satellite Io to within terms of the second order in the small parameter α. We show that to describe all effects of the second approximation, the equation for the figure of the satellite must contain not only the components of the second spherical function, but also the components of the third and fourth spherical functions. The contribution of the third spherical function is determined by the Love number of the third order h_3, whose model value is 1.6582. Measurements of the third-order gravitational moments could reveal the extent to which the hydrostatic equilibrium conditions are satisfied for Io. These conditions are $J_3 = C_{32} = 0$ and $C_{31}/C_{33} = -6$. We have calculated the corrections of the second order of smallness to the gravitational moments J_2 and C_{22}. We conclude that when modeling the internal structure of Io, it is better to use the observed value of k_2 than the moment of inertia derived from k_2. The corrections to the lengths of the semiaxes of the equilibrium figure of Io are all positive and equal to ~ 64.5, ~ 26, and ~ 14 m for the a, b, and c axes, respectively. Our theory allows the parameters of the figure and the fourth-order gravitational moments that differ from zero to be calculated. For the homogeneous model, their values are: $s_4 = \dfrac{885}{224}\alpha^2$, $s_{42} = -\dfrac{75}{224}\alpha^2$, $s_{44} = \dfrac{15}{896}\alpha^2$, $J_4 = -\dfrac{885}{224}\alpha^2$, $C_{42} = -\dfrac{75}{224}\alpha^2$, $C_{44} = \dfrac{15}{896}\alpha^2$. © *2004 MAIK "Nauka/Interperiodica"*.

Key words: *Solar system, Galilean satellites, internal structure models, equilibrium figures.*

INTRODUCTION

All the Galilean satellites are in synchronous rotation; their orbits are nearly circular and lie in the equatorial plane of Jupiter. Io is the large satellite closest to Jupiter. Therefore, the influence of Jupiter's tidal potential on the equilibrium figure and gravitational field of Io is appreciably stronger than it is on the remaining large satellites. For the theory of Io's figure to be consistent with currently available observational data, it must include effects of the second order of smallness.

If the Galilean satellites of Jupiter are in a state close to hydrostatic equilibrium, then data on their figures and gravitational fields allow us to impose a constraint on the density distribution in the interiors of these bodies and, thereby, to make progress in modeling their internal structure.

This problem was discussed by Hubbard and Anderson (1978) and Dermott (1979). In the former paper, the satellite model was represented as a heavy point mass (core) located at the center of a homogeneous envelope, while in the latter paper, a two-layer satellite model was studied. Formulas for the homogeneous model can be found in the well-known monograph by Jeffreys (1962). Zharkov *et al.* (1985) suggested a method that allowed the necessary relations to be derived for satellite models with an arbitrary density distribution. These relations are given below.

A remarkable achievement of the successful Galileo mission was the determination of the first coefficients in the expansion of the gravitational field in terms of spherical functions for the Galilean satellites and the proof that their figures are actually in hydrostatic equilibrium. The data for Io were so accurate that Anderson *et al.* (2001a) used the formulas obtained in the second approximation of the perturbation theory by Dermott and Thomas (1988) to describe the observational data; the latter authors used several assumptions in deriving the formulas of the second approximation. Here, we consider this question in a more consistent way. To understand the material presented below, we have to begin with a brief description of the general theory in the first approximation (Zharkov *et al.* 1985).

[*]E-mail: `Zharkov@uipe-ras.scgis.ru`

THE FIRST APPROXIMATION: A LINEAR THEORY

Let us introduce a spherical system of coordinates (r, θ, φ): r is the radius, θ is the colatitude (polar distance), and φ is the longitude. The tidal potential from Jupiter at the point of a satellite with coordinates (r, θ) has the standard form

$$W_t = \frac{GM}{R} \sum_{n=2}^{\infty} \left(\frac{r}{R}\right)^n P_n(\cos Z) = \sum_{n=2}^{\infty} W_n, \quad (1)$$

$$W_n = \frac{GMr^n}{R^{n+1}} P_n(\cos Z),$$

where G is the gravitational constant, M is the mass of Jupiter, Z is the angle between the radius vector of the interior point of the satellite under consideration and the direction of Jupiter's center of mass, $P_n(\cos Z)$ are the Legendre polynomials of degree n, and R is the radius of the satellite orbit, which is assumed to be circular. The equilibrium figure of the satellite is an equipotential surface of the sum of three potentials: the tidal potential W_t (1), the centrifugal potential

$$Q = \frac{\omega^2 r^2}{3} \left[1 - P_2(\cos \theta)\right], \quad (2)$$

and the potential from the mass distribution inside the satellite $V(r, \theta, \varphi)$, $U = W_t + Q + V = \text{const}$. In relation (2) ω is the angular velocity of the satellite around its axis, which is equal to the angular velocity of a synchronous satellite around the planet.

According to Kepler's third law, $\omega^2 = GM/R^3$ for synchronous satellites, and formula (2) takes the form

$$Q = \frac{GM}{3R} \left(\frac{r}{R}\right)^2 \left[1 - P_2(\cos \theta)\right]. \quad (3)$$

In deriving the equations of the figure theory (Zharkov and Trubitsyn 1975, 1980), we pass from the actual radius r to the effective radius s defined as the radius of a sphere of equivalent volume; i.e., we perform the transformation $(r, \theta, \varphi) \rightarrow (s, \theta, \varphi)$ which is discussed below in detail. The figure theory is constructed by expanding the expressions for the potentials in terms of the small parameter

$$\alpha = \frac{3\pi}{G\rho_0\tau^2} = \frac{\omega^2 s_1^3}{Gm_0} \quad (4)$$

$$= \left(\frac{M}{m_0}\right)\left(\frac{s_1}{R}\right)^3 = 171.37 \times 10^{-5},$$

where ρ_0, τ, m_0, and s_1 are the mean density, rotation period, mass, and mean radius of Io, respectively. The numerical value in (4) was obtained using data from table. In the first approximation, we may ignore the difference between r and s, which is of the order of α, and substitute s for r in W_t (1) and Q (2), (3). The

Observational data and model parameters for Io

Parameters	Io
Orbital radius R, 10^3 km	421.6
Period τ, days	1.769
s_1, km	1821.6 ± 0.5
m_0, 10^{23} g	893.2
ρ_0, g cm^{-3}	3.5278 ± 0.0029
g_0, cm s^{-2}	179
$\alpha = \dfrac{3\pi}{G\rho_0\tau^2}$, 10^{-5}	171.37
$\dfrac{C}{m_0 s_1^2}$	0.37685 ± 0.00035
J_2, 10^{-6}	1845.9 ± 4.2
C_{22}, 10^{-6}	553.7 ± 1.2
Jupiter's mass M, 10^{30} g	1.897

first term in (1), W_2 and Q (3) are determined by the same small parameter α. Therefore, in the first (linear) approximation, the combined effect from W_2 (1) and Q (3) is obtained by addition.

If the model of the satellite is known, i.e., if its density distribution is given and the satellite is close to hydrostatic equilibrium, then when its gravitational field and figure are calculated, it may be treated as an effectively liquid one and all of the sought parameters can be expressed in terms of the corresponding Love numbers. In this case, the quadrupole moment J_2 and the tesseral moment C_{22} as well as the semiaxes of the figure (a and b are the equatorial semiaxes directed toward the planet and along the orbital motion, respectively, and c is the polar semiaxis) can be calculated by adding up the individual responses of the satellite to the action of the first term of the tidal potential W_2 (1) and the centrifugal potential Q (3).

The Love numbers can be calculated by the method described by Gavrilov $et\ al.$ (1975), Gavrilov and Zharkov (1977), and Zharkov $et\ al.$ (1985). Let us introduce an auxiliary function $T(s)$ that is equal to the total perturbation of the satellite potential due to the action of W_2 (1) or Q (3):

$$V_i + W_k = \frac{1}{s_1 g_0} T \left(\frac{s_1}{s}\right)^n W_k, \quad (5)$$

$$k = t \text{ or } r, \quad W_r \equiv Q,$$

where n is the degree of the spherical function to which both W_2 (1) and Q (3) are directly proportional (in our case, $n = 2$), V_i is the perturbation of the satellite potential due to the action of W_2 (1) ($k = t$) or Q (3) ($k = r$), and g_0 is the gravitational acceleration on the surface of the satellite modeled by a sphere

of equivalent volume with radius s_1. The function $T(s)$ satisfies the ordinary differential equation of the second order

$$T'' + \frac{2}{s}T' + \left(4\pi G\frac{\rho'}{V'} - \frac{n(n+1)}{s^2}\right)T = 0, \quad (6)$$

where the prime denotes differentiation with respect to s. The function $T(s)$ must be finite at zero and satisfy the following boundary condition on the $s = s_1$ surface:

$$\left(T'\right)_{s_1-0} \qquad (7)$$
$$= -\frac{n+1}{s_1}(T)_{s_1-0} + 4\pi G\rho_{s_1}H_{s_1} + (2n+1)g_0.$$

The density distribution $\rho(s)$ in the satellite is assumed to be spherically symmetric, and, accordingly, the gravitational potential $V(s)$ depends only on the radius s.

The other function $H(s)$ that we encounter in the problem specifies the deformation and characterizes the radial displacement of the point under consideration

$$u_k = \frac{H(s)}{s_1 g_0}\left(\frac{s_1}{s}\right)^n W_k, \qquad (8)$$
$$k = t \text{ or } r, \quad W_r \equiv Q.$$

This function can be expressed in terms of T and V' using the formula

$$T + HV' = 0. \qquad (9)$$

The Love numbers of the nth order are determined by the values of $T(s)$ and $H(s)$ on the $s = s_1$ surface

$$h_n = \frac{H(s_1)}{s_1}, \quad k_n = \frac{T(s_1)}{s_1 g_0} - 1 \qquad (10)$$

(the subscript n of the functions $H(s)$ and $T(s)$ in Eqs. (5)–(8) was omitted). There is a simple relation between h_n and k_n:

$$h_n = 1 + k_n. \qquad (11)$$

Using the Legendre polynomial addition theorem and passing from the angle Z in W_2 (1) to Jupiter's angular coordinates (θ', φ') and to an arbitrary point of the satellite (θ, φ), we can easily obtain the sought-for relations (for details, see Zharkov et al. 1985):

$$J_2 = \frac{5}{6}\alpha k_2 = \frac{C - (A + B)/2}{m_0 s_1^2}, \qquad (12)$$

$$C_{22} = \frac{1}{4}\alpha k_2 = \frac{B - A}{4m_0 s_1^2}, \qquad (13)$$

where s_1 was chosen as the normalizing radius in the expansion of the equilibrium gravitational potential of Io in terms of spherical functions, and A, B, and C

are the equilibrium moments of inertia of Io relative to the a, b, and c axes, respectively. Adding up the effects from W_2 and Q in (8) yields an expression for the radial displacement of the satellite points:

$$u(s, \theta, \varphi) = u_0(s) + u_2(s, \theta, \varphi) \qquad (14)$$
$$= \frac{H_0(s)}{3s}\left(\frac{s}{s_1}\right)^2 \alpha s$$
$$+ \frac{H_2(s)}{s}\alpha s\left(-\frac{5}{6}P_2(t) + \frac{1}{4}P_2^2(t)\cos 2\varphi\right).$$

The geometrical figure of the satellite in the first approximation is given by formula (14), in which we should set $s = s_1$ and, according to (10), introduce the Love numbers h_0 and h_2:

$$u(s_1, \theta, \varphi) = \frac{1}{3}\alpha h_0 s_1 \qquad (15)$$
$$+ \alpha h_2 s_1\left(-\frac{5}{6}P_2(t) + \frac{1}{4}P_2^2(t)\cos 2\varphi\right).$$

In deriving (14) and (15), we assumed the following: the orbit of Io is circular, the angular coordinates of Jupiter are $\theta' = \pi/2$ and $\varphi' = 0$, the longitude φ is measured from the a axis directed along the line connecting the centers of the satellite and the planet, and $P_2^1(0) = 0$, $P_2^2(0) = 3$, $P_2(0) = -1/2$. The small expansion of the satellite given by the first term in (15) will not be included yet in the formulas for the increments of the semiaxes which are derived from (15) ($P_2(1) = 1$, $P_2^2(1) = 0$):

$$a = s_1 + \Delta a, \quad \Delta a = \frac{7}{6}\alpha h_2 s_1,$$
$$b = s_1 + \Delta b, \quad \Delta b = -\frac{1}{3}\alpha h_2 s_1, \qquad (16)$$
$$c = s_1 + \Delta c, \quad \Delta c = -\frac{5}{6}\alpha h_2 s_1.$$

In the first approximation, the theory yields simple formulas for the differences between the semiaxes:

$$a - c = 2\alpha h_2 s_1, \quad b - c = \frac{1}{4}(a - c). \qquad (17)$$

The same can also be said about the ratio of the moments J_2 (12) and C_{22}: (13)

$$J_2 = \frac{10}{3}C_{22}. \qquad (18)$$

In the theory of an equilibrium figure, there is dualism between the parameters of the figure (in our case, this is h_2 in (16) and k_2 in (12), (13)). If we have determined the semiaxes of the figure (16) and, hence, h_2, then we obtain k_2 using (11) and can calculate the moments J_2 and C_{22} using (12) and (13). The reverse is also true.

For the homogeneous model, $\rho(s) = \rho_0 = \text{const}$, we derive the standard relations from Eqs. (6) and (7)

$$h_n = \frac{2n+1}{2(n-1)}, \quad k_n = \frac{3}{2(n-1)}, \quad (19)$$

$$h_2 = 2.5, \quad k_2 = 1.5.$$

Substituting $h_2 = 2.5$ into (16) yields formulas for the increments of the semiaxes of a homogeneous satellite (Jeffreys 1962):

$$(\Delta a)_0 = \frac{35}{12}\alpha s_1, \quad (\Delta b)_0 = -\frac{5}{6}\alpha s_1, \quad (20)$$

$$(\Delta c)_0 = -\frac{25}{12}\alpha s_1.$$

The parameters of the gravitational field for the Galilean satellites determined in the Galileo space mission (Anderson *et al.* 1996, 1998, 2001a, 2001b) have shown that relation (18) holds with a high accuracy. Consequently, these bodies have equilibrium figures. For Io, J_2 and C_{22} are given to the fourth decimal place. The main relation (18) that is used to judge whether Io has an equilibrium figure was derived in the first approximation. Therefore, the following question arises: With what accuracy is the theoretical formula (18) valid? To answer this question, we must construct a theory in the next (second) approximation by including the terms of the order of α^2. This is the main goal of our analysis. In addition, this analysis provides a deeper insight into the whole problem.

THE EFFECT FROM THE THIRD SPHERICAL FUNCTION IN THE TIDAL POTENTIAL

The third spherical function W_3 in the tidal potential on the satellite surface at $s = s_1$ is proportional to $\alpha_1 \equiv \alpha(s_1/R)$. For Io (see the table), the ratio $s_1/R \approx 432 \times 10^{-5}$. Consequently, α_1 is of the order of α^2. Accordingly, the fourth spherical function W_4 is proportional to $\alpha_2 \equiv \alpha(s_1/R)^2$, and the ratio $\alpha_2/\alpha^2 \approx 10.85 \times 10^{-3}$. Thus, the effects from W_4 are two orders of magnitude smaller than those studied here, and they may be disregarded. The Love numbers k_n determine the tidally perturbed external gravitational potential of the satellite

$$U_t(r, \theta, \varphi) = \sum_{n=2}^{\infty} k_n \left(\frac{s_1}{r}\right)^{n+1} W_n = \sum_{n=2}^{\infty} U_{tn}. \quad (21)$$

Applying the Legendre polynomial addition theorem and comparing the result obtained with the general expansion of the response to a tide in the gravitational field of the satellite, we can easily derive general formulas for the gravitational moments:

$$J_n = -k_n (M/m_0) (s_1/R)^{n+1} P_n(t'), \quad (22)$$

$$\left.\begin{array}{c} C_{nm} \\ S_{nm} \end{array}\right\} = 2\frac{(n-m)!}{(n+m)!} \quad (23)$$

$$\times k_n (M/m_0) \left(\frac{s_1}{R}\right)^{n+1} P_n^m(t') \left\{\begin{array}{c} \cos m\varphi' \\ \sin m\varphi', \end{array}\right.$$

where θ' and φ' are the angular coordinates of Jupiter, $\theta' = \pi/2, \varphi' = 0, t' = cos\theta' = 0, P_n^m(t')$ ate the associated Legendre polynomials of the nth degree and the mth order. For the third spherical function W_3, all $S_{3m} = 0$. Since $P_3(0) = 0, P_3^1(0) = -3/2, P_3^2(0) = 0, P_3^3(0) = 15$, only

$$C_{31} = -\frac{1}{4}\alpha_1 k_3 \text{ and } C_{33} = \frac{1}{24}\alpha_1 k_3, \quad (24)$$

$$J_3 = 0 \text{ and } C_{32} = 0 \quad (25)$$

are nonzero.

In the first nonvanishing approximation of the figure theory, we derive relation (18) that was used to judge whether the Galilean satellites of Jupiter have equilibrium figures. The same relation for the third spherical function is

$$C_{31}/C_{33} = -6. \quad (26)$$

If it turns out that relations (25) and (26) hold for Io, then this will imply that Io is in a more "detailed" hydrostatic equilibrium than can be judged from the fulfillment of relation (18) alone. If relations (25) and (26) do not hold, then we can determine the extent to which Io deviates from hydrostatic equilibrium. When conditions (25) and (26) are satisfied, then, apart from k_2 (or h_2), which is used as a constraint when modeling the internal structure of the Galilean satellites, another constraint, more specifically, a constraint on k_3 (or h_3), arises.

Using (8), we can easily derive an expression for the third spherical function of the equilibrium figure:

$$u_{t3}(s, \theta, \varphi) = \frac{H_3(s)}{s}\alpha\left(\frac{s_1}{R}\right) \quad (27)$$

$$\times s \left(-\frac{1}{4}P_3^1(t)\cos\varphi + \frac{1}{24}P_3^3(t)\cos 3\varphi\right).$$

Setting $s = s_1, h_3 = H_3(s_1)/s_1$, and $\alpha_1 = \alpha(s_1/R)$, we represent (27) as

$$u_{t3}(s_1, \theta, \varphi) \quad (28)$$

$$= \alpha_1 h_3 s_1 \left(-\frac{1}{4}P_3^1(t)\cos\varphi + \frac{1}{24}P_3^3(t)\cos 3\varphi\right).$$

For the increments of the semiaxes, we obtain

$$\Delta a_{t3} = \alpha_1 h_3 s_1, \quad \Delta b_{t3} = \Delta c_{t3} = 0. \quad (29)$$

For the homogeneous model, $h_3 = 1.75$ and $\Delta a_{t3} = 23.7$ m, $k_3 = 0.75$ and

$$C_{31} = -\frac{3}{16}\alpha_1, \quad C_{33} = \frac{1}{32}\alpha_1. \quad (30)$$

THE SECOND APPROXIMATION: A GENERAL THEORY

The simplicity of the preceding analysis stems from the fact that we have studied problems for which the linear approximation was sufficient. In the linear statement, the actual radius r may be substituted with s. The general method of the figure theory presented in the paper by Zharkov and Trubitsyn (1975) and in the book by Zharkov and Trubitsyn (1980) should be used to calculate all effects of the second approximation. In the linear approximation, the shape of the equipotential surfaces is described by (14), (15) and (27), (28); these formulas define the deviations from the radius s of a sphere of equivalent volume of the order of α (4) and α^2, respectively. These deviations are proportional to the following spherical functions: $P_2(t)$, $P_2^2(t)\cos 2\varphi$, $P_3^1(t)\cos\varphi$, and $P_3^3(t)\cos 3\varphi$. The terms proportional to the components of the third spherical function are of the order of α^2 and do not need refinement. The terms proportional to the second spherical function are on the order of α. They are even functions of the angles θ and φ. Therefore, to construct a theory to within terms on the order of α^2, as is the case in the general figure theory (Zharkov and Trubitsyn 1975, 1980), the formula that gives the change from (r, θ, φ) to (s, θ, φ) must contain terms proportional to the even components of the fourth-degree ($n = 4$) spherical function: $P_4(t)$, $P_4^2(t)\cos 2\varphi$, and $P_4^4(t)\cos 4\varphi$. Thus, the relation between r and s is

$$r = s(1 + s_0 + s_2 P_2(t)) + s_{22}P_2^2(t)\cos 2\varphi \quad (31)$$
$$+ s_{31}P_3^1(t)\cos\varphi + s_{33}P_3^3(t)\cos 3\varphi + s_4 P_4(t)$$
$$+ s_{42}P_4^2(t)\cos 2\varphi + +s_{44}P_4^4(t)\cos 4\varphi.$$

The functions $s_{31}(s)$ and $s_{33}(s)$ are on the order of α^2 and were determined in the previous section (see (27)):

$$s_{31}(s) = -\frac{1}{4}\frac{H_3(s)}{s}\alpha\left(\frac{s}{R}\right), \quad (32)$$
$$s_{33}(s) = \frac{1}{24}\frac{H_3(s)}{s}\alpha\left(\frac{s}{R}\right), \quad \alpha_1 = \alpha\left(\frac{s_1}{R}\right).$$

They are known and do not enter into the subsequent transformations. Formula (31) contains the function

$s_0(s)$ which is not related to the dependence of the equilibrium figure on the angles. This function is not independent and can be found from the condition for determining the radius s of a sphere of equivalent volume (Zharkov and Trubitsyn 1975, 1980). To within terms of the second order, we obtain

$$-s_0(s) = \frac{1}{5}s_2^2(s) + \frac{12}{5}s_{22}^2(s). \quad (33)$$

In the first approximation, the functions of the figure $s_2(s)$ and $s_{22}(s)$ were calculated above in the linear approximation (see (14)):

$$s_2(s) = -\frac{5}{6}\frac{H_2(s)}{s}\alpha, \quad s_{22}(s) = \frac{1}{4}\frac{H_2(s)}{s}\alpha. \quad (34)$$

Substituting s_2 and s_{22} into (33) yields $s_0(s)$:

$$s_0(s) = \frac{13}{45}h_2^2(s)\alpha^2, \quad h_2(s) = \frac{H_2(s)}{s}. \quad (35)$$

It remains to determine the functions of the figure $s_2(s)$ and $s_{22}(s)$ in the second approximation and the functions $s_4(s)$, $s_{42}(s)$, and $s_{44}(s)$, which are on the order of α^2, in the first nonvanishing approximation. To this end, according to the theory (Zharkov and Trubitsyn 1975, 1980), we must write an analytical equation for the equipotential surface of the total potential $U(r, \theta, \varphi) = V + W_2 + Q$ and change (r, θ, φ) to (s, θ, φ) in $V(r, \theta, \varphi)$, $W_2(r, \theta, \varphi)$, and $Q(r, \theta)$, i.e., substitute r using formula (31), in which the functions of the second order of smallness $s_{31}(s)$ and $s_{33}(s)$ have already been calculated (32) and they may be omitted. Since the potential is constant on an equipotential surface, setting the expressions in front of $P_2(t)$, $P_2^2(t)\cos 2\varphi$, $P_4(t)$, $P_4^2(t)\cos 2\varphi$, and $P_4^4(t)\cos 4\varphi$ equal to zero, we obtain five integrodifferential equations for the sought functions. The sixth equation that gives the potential on equipotential surfaces contains only the sought functions of the figure.

Substituting r (31) into W_2 (1) and Q (3) and retaining the terms no higher than the second order of smallness, we obtain after simple transformations

$$W_2(s, \theta, \varphi) = \frac{Gm_0}{s_1}\alpha\left(\frac{s}{s_1}\right)^2\left\{-\frac{1}{5}(s_2 - 6s_{22})\right. \quad (36)$$
$$-\left(\frac{1}{2} + \frac{2}{7}s_2 + \frac{12}{7}s_{22}\right)P_2$$
$$+\left(\frac{1}{4} - \frac{1}{7}s_2 + \frac{2}{7}s_{22}\right)P_2^2\cos 2\varphi - \frac{18}{35}(s_2 - s_{22})P_4$$
$$\left. + \frac{3}{70}\left(s_2 - 2s_{22}\right)P_4^2\cos 2\varphi + \frac{3}{140}s_{22}P_4^4\cos 4\varphi\right\},$$

$$Q(s, \theta, \varphi) = \frac{Gm_0}{3s_1}\alpha\left(\frac{s}{s_1}\right)^2\left\{\left(1 - \frac{2}{5}s_2\right)\right. \quad (37)$$

$$-\left(1 - \frac{10}{7}s_2\right)P_2 + \frac{18}{7}s_{22}P_2^2\cos 2\varphi$$

$$-\frac{36}{35}s_2 P_4 - \frac{6}{35}s_{22}P_4^2\cos 2\varphi\Bigg\},$$

where the arguments $t = \cos\theta$ in the Legendre polynomials and s in the functions of the figure were omitted.

The potential produced by the mass distribution in the satellite at an arbitrary point with coordinates (r, θ, φ) is

$$V(r, \theta, \varphi) = G\int\limits_\tau \frac{\rho(\mathbf{r}')}{|\mathbf{r} - \mathbf{r}'|}d\tau', \qquad (38)$$

where $\rho(\mathbf{r}')$ is the matter density inside the satellite, $\mathbf{r}'$ is the radius vector of the current point, G is the gravitational constant, which is equal to 0.6672×10^{-7} in the CGS system, and the integration is over the entire volume τ of the satellite. The transformation of the potential V (38) is more cumbersome than that of the potentials W_2 (1) and Q (3), but, in principle, it is performed in the same way as in the theory of an equilibrium figure (Zharkov and Trubitsyn 1975, 1980). Expanding the function $1/|\mathbf{r} - \mathbf{r}'|$ in (38) in terms of Legendre polynomials (Zharkov and Trubitsyn 1980), we represent the gravitational potential of the satellite $V(r, t, \varphi), t = \cos\theta$ for an arbitrary point (r, t, φ) inside the satellite as the sum of multipole moments and retain the terms no higher than the second order of smallness in the expansion:

$$V(r, t, \varphi) = \frac{G}{r}\{(D_0 + rD_0') \qquad (39)$$

$$+ \left(r^{-2}D_2 + r^3D_2'\right)P_2(t)$$

$$+ \left(r^{-2}D_{22} + r^3D_{22}'\right)P_2^2(t)\cos 2\varphi$$

$$+ \left(r^{-4}D_4 + r^5D_4'\right)P_4(t)$$

$$+ \left(r^{-4}D_{42} + r^5D_{42}'\right)P_4^2(t)\cos 2\varphi$$

$$+ \left(r^{-4}D_{44} + r^5D_{44}'\right)P_4^4(t)\cos 4\varphi\},$$

where

$$D_0 = \int\limits_{r'<r}\rho(r')d\tau', \quad D_0' = \int\limits_{r'>r}\frac{\rho(r')}{r'}d\tau', \quad (40)$$

$$D_2 = \int\limits_{r'<r}\rho(r')r'^2P_2(t')d\tau',$$

$$D_2' = \int\limits_{r'>r}\rho(r')r'^{-3}P_2(t')d\tau',$$

$$D_{22} = \frac{2}{4!}\int\limits_{r'<r}\rho(r')r'^2P_2^2(t')\cos 2\varphi'd\tau',$$

$$D_{22}' = \frac{2}{4!}\int\limits_{r'>r}\rho(r')r'^{-3}P_2^2(t')\cos 2\varphi'd\tau',$$

$$D_4 = \int\limits_{r'<r}\rho(r')r'^4P_4(t')d\tau',$$

$$D_4' = \int\limits_{r'>r}\rho(r')r'^{-5}P_4^2(t')d\tau',$$

$$D_{42} = \frac{4}{6!}\int\limits_{r'>r}\rho(r')r'^4P_4^2(t')\cos 2\varphi'd\tau',$$

$$D_{42}' = \frac{4}{6!}\int\limits_{r'>r}\rho(r')r'^{-5}P_4^2(t')\cos 2\varphi'd\tau',$$

$$D_{44} = \frac{2}{8!}\int\limits_{r'<r}\rho(r')r'^4P_4^4(t')\cos 4\varphi'd\tau',$$

$$D_{44}' = \frac{2}{8!}\int\limits_{r'>r}\rho(r')r'^{-5}P_4^4(t')\cos 4\varphi'd\tau'.$$

In the transformation $r \rightarrow s$, the radius s may be said to number the equipotential surfaces; since the density on an equipotential surface is constant, we may substitute $\rho(s')$ for $\rho(r')$ in integrals (40). In their book, Zharkov and Trubitsyn (1980) provided arguments according to which the $\mathbf{r}' = \mathbf{r}(s, t, \varphi)$ equipotential surface passing through the point (r, t, φ) at which the potential is sought may be substituted for the $\mathbf{r}' = \mathbf{r}$ sphere within the integration limits in (40). As a result, the moments in (40) become functions of not the actual radius r, but s, and the variables s, t, φ in integrals (40) are separated. Substituting r (31) into (40) and performing simple integrations yields

$$D_0 = \frac{4\pi}{3}\int\limits_0^s \rho(s')d[s'^3], \qquad (41)$$

$$D_0' = \frac{4\pi}{2}\int\limits_s^{s_1}\rho(s')d\left[s'^2\left(1 - \frac{1}{5}s_2^2 - \frac{12}{5}s_{22}^2\right)\right],$$

$$D_2 = \frac{4\pi}{5}\int\limits_0^s \rho(s')d\left[s'^5\left(s_2 + \frac{4}{7}s_2^2 - \frac{48}{7}s_{22}^2\right)\right],$$

$$D_2' = \frac{4\pi}{5}\int\limits_s^{s_1}\rho(s')d\left[s_2 - \frac{1}{7}s_2^2 + \frac{12}{7}s_{22}^2\right],$$

$$D_{22} = \frac{4\pi}{5}\int\limits_0^s \rho(s')d\left[s'^5\left(s_{22} - \frac{8}{7}s_2s_{22}\right)\right],$$

$$D'_{22} = \frac{4\pi}{5} \int\limits_{s}^{s_1} \rho(s')d \left[s_{22} + \frac{2}{7}s_2 s_{22} \right],$$

$$D_4 = \frac{4\pi}{9} \int\limits_{0}^{s} \rho(s')d \left[s'^7 \left(s_4 + \frac{54}{35}s_2^2 + \frac{108}{35}s_{22}^2 \right) \right],$$

$$D'_4 = \frac{4\pi}{9} \int\limits_{s}^{s_1} \rho(s')d \left[s'^{-2} \left(s_4 - \frac{27}{35}s_2^2 - \frac{54}{35}{}_2 s_{22}^2 \right) \right],$$

$$D_{42} = \frac{4\pi}{9} \int\limits_{0}^{s} \rho(s')d \left[s'^7 \left(s_{42} + \frac{18}{35}s_2 s_{22} \right) \right],$$

$$D'_{42} = \frac{4\pi}{9} \int\limits_{s}^{s_1} \rho(s')d \left[s'^{-2} \left(s_{42} - \frac{9}{35}s_2 s_{22} \right) \right],$$

$$D_{44} = \frac{4\pi}{9} \int\limits_{0}^{s} \rho(s')d \left[s'^7 \left(s_{44} + \frac{3}{35}s_{22}^2 \right) \right],$$

$$D'_{44} = \frac{4\pi}{9} \int\limits_{s}^{s_1} \rho(s')d \left[s'^{-2} \left(s_{44} - \frac{3}{70}s_{22}^2 \right) \right].$$

It is now easy to understand how the sought relations are derived. Substituting the transformed multipole moments (41) into (39) and eliminating the powers of the radius r using (31), we obtain an expression for the potential $V(s, t, \varphi)$ as a function of (s, t, φ). It is convenient to pass to the dimensionless variables $x = s/s_1$ and $\delta(s) = \rho(s)/\rho_0$ in (41), where ρ_0 is the mean density, and substitute the moments themselves with their dimensionless equivalent expressions:

$$S_n(x) = x^{-n-3} \int\limits_{0}^{x} \delta(z)d \left[z^{n+3} f_n \right], \qquad (42)$$

$$S'_n(x) = x^{n-2} \int\limits_{x}^{1} \delta(z)d \left[z^{2-n} f'_n \right],$$

$$S_{nm}(x) = x^{-n-3} \int\limits_{0}^{x} \delta(z)d \left[z^{n+3} f_{nm} \right],$$

$$S'_{nm}(x) = x^{n-2} \int\limits_{x}^{1} \delta(z)d \left[z^{2-n} f'_{nm} \right],$$

where

$$f_0 = 1, \quad f'_0 = \frac{3}{2} \left(1 - \frac{1}{5}s_2^2 - \frac{12}{5}s_{22}^2 \right), \qquad (43)$$

$$f_2 = \frac{3}{5} \left(s_2 + \frac{4}{7}s_2^2 - \frac{48}{7}s_{22}^2 \right),$$

$$f'_2 = \frac{3}{5} \left(s_2 - \frac{1}{7}s_2^2 + \frac{12}{7}s_{22}^2 \right),$$

$$f_{22} = \frac{3}{5} \left(s_{22} - \frac{8}{7}s_2 s_{22} \right),$$

$$f'_{22} = \frac{3}{5} \left(s_{22} + \frac{2}{7}s_2 s_{22} \right),$$

$$f_4 = \frac{1}{3} \left(s_4 + \frac{54}{35}s_2^2 + \frac{108}{35}s_{22}^2 \right),$$

$$f'_4 = \frac{1}{3} \left(s_4 - \frac{27}{35}s_2^2 - \frac{54}{35}s_{22}^2 \right),$$

$$f_{42} = \frac{1}{3} \left(s_{42} + \frac{18}{35}s_2 s_{22} \right),$$

$$f'_{42} = \frac{1}{3} \left(s_{42} - \frac{9}{35}s_2 s_{22} \right),$$

$$f_{44} = \frac{1}{3} \left(s_{44} + \frac{3}{35}s_{22}^2 \right), \quad f'_{44} = \frac{1}{3} \left(s_{44} - \frac{3}{70}s_{22}^2 \right).$$

Setting $x = 1$ in (42), we obtain integral formulas for the first even gravitational moments that determine the external gravitational field of Io in hydrostatic equilibrium:

$$J_2 = -S_2(1), \quad J_4 = -S_4(1), \quad S_0(1) = 1, \quad (44)$$
$$C_{22} = S_{22}(1), \quad C_{42} = S_{42}(1), \quad C_{44} = S_{44}(1).$$

Adding up $V(s, t, \varphi)$, $W_2(s, t, \varphi)$ (36), and $Q(s, t, \varphi)$ (37), we obtain the sought potential on equipotential surfaces of Io in equilibrium,

$$U(s) = V(s, t, \varphi) + W_2(s, t, \varphi) + Q(s, t, \varphi), \quad (45)$$

$$U(s)\frac{s_1^3}{Gm_0 s^2} = U_0(s) + A_2(s)P_2(t)$$
$$+ A_{22}(s)P_2^2(t)\cos 2\varphi + A_4(s)P_4(t)$$
$$+ A_{42}(s)P_4^2(t)\cos 2\varphi + A_{44}(s)P_4^4(t)\cos 4\varphi,$$

where

$$U_0(s)\frac{Gm_0 s^2}{s_1^3} = \left[1 + \frac{2}{5} \left(s_2^2 + 12s_{22}^2 \right) \right] S_0(x) \quad (46)$$

$$+ S'_0(x) - \frac{3}{5}s_2 S_2(x) - \frac{36}{5}s_{22}S_{22}(x) + \frac{2}{5}s_2 S'_2(x)$$

$$+ \frac{24}{5}s_{22}S'_{22}(x) + \frac{\alpha}{3} \left[1 - s_2 + \frac{18}{5}s_{22} \right],$$

$$A_2(x) = - \left(s_2 - \frac{2}{7}s_2^2 + \frac{24}{7}s_{22}^2 \right) S_0(x) \quad (47)$$

$$+ \left(1 - \frac{6}{7}s_2 \right) S_2(x) + \left(1 + \frac{4}{7}s_2 \right) S'_2(x)$$

$$+ \frac{72}{7}s_{22}S_{22}(x) - \frac{48}{7}s_{22}S'_{22}(x)$$

$$+ \frac{\alpha}{3}\left[-\frac{5}{2} + \frac{4}{7}s_2 - \frac{36}{7}s_{22}\right] = 0,$$

$$A_4(x) = -\left(s_4 - \frac{18}{35}s_2^2 - \frac{36}{35}s_{22}^2\right)S_0(x) \qquad (48)$$

$$- \frac{54}{35}s_2 S_2(x) + \frac{36}{35}s_2 S_2'(x) - \frac{108}{35}s_{22}S_{22}(x)$$

$$+ \frac{72}{35}s_{22}S_{22}'(x) + S_4(x) + S_4'(x)$$

$$- \frac{\alpha}{3}\left[\frac{18}{7}s_2 - \frac{54}{35}s_{22}\right] = 0,$$

$$A_{22}(x) = -\left(s_{22} + \frac{4}{7}s_2 s_{22}\right)S_0(x) + \frac{6}{7}s_{22}S_2(x)$$
$$\qquad (49)$$

$$- \frac{4}{7}s_{22}S_2'(x) + \left(1 + \frac{6}{7}s_2\right)S_{22}(x)$$

$$+ \left(1 - \frac{4}{7}s_2\right)S_{22}'(x) + \frac{\alpha}{3}\left[\frac{3}{4} - \frac{3}{7}s_2 + \frac{24}{7}s_{22}\right] = 0,$$

$$A_{42}(x) = -\left(s_{42} - \frac{6}{35}s_2 s_{22}\right)S_0(x) - \frac{9}{35}s_{22}S_2(x)$$
$$\qquad (50)$$

$$+ \frac{6}{35}s_{22}S_2'(x) - \frac{9}{35}s_2 S_{22}(x) + \frac{6}{35}s_2 S_{22}'(x)$$

$$+ S_{42}(x) + S_{42}'(x) + \frac{\alpha}{3}\left[\frac{9}{70}s_2 - \frac{3}{7}s_{22}\right] = 0,$$

$$A_{44}(x) = -\left(s_{44} - \frac{3}{70}s_{22}^2\right)S_0(x) - \frac{9}{70}s_{22}S_{22}(x)$$
$$\qquad (51)$$

$$+ \frac{3}{35}s_{22}S_{22}'(x) + S_{44}(x) + S_{44}'(x) + \frac{3}{140}\alpha s_{22} = 0,$$

where the argument $x = s/s_1$ in the function of the figure was omitted. The five integrodifferential equations (47)–(51) allow all functions of the figure theory to be determined to within terms of the second order of smallness. In Eqs. (47)–(51), the small parameter α (4) and the radial density distribution in the satellite $\rho(s)$ (or $\delta(x)$) are assumed to be given. If we know the equation of state for the satellite $p(\rho)$ rather than the density distribution $\delta(x)$, then the function $\delta(x)$ can first be found from the hydrostatic equilibrium equation

$$\frac{1}{\rho}\frac{dP(\rho)}{ds} = \frac{Gm_0}{s_1^3}\frac{d(s^2 U_0)}{ds}. \qquad (52)$$

According to (46), the tidal and rotational corrections to the standard hydrostatic equilibrium equation are of the second order of smallness.

It is useful to transform the system of equations for the figure theory (47)–(51) by integrating the dimensionless moments S_n, S_n', S_{nm}, and S_{nm}' by parts by transferring the differential to the density $\delta(x')$, which is assumed to be given (Zharkov *et al.* 1973). The resulting integrals may be considered as the Stieltjes integrals. In general, $\delta(x)$ is a piecewise continuous function. Let us number the continuous segments of the function $\delta(x)$ from the center of the satellite to its surface $(1, 2, \ldots, n)$ and denote the points at which the function has discontinuities by x_i and the number of the segment adjacent to x_i from the left (from the smaller radius) by i. We refer the point x_i to the ith segment. There are a total of $n - 1$ points of discontinuity with coordinates x_1, x_2, ..., x_{n-1}. The point x_n denotes the extreme point of the integration domain $(x_n = 1)$. We write the discontinuity of the dimensionless density $\delta(x)$ at x_i as

$$\Delta\delta_i = \delta(x_i) - \delta(x_i + 0) \qquad (53)$$
$$\text{for } 1 \le i \le n - 1, \quad \Delta\delta_n = \delta(x_n).$$

As a result, the dimensionless moments (42) take the form

$$S_n(x) = f_n(x)\delta(x) + x^{-n-3} \qquad (54)$$

$$\times \left[\sum_{i=1}^{j-1} x_i^{n+3} f_n(x_i)\Delta\delta_i - \int_0^x z^{n+3} f_n(z)d\delta(z)\right],$$

$$S_n'(x) = f_n'(x)\delta(x)$$

$$+ x^{n-2}\left[\sum_{i=j}^{n} x_i^{2-n} f_n'(x_i)\Delta\delta_i - \int_x^1 z^{2-n} f_n'(z)d\delta(z)\right],$$

$$S_{nm}(x) = f_{nm}(x)\delta(x) + x^{-n-3}$$

$$\times \left[\sum_{i=1}^{j-1} x_i^{n+3} f_{nm}(x_i)\Delta\delta_i - \int_0^x z^{n+3} f_{mn}(z)d\delta(z)\right],$$

$$S_{nm}'(x) = f_{nm}'(x)\delta(x) + x^{n-2}$$

$$\times \left[\sum_{i=j}^{n} x_i^{2-n} f_{nm}'(x_i)\Delta\delta_i - \int_x^1 z^{2-n} f_{nm}'(z)d\delta(z)\right],$$

where $x_{j-1} < x < x_j$ and the functions $f_n(x)$, $f_n'(x)$, $f_{nm}(x)$, and $f_{nm}'(x)$ are given in (43).

The convenience of transformation (54) follows from the fact that piecewise constant density distributions are currently used in constructing models for Io. In this case, the integrals in Eqs. (47)–(51) of the figure theory vanish. Since the methods for solving the equations of figure theory were described in detail by Zharkov *et al.* (1973) and Zharkov and Trubytsyn (1980), we will not consider them here.

ALGEBRAIC RELATIONS

The values of the functions of the figure at $x = 1$ are called the figure parameters. The figure parameters in (31) specify the shape of the figure of an equilibrium satellite. Setting $x = 1$ in Eqs. (47)–(51), we obtain algebraic formulas that relate the gravitational moments (44) to the figure parameters:

$$J_2 = -s_2 - \frac{5}{6}\alpha - \frac{4}{7}s_2^2 + \frac{48}{7}s_{22}^2 - \frac{11}{21}as_2 - \frac{30}{7}\alpha s_{22}, \quad (55)$$

$$C_{22} = s_{22} - \frac{1}{4}\alpha - \frac{8}{7}s_{22}s_2 + \frac{5}{14}\alpha s_2 - \frac{13}{7}\alpha s_{22},$$

$$J_4 = -s_4 - \frac{36}{35}s_2^2 - \frac{72}{35}s_{22}^2 - \frac{15}{7}\alpha s_2 + \frac{9}{7}as_{22},$$

$$C_{42} = s_{42} + \frac{12}{35}s_2 s_{22} - \frac{3}{28}\alpha s_2 + \frac{5}{14}\alpha s_{22},$$

$$C_{44} = s_{44} + \frac{3}{35}s_{22}^2 - \frac{3}{56}\alpha s_{22}.$$

Relations (55) can be reversed:

$$s_2 = -\left(J_2 + \frac{5}{2}\alpha\right) - \frac{4}{7}J_2^2 \quad (56)$$

$$- \frac{38}{63}\alpha^2 - \frac{3}{7}\alpha J_2 + \frac{48}{7}C_{22}^2 - \frac{6}{7}\alpha C_{22},$$

$$s_{22} = C_{22} + \frac{1}{4}\alpha - \frac{8}{7}J_2 C_{22}$$
$$+ \frac{1}{14}\alpha J_2 + \frac{11}{21}a^2 + \frac{19}{21}\alpha C_{22},$$

$$s_4 = -J_4 - \frac{36}{35}J_2^2 - \frac{72}{35}C_{22}^2$$
$$+ \frac{177}{140}\alpha^2 + \frac{3}{7}\alpha J_2 - \frac{99}{140}\alpha C_{22},$$

$$s_{42} = C_{42} + \frac{12}{35}J_2 C_{22} + \frac{1}{14}\alpha^2 - \frac{3}{140}aJ_2 + \frac{9}{14}\alpha C_{22},$$

$$s_{44} = C_{44} - \frac{3}{35}C_{22}^2 + \frac{9}{1120}\alpha^2 + \frac{3}{280}aC_{22}.$$

If the satellite is in hydrostatic equilibrium, then the coefficients in the expansion of its external gravitational field in terms of spherical functions can be determined by measuring its figure parameters. The reverse is also true. Relations (55) and (56) express the dualism in figure theory. The problem under consideration is peculiar in that both J_2 and C_{22}, to within terms of the second order, are determined via the small parameter α (4) and the Love number of the second order k_2 (or $h_2 = 1 + k_2$). Indeed, substituting $s_2(1)$ and $s_{22}(1)$ (34) into (55) yields

$$J_2 = \frac{5}{6}k_2\alpha - \frac{40}{63}\left(1 - \frac{1}{20}h_2\right)h_2\alpha^2, \quad (57)$$

$$C_{22} = \frac{1}{4}k_2\alpha - \frac{16}{21}\left(1 - \frac{5}{16}h_2\right)h_2a^2, \quad (58)$$

$$\frac{J_2}{C_{22}} = \frac{10}{3}\left\{1 + \frac{16}{21}\frac{h_2}{k_2}(3 - h_2)a\right\}. \quad (59)$$

Formulas (57)–(59) may be used to correct the Galileo data (Anderson *et al.* 2001a).

The Love number k_2 in the paper by Anderson *et al.* (2001a) was found by using formula of the first approximation (13) and the observed value of $C_{22} = (553.7 \pm 1.2) \times 10^{-6}$:

$$k_2 = 4(C_{22}/\alpha) = 1.2924 \pm 0.0027. \quad (60)$$

The quadrupole moment J_2 is determined with a lower accuracy and is chosen to satisfy the theoretical formula (18), which is derived in the linear approximation. Since the correction of the second approximation to C_{22} is, according to (58), negative, to correct k_2, it should be added to the observed value of C_{22} and formula (13) should be applied to the derived C_{22}^*:

$$k_2^* = 4(C_{22}^*/\alpha) = 1.2958 \pm 0.0027. \quad (61)$$

Thus, allowing for the second approximation affects the fourth digit in k_2 (60).

To determine the dimensionless moment of inertia, Anderson *et al.* (2001a) used a formula valid in the Rado approximation for a satellite in hydrostatic equilibrium from the book by Jeffreys (1962):

$$\frac{C}{m_0 s_1^2} = \frac{2}{3}\left(1 - \frac{2}{5}\sqrt{\frac{4 - k_2}{1 + k_2}}\right) \quad (62)$$
$$= 0.37685 \pm 0.00035.$$

(For more details on the meaning of (62), see the next section.) Substituting k_2^* (61) for k_2 in (62) yields 0.37725, i.e., corrects the third decimal place.

The general formula for the radius of an equilibrium spheroid in the second approximation (31) allows the corresponding formulas for the semiaxes of the equilibrium figure of Io to be written. Since $P_2(0) = -1/2$, $P_2^2(0) = 3$, $P_3^1(0) = -3/2$, $P_3^3(0) = 15$, $P_4^0(0) = 3/8$, $P_4^2(0) = -15/2$, $P_4^4(0) = 105$, $P_2(1) = P_4(1) = 1$, $P_2^2(1) = P_3^1(1) = P_3^3(1) = P_4^2(1) = P_4^4(1) = 0$, we obtain

$$a = s_1\left\{1 + s_0(1) - \frac{1}{2}s_2(1) + 3s_{22}(1)\right. \quad (63)$$
$$- \frac{3}{2}s_{31}(1) + 15s_{33}(1) + \frac{3}{8}s_4(1)$$
$$\left. - \frac{15}{2}s_{42}(1) + 105s_{44}(1)\right\},$$

$$b = s_1\left\{1 + s_0(1) - \frac{1}{2}s_2(1) - 3s_{22}(1)\right. \quad (64)$$
$$\left. + \frac{3}{8}s_4(1) + \frac{15}{2}s_{42}(1) + 105s_{44}(1)\right\},$$

$$c = s_1 \left\{ 1 + s_0(1) + s_2(1) + s_4(1) \right\}. \qquad (65)$$

The figure parameters $s_2(1)$ and $s_{22}(1)$, to within terms of the second order, can be easily determined from the algebraic relations (55) and (56):

$$s_2 = -\frac{5}{6} h_2 \alpha - \frac{40}{63} \left(1 - \frac{1}{20} h_2 \right) h_2 \alpha^2, \qquad (66)$$

$$s_{22} = \frac{1}{4} h_2 \alpha + \frac{16}{21} \left(1 - \frac{5}{16} h_2 \right) h_2 \alpha^2. \qquad (67)$$

Formulas (66) and (67) are valid for equilibrium models of Io with an arbitrary density distribution. The deviations of the semiaxes of the equilibrium Io a (63), b (64), and c (65) from the mean radius s_1 depend not only on s_2 (66) and s_{22} (67), s_{31} and s_{33} (28), which can be determined relatively easily, but also on the second-order figure parameters s_4, s_{42}, and s_{44}, whose determination requires solving Eqs. (48), (50), and (51). These equations admit a simple solution for the homogeneous model ($h_2 = 2.5$),

$$s_4 = \frac{885}{224} \alpha^2, \quad s_{42} = -\frac{75}{224} \alpha^2, \quad s_{44} = \frac{15}{896} \alpha^2 \qquad (68)$$

and the corresponding values of the gravitational moments

$$J_4 = -\frac{885}{224} \alpha^2, \quad C_{42} = -\frac{75}{224} \alpha^2, \quad C_{44} = \frac{15}{896} \alpha^2, \qquad (69)$$

where α (4) is the small parameter of the figure theory.

A TRIAL MODEL OF IO

Anderson *et al.* (2001) constructed a large number of two-layer (silicate mantle + Fe−FeS core) and three-layer (crust + silicate mantle + Fe−FeS core) models that satisfied the known mean density and moment of inertia of Io. We also considered this issue in detail previously (Zharkov 2003).

The orbital angular velocities of Io and Europa are in resonance $n_1 + 2n_2 \approx 0$. As a result, their circular orbits acquire small "forced" eccentricities. Since both satellites are fairly close to Jupiter, the latter generates powerful tidal waves on both bodies whose dissipation into heat affected significantly their structures. According to the most recent data (Matson *et al.* 2001), the heat flux from Io lies within the range $\sim (2-13.5) \times 10^3 \ \mathrm{erg \ cm^{-2} \ s^{-1}}$. The mean global heat fluxes from the Earth and the Moon are $\sim 87 \pm 2$ and $\sim 15-20 \ \mathrm{erg \ cm^{-2} \ s^{-1}}$, respectively. The temperatures of the lavas from the interiors of Io are very high (~ 1900 K). It is beyond doubt that the interiors of Io are strongly heated. The core of the satellite, composed of Fe−FeS eutectic, is molten, and the silicate mantle may be in a partially molten state.

In the two-layer model, the model of the outer layer of the satellite, the crust, which is of great interest for Io, drops out of the consideration. This issue was considered by Leone and Wilson (2001) (see also Zharkov 2003).

In our case, it seems natural to choose a simple trial model of Io that would differ from the homogeneous model (Zharkov 2003) to illustrate the theory.

Anderson *et al.* (2001a) took $\rho_1 = 5.15 \ \mathrm{g \ cm^{-3}}$ for the density of Io's core, which is assumed to consist of Fe−FeS eutectic and to be in a molten state. We then obtain the mean density for the silicate mantle, $\rho_2 = 3.25 \ \mathrm{g \ cm^{-3}}$, from the conservation condition for the satellite mass and the Love number k_2 ($k_2 = h_2 - 1$) (60). For the calculation of the Love numbers for the two-layer model, the solution of system (5)−(9) leads to the expression

$$h_n = \frac{Z_n}{Z_d}, \qquad (70)$$

where

$$Z_n = (2n + 1) \left[\left(\frac{\rho_1}{\rho_2} - 1 \right) x_c^3 + 1 \right]$$
$$\times \left\{ \left[(2n + 1) - 3 \left(1 - \frac{\rho_2}{\rho_1} \right) \right] \right.$$
$$\left. + 3 \left(1 - \frac{\rho_2}{\rho_1} \right) x_c^{(2n+1)} \right\},$$

$$Z_d = \left[(2n + 1) - 3 \left(1 - \frac{\rho_2}{\rho_1} \right) \right]$$
$$\times \left\{ (2n + 1) \left[\left(\frac{\rho_1}{\rho_2} - 1 \right) x_c^3 + 1 \right] - 3 \right\}$$
$$- 9 \left(1 - \frac{\rho_2}{\rho_1} \right) x_c^{(2n+1)},$$

$x = s/s_1$ is the relative radius, ρ_1 and ρ_2 are the core and mantle densities, respectively, $x_c = s_c/s_1$ is the core radius, and s_1 is the mean radius of Io.

For the model under consideration ($\rho_1 = 5.15 \ \mathrm{g \ cm^{-3}}$, $\rho_2 = 3.25 \ \mathrm{g \ cm^{-3}}$, $x_c = 0.5268$, $s_1 = 1821.6$ km),

$$h_2 = 2.2944, \qquad (71)$$

i.e., it is virtually equal to the observed value of $k_2 = (h_2 - 1)$ (60), (61).

The corresponding Love number of the third order is

$$h_3 = 1.6582. \qquad (72)$$

The mean (relative) moment of inertia for the model under consideration is

$$I^* = \frac{I}{m_0 s_1^2} = \frac{2}{5} \frac{\rho_2}{\rho_0} \left[\left(\frac{\rho_1}{\rho_2} - 1 \right) x_c^5 + 1 \right] = 0.37724. \qquad (73)$$

Formula (62) with the model value of $k_2 = (h_2 - 1)$ (71) yields an almost equal value of 0.37708.

Let us now explain the meaning of formula (62), which was used by Anderson *et al.* (2001) to constrain the moment of inertia of Io. Recall how this formula was derived. For the equilibrium figure of a rotating planet or satellite in the Rado approximation, the Rado–Darwin formula is valid (see, e.g., Zharkov and Trubitsyn 1980; formula (32.20))

$$\frac{C}{Ma_1^2} = \frac{2}{3}\left[1 - \frac{2}{5}\sqrt{\frac{5\alpha}{3J_2 + \alpha} - 1}\right], \quad (74)$$

where C is the polar moment of inertia, M is the mass, a_1 is the equatorial radius, J_2 is the quadrupole moment, and α (4) is the small parameter of the rotating equilibrium planet. Zharkov *et al.* (1985) showed that for a synchronously rotating equilibrium satellite in the field of the tidal potential in the first approximation, the equilibrium quadrupole moment J_2 of the body under consideration is the sum of the part attributable to the tidal potential $J_{2t} = 0.5\alpha k_2$ and the part attributable to the centrifugal potential $J_{2r} = 1/3\alpha k_2$:

$$J_2 = J_{2t} + J_{2r} = \frac{5}{6}\alpha k_2. \quad (75)$$

Formula (62) is obtained if we substitute not J_2 (75), but only the part of J_2, more specifically, J_{2r} into (74). Thus, it refers to an equilibrium rotating planet or satellite, i.e., to a similar, but not the same problem studied here. Therefore, it would be natural to use the Love number k_2 or h_2 as a constraint when modeling any Galilean satellite.

In the first approximation, the formulas for the principal moments of inertia are

$$A = \frac{8\pi}{15}\int_0^{s_1} \rho(s)d\left[s^5\left(1 + \frac{1}{2}s_2(s) - 2s_{22}(s)\right)\right]$$
$$(76)$$

(relative to the x axis directed from Io's center of mass to Jupiter),

$$B = \frac{8\pi}{15}\int_0^{s_1} \rho(s)d\left[s^5\left(1 + \frac{1}{2}s_2(s) + 2s_{22}(s)\right)\right]$$
$$(77)$$

(relative to the y axis directed along the orbital motion of Io),

$$C = \frac{8\pi}{15}\int_0^{s_1} \rho(x)d\left[s^5\left(1 - s_2(s)\right)\right] \quad (78)$$

(relative to the z axis directed along the rotation axis of Io).

Formulas (76)–(78) include the functions of the figure $s_2(s)$ (66) and s_{22} (67), which, in turn, are determined by the function of the Love number $h_2(s)$. It follows from (76)–(78) that the difference between all moments (A, B, C) is of the order of α (4), i.e., in the third decimal place.

The Love numbers h_2 (71) and h_3 (72) for the two-layer model under consideration and the figure parameters s_4, s_{42}, and s_{44} (68) for the homogeneous model allow us to estimate the contribution from the effects of the second approximation to the lengths of the semiaxes a (63), b (64), and c (65) for the equilibrium figure of Io. Including these effects lengthens the a, b, and c semiaxes by ~ 64.5, ~ 26, and ~ 14 m, respectively.

CONCLUSIONS

The determination of the first gravitational moments by the Galileo spacecraft showed that J_2 and C_{22} satisfy relation (18), which is valid for bodies in hydrostatic equilibrium. It was concluded that all Galilean satellites are close to hydrostatic equilibrium. The Love number k_2 (60) was estimated with a high accuracy, which is virtually equivalent to the determination of the mean moment of inertia. As a result, significant progress in modeling the internal structure of the Galilean satellites has been made, while the models themselves contain information about the conditions under which Jupiter was formed. The data for Io were so accurate that Anderson *et al.* (2001a) used the formulas obtained in the second approximation of the perturbation theory by Dermott and Thomas (1988) to describe the observational data; the latter authors used several assumptions to derive the formulas of the second approximation. Therefore, we considered this question in a more rigorous and consistent way. We showed that to describe all effects of the second approximation, formula (31) for the figure of the satellite must contain not only the components of the second spherical function, but also the components of the third and fourth spherical functions. Measurements of the third-order gravitational moments (see formulas (24) and (25)) could reveal the extent to which the hydrostatic equilibrium conditions are satisfied for Io. In this sense, relation (26) plays the same role as formula (18) did in finding out whether the Galilean satellites are in hydrostatic equilibrium.

We calculated the corrections of the second order of smallness both to the gravitational moments J_2 and C_{22} (formulas (57) and (58)) and to the main relation (18) (formula (59)). We considered the determination of the moment of inertia for Io via the Love number k_2. We concluded that when modeling the internal structure of Io, it is better to use the observed

value of k_2 than the moment of inertia derived from k_2. This eliminates additional assumptions. We derived formulas (63)–(65), which allow the second-order corrections to the lengths of the semiaxes of the figure of Io to be calculated. All corrections are positive and increase the lengths of the equilibrium axes: by $\sim$64.5 m for the a axis, by $\sim$26 m for the b axis, and by $\sim$14 m for the c axis. The theory presented here allows the figure parameters and the fourth-order gravitational moments that differ from zero to be calculated. For the homogeneous model, these parameters are given by formulas (68) and (69).

1. ACKNOWLEDGMENTS

REFERENCES

1. J. D. Anderson, R. A. Jacobson, E. L. Lau, W. B. Moore, and G. Schubert, J. Geophys. Res. **106** (E12), 32 963 (2001a).
2. J. D. Anderson, R. A. Jacobson, T. P. McElrath, *et al.*, Icarus **151**, 204 (2001b).
3. J. D. Anderson, E. L. Lau, W. L. Sjogren, *et al.*, Nature **384**, 541 (1996).
4. J. D. Anderson, G. Schubert, R. A. Jacobson, *et al.*, Science **281**, 2019 (1998).
5. S. F. Dermott, Icarus **37**, 575 (1979).
6. S. F. Dermott and P. C. Thomas, Icarus **73**, 25 (1988).
7. S. V. Gavrilov and V. N. Zharkov, Icarus **32**, 443 (1977).
8. S. V. Gavrilov, V. N. Zharkov, and V. V. Leont'ev, Astron. Zh. **52**, 1021 (1975) [Sov. Astron. **19**, 618 (1975)].
9. W. B. Hubbard and J. D. Anderson, Icarus **33**, 336 (1978).
10. H. Jeffreys, *The Earth* (Cambridge Univ. Press, London, 1962).
11. G. Leone and L. Wilson, J. Geophys. Res. **106** (E12), 32 983 (2001).
12. D. L. Matson, T. V. Johnson, G. J. Veeder, *et al.*, J. Geophys. Res. **106** (E12), 33 021 (2001).
13. V. N. Zharkov, *The 1st Meeting Commemorating O. Yu. Shmidt: Geophysical Studies of Planets and Satellites, Moscow, 2002* (OIFZ RAN, Moscow, 2003), p. 102.
14. V. N. Zharkov, V. V. Leontjev, and A. V. Kozenko, Icarus **61**, 92 (1985).
15. V. N. Zharkov, A. B. Makalkin, and V. P. Trubitsyn, Astron. Zh. **50**, 150 (1973) [Sov. Astron. **17**, 97 (1973)].
16. V. N. Zharkov and V. P. Trubitsyn, Astron. Zh. **52**, 599 (1975) [Sov. Astron. **19**, 366 (1975)].
17. V. N. Zharkov and V. P. Trubitsyn, *Physics of Planetary Interiors* (Nauka, Moscow, 1980) [in Russian].

Translated by V. Astakhov